

**EXPERIMENTAL ASSESSMENT OF STRESS PATH
EFFECTS ON ROCK SALT DEFORMATION**

Mr. Mongkhon Jandakaew

A Thesis Submitted in Partial Fulfillment of the Requirements for the Degree of

Master of Engineering in Geotechnology

Suranaree University of Technology

Academic Year 2003

ISBN 974-533-323-9

การทดสอบเพื่อศึกษาผลกระทบของวิถีความแก่น
ต่อการเปลี่ยนแปลงรูปร่างของเกลือหิน

นายมงคล จันดาแก้ว

วิทยานิพนธ์นี้เป็นส่วนหนึ่งของการศึกษาตามหลักสูตรปริญญาวิศวกรรมศาสตรมหาบัณฑิต

สาขาวิชาเทคโนโลยีธรณี

มหาวิทยาลัยเทคโนโลยีสุรนารี

ปีการศึกษา 2546

ISBN 974-533-323-9

**EXPERIMENTAL ASSESSMENT OF STRESS PATH EFFECTS
ON ROCK SALT DEFORMATION**

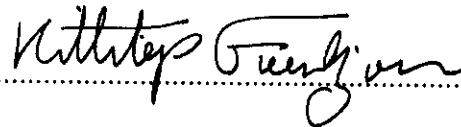
Suranaree University of Technology has approved this thesis submitted in partial fulfillment of the requirements for a Master's Degree.

Thesis Examining Committee



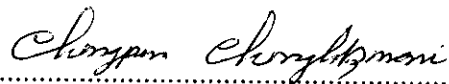
(Asst. Prof. Thara Lekuthai)

Chairman



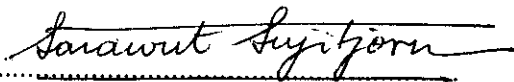
(Assoc. Prof. Dr. Kittitep Fuenkajorn)

Member (Thesis Advisor)



(Dr. Chongpan Chonglakmani)

Member



(Assoc. Prof. Dr. Sarawut Sujitjorn)

Vice Rector for Academic Affairs



(Assoc. Prof. Dr. Vorapot Khompis)

Dean of Institute of Engineering

มงคล จันดาแก้ว: การทดสอบเพื่อศึกษาผลกระทบของวิถีความเค้นต่อการเปลี่ยนแปลง
รูปร่างของเกลือหิน(EXPERIMENTAL ASSESSMENT OF STRESS PATH
EFFECTS ON ROCK SALT DEFORMATION)

อาจารย์ที่ปรึกษา: รองศาสตราจารย์ ดร. กิตติเทพ เฟื่องขจร, 139 หน้า

ISBN 974-533-323-9

วิถีความเค้นหรือลำดับและช่วงเวลาของการให้แรงเป็นปัจจัยสำคัญปัจจัยหนึ่งที่มีผลกระทบต่อพฤติกรรมทางกลศาสตร์ของหิน พฤติกรรมที่ขึ้นกับวิถีความเค้นจะปรากฏเด่นชัดในหินที่มีพฤติกรรมเชิงพลาสติกเช่น เกลือหิน กระบวนการที่ทำให้เกิดความแตกต่างของวิถีความเค้นในมวลหินอาจมีผลมาจากขั้นตอนและช่วงเวลาของการก่อสร้าง โครงสร้างทางวิศวกรรม โดยทั่วไปเพื่อความสะดวกในการวิเคราะห์การออกแบบจะสมมุติให้ผลกระทบจากวิถีความเค้นไม่เกิดขึ้น ถ้าพฤติกรรมที่ขึ้นกับวิถีความเค้นของหินมีมากวิธีการประเมินคุณสมบัติทางกลศาสตร์ของหินในห้องปฏิบัติการควรมีการออกแบบให้สามารถตรวจสอบปัจจัยดังกล่าวได้ และเพื่อให้ได้คุณสมบัติที่ใกล้เคียงกับพฤติกรรมที่เกิดขึ้นจริงในมวลหิน วัตถุประสงค์ของงานวิจัยคือ เพื่อศึกษาผลกระทบของวิถีความเค้นต่อพฤติกรรมทางกลศาสตร์ของหินของเกลือหินโดยการทดสอบในห้องปฏิบัติการและระเบียบวิธีการคำนวณเชิงตัวเลข วิธีการทดสอบที่นำมาประเมินผลกระทบของวิถีความเค้นประกอบด้วย การทดสอบการเคลื่อนไหลสามแกนแบบดั้งเดิมและแบบลดความดันด้านข้าง โดยศึกษาพฤติกรรมของมวลเกลือรอบโพรงเกลือ โดยใช้แบบจำลองทางคอมพิวเตอร์เพื่อประเมินความสำคัญของผลกระทบของวิถีความเค้นต่อโพรงกักเก็บในมวลเกลือหิน ผลการทดสอบคุณสมบัติเชิงกลศาสตร์พื้นฐานระบุว่า ตัวอย่างเกลือหินจากหมวดหินมหาสารคามที่นำมาใช้ในการทดสอบมีค่ากำลังต้านแรงกดในแกนเดียวและกำลังรับแรงดึงอยู่ในเกณฑ์ค่อนข้างสูงเมื่อเทียบกับเกลือหินจากแหล่งอื่น ๆ ผลจากการทดสอบกำลังต้านแรงกดในสามแกนของตัวอย่างเกลือหินระบุว่าอัตราส่วนปัวซองมีค่า 0.37 ค่าแรงยึดเหนี่ยวและมุมเสียดทานภายในมีค่า 6 เมกะปาสคาล และ 50

เส้นที่เท่ากันตัวอย่างเกลือหินที่ทดสอบแบบดั้งเดิมมีการเปลี่ยนรูปร่างมากกว่าตัวอย่างที่ทดสอบแบบลดความดันด้านข้าง ความเหนียวและความเหนียวพลาสติกของเกลือหินที่สอบเทียบได้จากวิธีการทดสอบแบบลดความดันด้านข้างมีค่าสูงกว่าคุณสมบัติที่ได้จากการทดสอบแบบดั้งเดิมเล็กน้อย การทรุดตัวของผิวดินที่คำนวณได้จากการทดสอบแบบลดความดันด้านข้างมีค่าน้อยกว่าจากการทดสอบแบบดั้งเดิมร้อยละ 31.6 (สำหรับแบบจำลองรูปทรงกลม) และ ร้อยละ 30.1 (สำหรับแบบจำลองรูปทรงกระบอก) การหดตัวของโพรงโดยใช้ผลจากการทดสอบแบบลดความดันด้านข้างมีค่าน้อยกว่าผลการทดสอบแบบดั้งเดิมร้อยละ 25.7 (สำหรับแบบจำลองรูปทรงกลม) และ ร้อยละ 23.3 (สำหรับแบบจำลองรูปทรงกระบอก) สามารถสรุปได้ว่าพฤติกรรมเชิงกลศาสตร์ของตัวอย่างเกลือหินจะขึ้นกับวิถีความเค้น การทดสอบแบบลดความดันด้านข้างให้ผลที่สอดคล้องกับความเค้นในภาคสนามมากกว่าวิธีการแบบดั้งเดิม แต่วิธีการทดสอบแบบดั้งเดิมแสดงผลการเคลื่อนไหลและคุณสมบัติของตัวอย่างเกลือหินเป็นไปในเชิงอนุรักษ์มากกว่า

สาขาวิชาเทคโนโลยีธรณี

ปีการศึกษา 2546

ลายมือชื่อนักศึกษา.....*ll. Tach*.....

ลายมือชื่ออาจารย์ที่ปรึกษา.....*K. Sujan*.....

**MONGKHOL JANDAKAEW: EXPERIMENTAL ASSESSMENT
OF STRESS PATH EFFECTS ON ROCK SALT DEFORMATION
THESIS ADVISOR: ASSOC. PROF. KITTITEP FUENKAJORN,
Ph.D., P.E. 139 pp. ISBN 974-533-323-9**

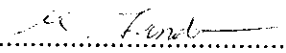
**ROCK SALT/STRESS PATH/TRIAXIAL/CREEP/VISCO-PLASTICITY/
FINITE ELEMENT/CAVERN**

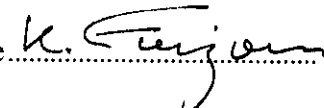
Stress path or sequence and duration of loading are one of the factors affecting the mechanical behavior of rocks. The stress path dependency is even more pronounced in soft rocks that exhibit plastic behavior when subjected to load. The stress conditions in the rock mass may be subject to different stress paths through the processes of construction and operation. For most rock mechanics analyses, stress path independence is often assumed. If the stress path dependency is significant, the laboratory test method should be designed to detect or measure such factors, and hence to obtain test results that are more representative to the actual in-situ conditions. The objective of this research is to assess the effect of stress path on the mechanical behavior of rock salt by means of mechanical laboratory testing and numerical analysis. The creep property parameters calibrated from the results of conventional triaxial creep test (CTC) and radially unloaded triaxial creep test (RUTC) are compared to reveal the effect of stress path. The significance of the stress path dependency is evaluated by performing numerical modeling of salt behavior around storage caverns. The compressive and tensile strengths of the Maha Sarakham salt are

relatively high as compared with those from various sources. The triaxial strength results show that the average Poisson's ratio is 0.37. Based on the Coulomb criterion, the cohesion is 6 MPa and the internal friction angle is 50 degrees. Comparison the creep results from the two triaxial tests shows that the specimens subjected to CTC test show higher deformation than that of the RUTC test under the same octahedral shear stress. The viscoelastic and viscoplastic parameters calibrated from the RUTC test are slightly greater than that from the CTC test. The cavern simulation shows that the surface subsidence obtained from the RUTC properties are 31.6% (for spherical) and 30.1% (for cylindrical) less than those from the CTC properties. The vertical and horizontal closures simulated from the RUTC properties are 25.7% (for spherical) and 23.3% (for cylindrical) less than those from the CTC properties. It is concluded that the salt specimen behavior depends upon the stress paths. The RUTC test results may be more representative to the actual in-situ conditions. The CTC test method, however, yields the creep results and calibrated properties that are more conservative than does the RUTC test method.

School of Geotechnology

Academic Year 2003

Student's Signature 

Advisor's Signature 

ACKNOWLEDGEMENTS

The author wishes to acknowledge the support from the Department of Alternative Energy Development and Efficiency (DEDE) who has provided funding for this research. Asia Pacific Potash Corporation, Ltd. (APPC) has provided the salt cores for testing.

Assoc. Prof. Dr. Kittitep Fuenkajorn is the thesis advisor, Asst. Prof. Thara Lekuthai and Dr. Chongpan Chonglakmani are the thesis committee.

Mongkhon Jandakaew

TABLE OF CONTENTS

	PAGE
ABSTRACT (THAI)	I
ABSTRACT (ENGLISH).....	III
ACKNOWLEDGEMENTS	V
TABLE OF CONTENTS.....	VI
LIST OF TABLES.....	X
LIST OF FIGURES	XII
LIST OF ABBREVIATIONS.....	XX
CHAPTER	
I INTRODUCTION	1
1.1 Problem and Rationale.....	1
1.2 Objectives	2
1.3 Scope of Work	2
1.4 Methodology	3
1.4.1 Literature Review	3
1.4.2 Sample Collection and Preparation.....	3
1.4.3 Laboratory Experiments	5
1.4.4 Numerical Analysis	5
1.4.5 Analysis	6
1.4.6 Thesis Writing	6

TABLE OF CONTENTS (Continued)

	PAGE
1.5 .Thesis Contents.....	6
II LITERATURE REVIEW.....	8
2.1 Theories and Principles.....	8
2.2 Experimental Assessment of Stress Paths.....	10
2.2.1 Rock Salt	10
2.2.2 Other Rocks and Engineering Materials	12
2.3 Mechanical Testing on Salt.....	14
2.4 Stress Around Salt Cavern.....	17
2.5 Constitutive Law used in this Study	21
2.6 Rock Salt in the Maha Sarakham Formation	25
III LABORATORY EXPERIMENTS	29
3.1 Introduction.....	29
3.2 Sample Preparation	29
3.3 Characterization Tests on Salt Specimens	33
3.3.1 . Uniaxial Compressive Strength Tests	33
3.3.2 . Brazilian Tensile Strength Tests.....	39
3.3.3 . Triaxial Compressive Strength Tests	43
3.4 Triaxial Creep Tests	63
3.4.1 Conventional Triaxial Creep Tests.....	63
3.4.2 Radially Unloaded Triaxial Creep Tests	72

TABLE OF CONTENTS (Continued)

	PAGE
IV CALIBRATION OF SALT PROPERTIES	86
4.1 Introduction.....	86
4.2 Calibration of Salt Property Parameters	86
4.2.1 Determination of Elastic Parameters.....	88
4.2.2 Determination of Viscoelastic Parameters	90
4.2.3 Determination of Viscoplastic Parameter.....	90
4.3 Discussions	93
V COMPUTER MODELING	96
5.1 Introduction.....	96
5.2 Area of Study	96
5.3 Model Characteristics	97
5.4 Rock Properties.....	101
5.5 Computer Simulation Results	101
5.5.1 Spherical Model	101
5.5.2 Cylindrical Model.....	105
VI COMPARISON AND DISCUSSIONS	109
6.1 Introduction.....	109
6.2 Comparison of the Experimental Results	109
6.3 Comparison of the Calibrated Property Parameters.....	114
6.4 Comparison of the Computer Modeling Results	114

TABLE OF CONTENTS (Continued)

	PAGE
6.5 Discussions	118
6.5.1 Discussion on the Experiments	118
6.5.2 Discussion on the Property Calibration.....	122
6.5.3 Discussion on the Computer Modeling.....	123
VII CONCLUSIONS AND RECOMMENDATIONS FOR	
FUTURE STUDIES	124
7.1 Conclusions.....	124
7.2 Recommendations for Future Studies.....	127
REFERENCES.....	128
BIOGRAPHY	139

LIST OF TABLES

TABLE	PAGE
3.1 Summary of test results from the uniaxial compressive strength testing	37
3.2 Summary of test results from the Brazilian tensile strength testing	42
3.3 Summary of test results from the triaxial compressive strength testing.....	48
3.4 Test matrix for the conventional triaxial creep testing.....	66
3.5 Summary of the results for the conventional triaxial creep testing.....	73
3.6 Summary of the instantaneous strains calculated from the results of CTC test	74
3.7 Test matrix for the radially unloaded triaxial creep testing.....	77
3.8 Summary of test results for the radially unloaded triaxial creep testing	82
3.9 Summary of the instantaneous strains calculated from the results of RUTC tests.....	83
4.1 The initial salt property parameters obtained from GEO database	89
4.2 Salt property parameters calculated from the results obtained from the CTC tests using the finite element code GEO and the creep equations.....	91
4.3 Salt property parameters calculated from the results obtained from the RUTC tests using the finite element code GEO and the creep equations	92
5.1 Coefficient values for associated rocks selected from the GEO database ...	102
5.2 Summary of salt property parameters for computer models	103

LIST OF TABLES (Continued)

TABLE	PAGE
6.1 Comparison of salt property parameters calculated from different loading paths.....	115
6.2 Properties of salt used in the simulation. They are averaged from four specimens for each loading path	116

LIST OF FIGURES

FIGURE	PAGE
1.1 Research plan for the experimental and numerical assessment of stress path effects on rock salt behavior	4
2.1 A typical section of the Maha Sarakham Formation	24
2.2 Korat and Sakon Nakhon salt basins in the northeast of Thailand	26
2.3 Geological map of the northeast of Thailand.....	27
3.1 Locations where the core samples are obtained and where the geologic sequences are used in the computer modeling.....	30
3.2 Some salt cores used in this research. They are donated by Asia Pacific Potash Corporation, Udon Thani province, Thailand.....	31
3.3 A salt core is cut to desired length using cutting machine.....	31
3.4 A salt specimen is machined to obtain specified dimensions for the triaxial tests	32
3.5 Specimen designations for each test type	34
3.6 A compression machine (Elect/ADR2000 model) is used in the uniaxial compressive strength tests.....	36
3.7 Results of uniaxial compressive strength test. The axial stresses are plotted as a function of axial strain	37

LIST OF FIGURES (Continued)

FIGURE	PAGE
3.8 Comparison of the uniaxial compressive strength of salt tested here (shaded bar) with the results obtained from various sources	38
3.9 Some post-tested specimens (BD99-1-UX01e and UX05e), failed at 37.07 MPa and 34.03 MPa. In the mid-length of the specimens, micro- cracks develop as indicated by milky fragments of the salt. Failure plane makes an angle of 60 degrees with the specimen axis.....	40
3.10 Laboratory arrangements for the Brazilian tensile strength test. SBEL PLT-75 loading machine with the maximum capacity of 350 kN is used	41
3.11 Comparison of the Brazilian tensile strength obtained here (shaded bars) with the results obtained from various sources.....	44
3.12 The Brazilian test specimens after failure. Tensile crack is induced along the loading diameter. The failure plane cuts through the salt crystals.....	45
3.13 A compression machine (Elect/ADR2000 model) and a Hoek cell are used for the triaxial testing.....	47
3.14 Mohr circles and Coulomb criterion used to represent the triaxial compressive strengths	50
3.15 Differential stress ($\sigma_1-\sigma_3$) versus strains from triaxial test result at confining pressure of 6.9 MPa	51

LIST OF FIGURES (Continued)

FIGURE	PAGE
3.16 Differential stress ($\sigma_1 - \sigma_3$) versus strains from triaxial test result at confining pressure of 5.5 MPa	52
3.17 Differential stress ($\sigma_1 - \sigma_3$) versus strains from triaxial test result at confining pressure of 12.4 MPa	53
3.18 Differential stress ($\sigma_1 - \sigma_3$) versus strains from triaxial test result at confining pressure of 15.2 MPa	54
3.19 Differential stress ($\sigma_1 - \sigma_3$) versus strains from triaxial test result at confining pressure of 19.3 MPa	55
3.20 Differential stress ($\sigma_1 - \sigma_3$) versus strains from triaxial test result at confining pressure of 8.3 MPa	56
3.21 Some post-tested specimens subjected to the triaxial stresses. Specimen on the left shows the multi-shear failure at confining pressure of 15.2 MPa. Specimen on the right shows single shear failure at confining pressure of 12.4 MPa	59
3.22 Comparison of the cohesion from the triaxial compressive strength tests obtained here (shaded bar) with the results from various sources.....	60
3.23 Comparison of the internal friction angles obtained here (shaded bar) with the results from various sources.....	61

LIST OF FIGURES (Continued)

FIGURE	PAGE
3.24 Comparison of the Poisson's ratio obtained from the triaxial compressive strength tests performed here	62
3.25 Comparison of stress paths between the conventional method (CTC) and the radially unloaded method (RUTC) in major-minor principal stresses diagram	64
3.26 Schematic diagram for triaxial creep testing. The axial load is applied and maintained by dead weight through a level arm	67
3.27 Result of conventional triaxial creep test for specimen number BD99-1-CTC2e.....	68
3.28 Result of conventional triaxial creep test for specimen number BD99-1-CTC3e.....	69
3.29 Result of conventional triaxial creep test for specimen number BD99-1-CTC4e.....	70
3.30 Result of conventional triaxial creep test for specimen number BD99-1-CTC5e.....	71
3.31 Some post-tested specimens subjected to the conventional triaxial stress path. Both specimens show the tensile crack induced along inter-crystalline boundaries. Specimens on the left and right are subjected to the octahedral shear stresses in the second stage of 9.6 MPa and 10.6 MPa, respectively	75

LIST OF FIGURES (Continued)

FIGURE	PAGE
3.32 Result of radially unloaded triaxial creep test for specimen number BD99-RUTC2e	78
3.33 Result of radially unloaded triaxial creep test for specimen number BD99-1-RUTC3e	79
3.34 Result of radially unloaded triaxial creep test for specimen number BD99-1-RUTC4e	80
3.35 Result of radially unloaded triaxial creep test for specimen number BD99-1-RUTC5e	81
3.36 Some post-tested specimens subjected to the radially unloaded triaxial stress path. Both specimens show the tensile crack induced along inter-crystalline boundaries but specimen on the right show more expansion. Specimens on the left and right are subjected to the octahedral shear stresses in the second stage of 9.6 MPa and 10.6 MPa, respectively	84
4.1 Model of salt specimen by using a single element used in the calibration of property parameters	87
4.2 Comparison of the strain-time curves between GEO simulation (dot line) and the actual creep test results (solid line) obtained from the conventional triaxial tests	94

LIST OF FIGURES (Continued)

FIGURE	PAGE
4.3 Comparison of the strain-time curves between GEO simulation (dot line) and the actual creep test results (solid line) obtained from the radially unloaded triaxial tests	95
5.1 Reclassified rock sequences for geomechanics analysis for borehole number K-55 at Wanon Niwat District, Sakon Nakhon	98
5.2 Finite element meshes for spherical model showing the spherical cavern and rock stratigraphy at Wanon Niwat District, Sakon Nakhon. The cavern diameter is 40 meters	99
5.3 Finite element meshes for the cylindrical model showing the cavern and rock stratigraphy at Wanon Niwat District, Sakon Nakhon. The cylindrical cavern is 40 meters high with a diameter of 40 meters	100
5.4 Surface subsidence induced by the spherical cavern with the properties calibrated from the results of CTC test.....	104
5.5 Surface subsidence induced by the spherical cavern with the properties calibrated from the results of RUTC test.....	104
5.6 Diameter closure of the spherical cavern with the properties calibrated from the results of CTC test.....	106
5.7 Diameter closure of the spherical cavern with the properties calibrated from the results of RUTC test.....	106

LIST OF FIGURES (Continued)

FIGURE	PAGE
5.8 Surface subsidence induced by the cylindrical cavern with the properties calibrated from the results of CTC test.....	107
5.9 Surface subsidence induced by the cylindrical cavern with the properties calibrated from the results of RUTC test.....	107
5.10 Diameter closure of the cylindrical cavern with the properties calibrated from the results of CTC test.....	108
5.11 Diameter closure of the spherical cavern with the properties calibrated from the results of RUTC test.....	108
6.1 Comparison of the creep test results from different loading paths on salt specimens (no. BD99-1-CTC2e and BD99-1-RUTC2e).....	110
6.2 Comparison of the creep test results from different loading paths on salt specimens (no. BD99-1-CTC3e and BD99-1-RUTC3e).....	111
6.3 Comparison of the creep test results from different loading paths on salt specimens (no. BD99-1-CTC4e and BD99-1-RUTC4e).....	112
6.4 Comparison of the creep test results from different loading paths on salt specimens (no. BD99-1-CTC5e and BD99-1-RUTC5e).....	113
6.5 Comparison of surface subsidence induced by the spherical cavern with the CTC properties and RUTC properties.....	117
6.6 Comparison of vertical closure of the spherical cavern with the CTC properties and RUTC properties.....	119

LIST OF FIGURES (Continued)

FIGURE	PAGE
6.7 Comparison of horizontal closure of the spherical cavern with the CTC properties and RUTC properties	119
6.8 Comparison of surface subsidence induced by the cylindrical cavern with the CTC properties and RUTC properties	120
6.9 Comparison of vertical closure of the cylindrical cavern with the CTC properties and RUTC properties	120
6.10 Comparison of horizontal closure of the cylindrical cavern with the CTC properties and RUTC properties	121

LIST OF SYMBOLS AND ABBREVIATIONS

A	=	initial cross-section area
C	=	deterioration coefficient
c	=	cohesion
D_2	=	hydrostatic elastoviscosity
D_m	=	new diameter of specimen
D_{ro}	=	original diameter of specimen
D_s	=	diameter of specimen
E_1	=	elastic modulus
f_D	=	deteriorating function
G_1	=	shear modulus
G_2	=	retarded shear modulus
G_{21}	=	retarded shear moduli for short-term viscoelastic strain
G_{22}	=	retarded shear modulus for medium-term viscoelastic strain
G_{23}	=	retarded shear modulus for long-term viscoelastic strain
ΔK_O	=	variance portion of the strength
K_1	=	ultimate bulk modulus
K_2	=	retarded bulk modulus
K^A	=	unconfined octahedral shear strength
K^B	=	ultimate octahedral shear strength
K_O	=	octahedral shear strength

LIST OF SYMBOLS AND ABBREVIATION (Continued)

K^R	=	residual strength
L	=	thickness of specimen
L_m	=	new length of specimen
L_{ro}	=	original length of specimen
Δl	=	axial deformation
l_0	=	original specimen length
m	=	Lode parameter
P	=	plastic transition pressure
P_{bf}	=	failure load of Brazilian tensile test
P_{uf}	=	failure load of uniaxial compressive test
VE	=	viscoelastic behavior
V_{oil}	=	hydraulic oil bleeding from Hoek cell
V_m	=	new rock volume
V_{ro}	=	original rock volume
V_{steel}	=	volume of the moving steel plate
α	=	yield surface coefficient
ϵ_1	=	maximum principal strain
ϵ_2	=	intermediate principal strain
ϵ_3	=	minimum principal strain
ϵ_{axial}	=	axial strain
ϵ_{VD}	=	non-recoverable volumetric dilation

LIST OF SYMBOLS AND ABBREVIATION (Continued)

ϵ_{ij}^e	=	elastic strain tensor
ϵ_f	=	failure strain
ϵ_{ij}	=	total strain tensor
ϵ_{lat}	=	lateral strain
ϵ_m	=	mean strain
ϵ_{ij}^p	=	plastic strain tensor
ϵ_{vol}	=	volumetric strain
ϕ	=	angle of internal friction
γ_{21}^{VE}	=	short-term viscoelastic strain rate
γ_{22}^{VE}	=	medium-term viscoelastic strain rate
γ_{23}^{VE}	=	long-term viscoelastic strain rate
γ_{oct}^s	=	octahedral shear strain rate in steady state
γ_{total}^{VE}	=	total viscoelastic creep strain rate
γ_c	=	critical strain of elastic limit
γ_{oct}	=	octahedral shear strain
γ_{oct}^i	=	viscoelastic octahedral shear strain
γ_o	=	induced octahedral shear strain
η_2	=	elastoviscosity
η_{21}	=	elastoviscosity coefficient for short-term

LIST OF SYMBOLS AND ABBREVIATION (Continued)

η_{22}	=	elastoviscosity coefficient for medium-term
η_{23}	=	elastoviscosity coefficient for long-term
η_4	=	plastoviscosity
λ	=	Lame constant
ν	=	Poisson's ratio
σ	=	normal stress
σ_1	=	maximum principal stress
$\sigma_1 - \sigma_3$	=	differential stress
σ_2	=	intermediate principal stress
σ_3	=	minimum principal stress
τ	=	shear stress
τ_{oct}	=	octahedral shear stress
τ_{oct}^1	=	octahedral shear stress in the first stage
τ_{oct}^2	=	octahedral shear stress in the second stage

CHAPTER I

INTRODUCTION

1.1 Problem and Rationale

Stress path or sequence and duration of directional loading are one of the factors affecting the mechanical behavior of rocks. The stress path dependency is even more pronounced in soft rocks that exhibit plastic behavior when subjected to load. The issue of stress path dependency is important in various disciplines, especially in geotechnical problems, e.g. dams, tunnels, retaining walls and footing. The stress conditions in the rock mass may be subject to different stress paths through the processes of construction and operation. For most rock mechanics analyses, stress path independence is often assumed. Rare experimental work has been performed to verify this phenomenon. Only the theoretical implication has been shown, particularly when complex behavior of rock material has to be dealt with. If the stress path dependency is significant, the laboratory test method should be designed to detect or measure such factors, and hence to obtain test results that are more representative to the actual in-situ conditions.

Analysis and design of engineering structures, such as storage caverns and mine openings, in rock salt may need to recognize the effect of stress path because rock salt exhibits a strong time-dependent behavior under relatively low applied load. Assessing the time-dependent (creep) properties of the salt by performing the conventional triaxial creep test as specified by American Society for Testing and

Materials (ASTM) may not be adequate. Since the stress paths designated for such test are different from those actually occurred under in-situ conditions, the test results may not be strictly represent the actual properties of the rock. Experimental assessment of the stress path dependency of rock salt is rare. In addition, the significance of the stress path effect on the analysis and design of the engineering structures in salt mass has not been specifically evaluated.

1.2 Objectives

The objective of this research is to assess the effect of stress path on the mechanical behavior of rock salt by means of mechanical laboratory testing and numerical analysis. The creep property parameters calibrated from the results of conventional triaxial creep test (CTC) and radially unloaded triaxial creep test (RUTC) are compared to reveal the effect of stress path. The significance of the stress path dependency is evaluated by performing numerical modeling of salt behavior around storage caverns.

1.3 Scope of Work

The research efforts involve two main tasks: laboratory mechanical testing on rock salt and numerical modeling on salt caverns. The conventional triaxial creep tests and the radially unloaded triaxial creep tests are performed to investigate the difference in the mechanical behavior of rock salt under different loading paths. The analytical and experimental works assume homogeneous and isotropic conditions. The study will not include the shape and size effects on the salt specimen. Rock salt used in this research has been donated by Asia Pacific Potash Corporation, Udon

Thani province, Thailand. They are cylindrical shapes with 6-centimeters in diameter and are drilled from the Sakon Nakhon Basin. The loading rate and testing temperature are maintained constant. The results from the laboratory tests are used to calibrate the creep property parameters of a non-linear finite element program GEO (Serata and Fuenkajorn, 1992; Fuenkajorn and Serata, 1992, 1993, 1994). The program is used to compute the stresses and deformation of salt mass around storage caverns under different sets of the calibrated property parameters. Comparisons of the numerical results are made to assess the impact of the stress paths. The actual subsurface salt formation at Ban Kudjik, Sakon Nakhon Basin, Thailand is used as an example for the modeling. No in-situ testing is performed in this research.

1.4 Methodology

This research consists of six tasks, including literature review, sample collection and preparation, laboratory experiments, numerical analyses, analysis, and thesis writing. Figure 1.1 shows the research plan.

1.4.1 Literature Review

Literature review has been performed on relevant technical reports, conference papers and journals. The reviewed topics include the conventional triaxial testing and other relevant testing on rocks, stress path effect, mechanical testing on salts, stress around salt cavern, and the evaporite geology of the Maha Sarakham Formation. Summary of the literature review is documented.

1.4.2 Sample Collection and Preparation

Rock salt samples used in this research have been donated by Asia Pacific Potash Corporation, Udon Thani province, Thailand. The core samples are

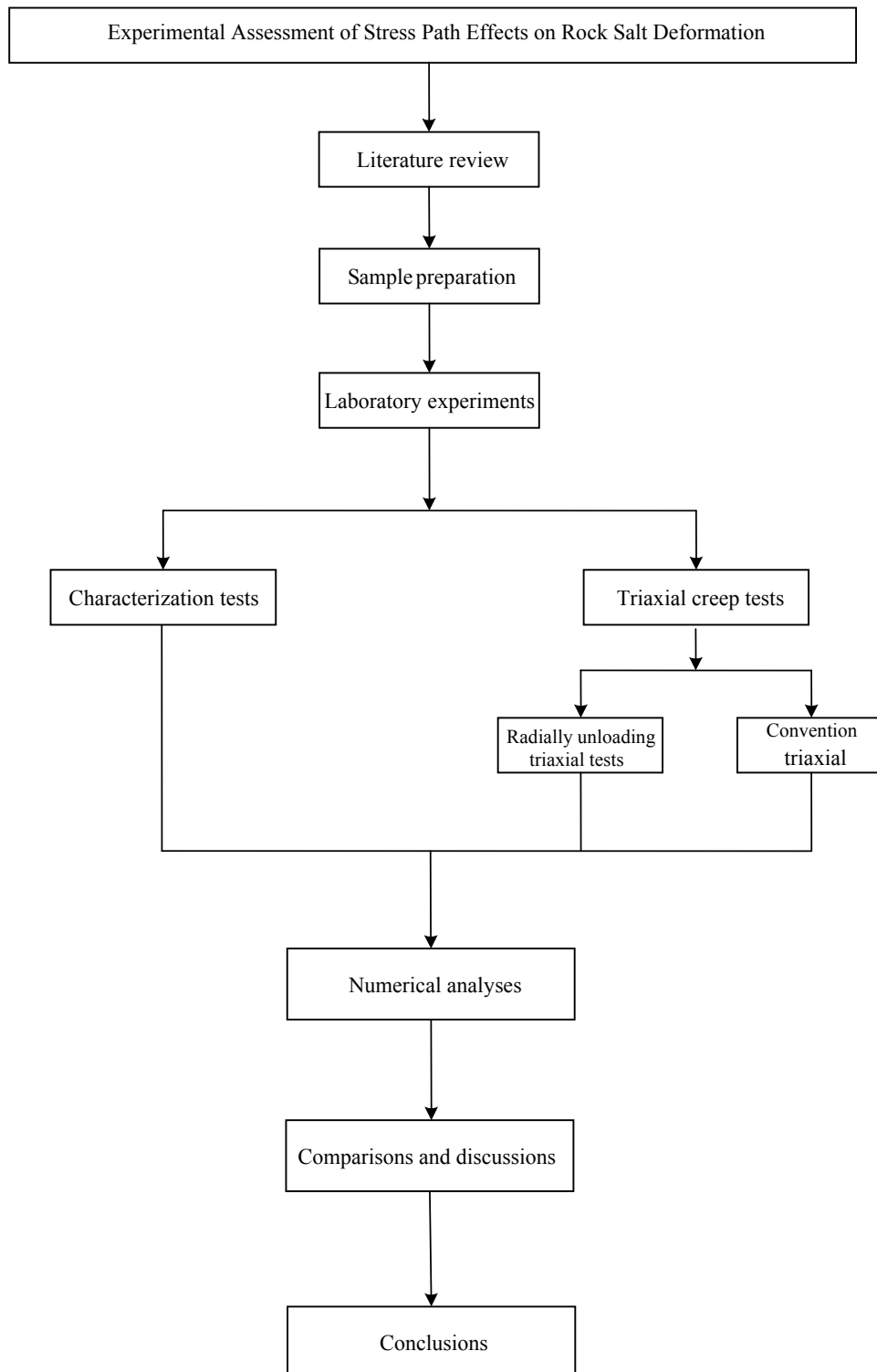


Figure 1.1 Research plan for the experimental and numerical assessment of stress path effects on rock salt behavior.

from the Sakon Nakhon Basin. They are cylindrical shapes with 6-centimeters in diameter. Preparations of these samples follow as much as practical the American Society for Testing and Materials (ASTM D4543-85). The dimension requirements of the tested specimens comply with both the ASTM standard and the International Society for Rock Mechanics (ISRM) suggested methods. Petrographic features and depths where the core specimens obtained are recorded.

1.4.3 Laboratory Experiments

The mechanical laboratory testing is performed on the salt specimens. The ASTM standards and the test method suggested by Wawersik and Preece (1981) are followed. The test series include the uniaxial compressive strength tests (ASTM D2938-95), the Brazilian tensile strength tests (ASTM D3967-92), the triaxial compressive strength tests (ASTM D2664-95), the conventional triaxial creep tests (ASTM D4406-93), and the radially unloaded triaxial creep tests. For both triaxial creep tests, a number of specimens are subjected to two stages of loading. The octahedral shear stresses of 2.0, 3.5, 4.1 and 5.1 MPa are applied for the first stage. The second stage uses the shear stresses of 8.7, 9.6, and 10.6 MPa. Axial strains are monitored during the tests. The relationship between the strain and time is determined for each loading stage.

1.4.4 Numerical Analyses

The objectives of performing numerical modeling are to calibrate the salt properties from the test results with different stress paths, and to simulate the storage caverns in salt formation. The property parameters studied here include the shear modulus, ultimate bulk modulus, retarded shear modulus, retarded bulk modulus elastoviscosity and plastoviscosity.

Computer model is constructed to represent the salt formation around the storage caverns. The simulation of the cavern behavior is made using the two different property sets. Similarities and differences of the results will be investigated in term of time-dependent stress distribution, cavern closure, and surface subsidence.

1.4.5 Analysis

The effect of stress paths is discussed in terms of the representation of the test results that are obtained from different stress paths, as well as the impact of the stress paths on the computer simulation. Validity and practicality of both triaxial testing techniques are analyzed.

1.4.6 Thesis Writing

The thesis presents the results of literature review, comprehensive methodology, results of testing and computer modeling, discussions and conclusions of the findings.

1.5 Thesis Contents

This research thesis is divided into seven chapters. The first chapter includes problem and rationale, research objectives, scope of work, and research methodology. Chapter II presents results of the literature review on stress path effect, mechanical testing on rock salt, stress around salt caverns, and the evaporite geology of the Maha Sarakham Formation. Chapter III describes sample preparation, and laboratory experiments. The experiments include characterization and triaxial creep tests on the salt specimens obtained from the Sakon Nakhon Basin. The constitutive law and salt parameters calibration are described in Chapter IV. Chapter V presents the results of computer modeling using parameters calibrated from different stress paths. They

emphasize on the cavern convergence and ground surface subsidence. Chapter VI discusses the effect of different stress paths on salt specimens and the significance of the difference in terms of the computer simulations. Chapter VII provides conclusions and recommendations for future studies.

CHAPTER II

LITERATURE REVEIW

2.1 Theories and Principles

The mechanical behavior of rock is commonly analyzed either by the principle of elasticity or inelasticity. In most cases, the principle of elasticity is often used or assumed for the stress-strain analysis, because it is convenient for practical applications. Under this assumption the effect of the different loading directions and sequences is ignored (Chen and Zhang, 1991).

For some rocks, the assumption of inelastic behavior is more suitable than linearly elastic, especially for soft rock such as salt. The mechanical behavior of rock salt is important for geological engineering structures, such as nuclear waste repository, storage caverns and underground salt mines. Salt exhibits complex mechanical behavior due to the plastic deformation and time dependency. Chen and Zhang (1991) and Shames and Cozzarelli (1997) suggest that the analysis of materials in the plastic range is dependent of stress path. The influence of stress path or loading sequence and direction should therefore be considered to analyze the engineering structures in salt formation.

For the inelastic behavior, strain hardening becomes a dominant range. To generate a new yield surface, the plastic deformation is developed by increasing the applied stresses. This new yield surface is called subsequent yield surface or loading surface. Since the loading surface changed according to the way the plastic

deformation is produced, the stress-strain behavior of a work-hardening (ductile) material is loading path dependent or loading history dependent (Chen and Zhang, 1991, and Khan and Huang, 1995). Two theories for the work-hardening materials have been proposed: the deformational theory and the incremental theory. The deformational theory neglects the effect of loading path in the development of stress-strain relationship. Determinations of the total strain, ε_{ij} , and the plastic strain, ε_{ij}^p , are unique along the plastic deformation continuum. The total strains are decomposed into elastic and plastic components (ε_{ij}^e and ε_{ij}^p) by a simple superposition:

$$\varepsilon_{ij} = \varepsilon_{ij}^e + \varepsilon_{ij}^p \quad (2.1)$$

where the functional plastic range depends on the effective strain.

For the incremental theory, the total incremental strains, $d\varepsilon_{ij}$, are assumed to be divisible into elastic, $d\varepsilon_{ij}^e$, and plastic, $d\varepsilon_{ij}^p$, components:

$$d\varepsilon_{ij} = d\varepsilon_{ij}^e + d\varepsilon_{ij}^p \quad (2.2)$$

For this theory, the plastic deformation depends on the loading path, so it is necessary to integrate the incremental stress-strain relation along the loading path to obtain the final state of deformation. There are three basic elements in the development of stress-strain relationship for this theory: 1) loading criterion, 2) flow rule, and 3) hardening rule. Chen and Zhang (1991) describe these rules which are derived from the basis of stress path effect consideration. For the hardening rule, Khan and Huang (1995) describe the determination of the subsequent yield surface of isotropic strain hardening (subgroup of hardening rule) and the total plastic work. These are called the work-hardening hypothesis. The amount of hardening depends only on the total plastic work and does not depend on the loading path.

2.2 Experimental Assessment of Stress Paths

2.2.1 Rock Salt

Wawersik and Hannum (1980) study the loading path conditions using the conventional triaxial test under constant confining pressure, constant mean stress, and axial stress. Salt specimens are subjected to quasi-static triaxial compression. They find that the maximum and minimum principal strains (ϵ_1 and ϵ_3) are numerically greatest along the path of constant confining pressure. The smallest ϵ_1 and ϵ_3 are obtained along the path of constant axial stress. The greatest ratio of ϵ_3/ϵ_1 is obtained along the path of the lowest pressure. For the total strains, the stress path also affects the magnitudes of the strain increments and the ratios of strain increments at common stress states. This observation indicates that the stress path affects rock salt behavior. Lux and Rokahr (1984) compare the results of the conventional and the extensional triaxial tests on rock salt. For the short term behavior, the strength of rock salt significantly depends upon the type of stress state and the mean stresses. For the long term behavior, the triaxial extension test shows less creep deformation than that of the triaxial compression test under the same deviatoric stress. The results of Wawersik and Hannum (1980) and Lux and Rokahr (1984) demonstrate the loading path in the triaxial compression tests on salt specimens that can induce more creep deformation than those of the triaxial extension tests. Hunsche and Albrecht (1990) study the effect of the variation of hydrostatic stress (mean stress), loading path (load geometry), temperature and residual strength on the true triaxial strength of rock salt. It is found that the mean stress and the load geometry, as described by the Lode parameter (m), are the main factors influencing the primary strength of rock salt.

Assis and Kaiser (1991) conduct two different triaxial compression tests on Saskatchewan potash specimens using conventional method and constant mean stress (J1) method. Comparison of the results shows that the loading path from J1-constant method exhibited considerably higher creep deformation than that from the conventional method for the same stress state, especially in transient creep phase. The results also show that the J1-constant method presents a directly proportional relationship between creep deformation and confining stress but for the conventional method, the creep deformation is directly proportional to applied deviatoric stress and inversely proportional to the confining stress. They conclude that the results might have serious implications to the prediction of in-situ time-dependent behavior of underground openings. They suggest that the J1-constant stress path is more representative of the excavation procedure of underground openings and that should be adopted for providing creep properties in laboratory.

Allemendou and Dusseault (1993) perform cyclic creep testing on rock salt. The experiments are designed for the triaxial testing program and focused on the stress path. They find that the octahedral stress and deviatoric stress can affect the creep of rock salt. The radial unloading triaxial test shows less deformation than that from the conventional triaxial test. However, the peak strength at peak strain from both tests is similar, and the point at which the yield envelope intersected is not significantly different. Aubertin et al. (1999) and Yahya et al. (2000) conduct strain rate tests using the conventional triaxial loading and the reduced triaxial extension loading. The tests are performed to use for verifying the mathematic model for rock salt. The rock salt specimens are subjected to high confining pressure, where fully plastic (ductile) deformation mechanisms dominated. The test results show that

during a constant strain rate tests, the flow stress at a given accumulated strain is larger if the strain rate is higher. The reduced triaxial extension loading usually induces an elastic response.

2.2.2 Other Rocks and Engineering Materials

Jaeger (1967) conducts mechanical laboratory testing on brittle rock specimens. The stress path is parallel to the direction of the maximum principal stress. The rocks are fractured by increasing the maximum stress while the intermediate and the minimum principal stresses are constant. He states that the possibility of path-dependent fractures remains inconclusive. Swanson and Brown (1971) investigate the effect of stress path on the development of fracture and the failure stress for several rocks. It is observed that the maximum stresses in all rock tests are independent of the stress path. Crouch (1972) also confirms this after conducting experiments on South African norite specimens using quasi-static triaxial compression method. The volumetric strains are measured to present the effect of stress path. The results indicate that the compressive strength is independent of the way in which the axial and confining stresses are applied. On the contrary Guangzhi et al. (1988) conduct laboratory experiments on sandstone and limestone specimens. They find that the different stress paths can affect the rock strength. The experiments are performed under three types of the stress path by using the true triaxial apparatus. The failure could be caused not only by increasing the maximum principal stresses, but also by decreasing the intermediate and minimum principal stresses.

Korshunov et al. (1996) study the effect of loading path on the parameters of thermomechanical treatment of titanium alloy VT9. The values of these parameters are changed under different paths. Bylia et al. (1997) conduct experiments

on the same material to study the effect of different loading paths on the textures and micro-structural parameters. It is found that those values change after testing along different paths. The test results obtained by Korshunov et al. (1996) and Bylia et al. (1997) lead to a conclusion that the loading path influences the kinetics of significant structural changing. These are the first efforts in which specialists in mechanics and material sciences have worked together to derive conclusions of practical relevance. Evidently, such works are very important and should be pursued in the future (Padmanabhan et al., 2001)

Inoue et al. (1998) investigate the loading path effect on the low cyclic fatigue of glass fabrics composite. Three types of the loading path are applied under tension and torsion biaxial loading. The experimental results reveal that no significant effect of loading path on the fatigue life (i.e. fatigue strength) exists. The fatigue lives at low cyclic fatigue are almost independent of the loading path since final failure of the material is due to the fiber breakage.

Lee et al. (1999) investigate the potential of the stress path effect on the mechanical behavior of the Pei-Tou Sandstone. They perform a series of hollow cylindrical triaxial tests. The stress path is the identification of the different angles between the stress path and the projection of the maximum principal stress axis on the octahedral plane. The test results show that the shape of the failure surface on the octahedral plane depends on the value of the angle.

It can be concluded here that the stress path has an effect on the mechanical behavior of inelastic materials (e.g., ultimate strength, strain increment and creep deformation). For linearly elastic materials, the influence of stress path remains ambiguous. The different stress paths are used for various objectives, such as

to construct yield surface or failure surface and to describe models. However, no published research has revealed the effect of stress path to evaluate the mechanical parameters of rocks.

2.3 Mechanical Testing on Salt

Uniaxial compression test is a basic laboratory testing technique to determine the strength and stiffness of rocks under uniaxial load. Lux and Rokahr (1984) have performed uniaxial compressive strength tests on salt obtained from nine different locations. The tests are carried out on a strain regulation basis with a strain rate of 0.25 per minute. The results indicate that the strengths of rock salt are strongly influenced by texture and the structure. The strengths of 38-41 MPa are determined for fine crystalline, slightly impure and relatively homogeneous rock salt. For medium- to coarse-crystalline rock salt with a steep to vertical orientation of the elongated crystals, the strengths of 11-16 MPa are obtained. The medium compressive strengths from 20 to 28 MPa belong to the medium- to coarse-grained crystalline rock salt with a low anhydrite impurity lacking a distinct crystal orientation, respectively with none to steeply inclined crystal structure. Hansen et al. (1984) have carried out series of the laboratory testing on ten natural rock salts. Tested specimens are 50-100 millimeters in diameter. They are collected from several sources in the United States, including Richton, Weeks Island, Vacherie, New Mexico, Avery Island, Jefferson Island, Lyons, Cote Blanche, Permian basin and Paradox basin. Their range values of the compressive strengths are 13.3-33.3 MPa. Fuenkajorn and Daemen (1988) have tested salt specimens from Permian basin, New Mexico. Tested conditions are controlled with stress rates of 3-190 MPa/min. The average

uniaxial compressive strength is 18.4 MPa. Wanten et al. (1993) have studied the uniaxial compressive strengths of salt under controlled strain rates between 10^{-4} - 10^{-7} per second and temperatures between 20 and 200 °c. The uniaxial compressive strengths are 15-30 MPa. Devries et al. (2002) have performed and compiled uniaxial compressive strengths of salt from several sites, including Petal, Bay gas Well No.2 in McIntosh Dome, Napoleonville, McIntosh, Spindletop and Barber Hill, which show the strengths of 14.9, 17.1, 21.2, 18.7, 22.5, and 25.1 MPa, respectively

Boontongloan (2000) has tested salt specimens from Sakon Nakhon Basin, Udon Thani Province, Thailand. Tested specimens are obtained from three salt members of the Maha Sarakharm Formation. The uniaxial compressive strengths are 18.5, 26 and 25 MPa for the Upper, Middle and Lower Salt members, respectively. For the Middle Salt, the average tangent and secant moduli at 50% of ultimate strength are 5.6 and 9.9 GPa, respectively. For the Lower Salt, the average tangent and secant moduli are 6.4 and 11.4 GPa, and the Poisson's ratios are 0.35 and 0.42. Wetchasat (2002) also tests the salt from the same source. The test series vary stress rate from 0.01 to 1.0 MPa/s. The average uniaxial compressive strength is 23.0 MPa for the Middle Salt, and 31.1 MPa for the Lower Salt. Phueakphum (2003) conducts uniaxial compressive strength tests on the Middle Salt from Udon Thani Province, using a stress rate of 0.1 MPa/s. The average uniaxial compressive strength is 23.0 MPa. The failure axial strains are 0.017-0.035. Other researches have tested the salt specimens from Udon Thani Province. They present the same range of strength values (Fuenkajorn and Jandakaew, 2003 and Fuenkajorn et al., 2003).

Hansen et al. (1984) have performed Brazilian tension test on ten natural rock salts. The rocks are collected from several sources in the United States. The tensile

strengths vary from 1.1 to 2.6 MPa. Fuenkajorn and Daemen (1988) have tested salt specimens from the Salado Formation under a stress rate of 3.45 MPa/min. The average tensile strength is 1.59 MPa. They suggest that the strength of intercrystalline boundaries is lower than that of the salt crystal. Hunsche (1993) studies the effect of loading rate on the tensile strength. It is concluded that the suitable stress rate for the Brazilian test on salt specimen is between 0.017 and 0.248 MPa/s. Hardy (1996) has tested fine-grained salt specimens using different methods; direct-pull test, Brazilian test and hoop-stress test. The tests are controlled under stress rates of 0.003-0.059 MPa/s. The Brazilian test gives the highest strength while hoop-stress test gives the lowest strength. Devries et al. (2002) have performed and complied tensile strength tests on various salts. The tensile strengths vary from 1.3 to 1.8 MPa.

For salt specimens obtained from the Maha Sarakham Formation, Thailand. They have been tested by Boontongloan (2000), Wetchasat (2002), Phueakphum (2003), Fuenkajorn and Jandakaew (2003) and Fuenkajorn et al. (2003). They report the range of tensile strengths for this salt is from 1.4 to 2.2 MPa.

Triaxial compressive strength test determines the rock strength under to triaxial stress states. At low confining pressures, salt fails in a brittle mode, but becomes increasingly plastic at higher pressures. A parabolic-shaped failure surface may be represented by von Mises criterion. (Serata, 1968; Dreyer, 1972; Wawersik et al., 1976; Fairhurst et al., 1979 and Ottosen and Krenk, 1979). Lux and Rokahr (1984) have conducted triaxial compression and extension tests on salt to study the effects of test type, confining pressures and intrinsic impurity. The test results show that the strength of rock salt depends significantly upon the type of stress state and on the mean stress. For different crystalline textures, the greater strength of fine crystalline

rock salt at lower confining pressure does not increase at the same rate with the rising confining pressures. Hansen et al. (1984) have carried out triaxial tests on ten natural rock salts collected from several sources in the United States. Tested specimens are subjected to confining pressures of 0, 1.7, 3.4 and 20.7 MPa. For the linear Mohr-Coulomb failure, the ranges of cohesion and friction angle of the salt are from 2.07 to 4.68 MPa and from 56.7° to 64.7° , respectively. Fuenkajorn and Daemen (1988) study the effects of strain rate on the salt deformation under confining pressures of 1.54-8.18 MPa. The constant strain rate is from 2.25×10^{-5} to 2.08×10^{-4} per second. The salt behaves as strain softening when they are subjected to a high strain rate, and as strain hardening under a low strain rate. Therol and Ghoreychi (1996) find that salt generates cracks when the volumetric strain changes from linearly elastic to non-linear modes.

Wetchasat (2002) have performed triaxial tests on the Maha Sarakham salt. The experimental results are fitted by Coulomb criterion. The value of cohesion and friction angle of salt is 8 MPa and 49° , respectively.

2.4 Stress Around Salt Caverns

The purpose of this section is to review the studies of stress states around salt caverns. The issues include stress measurement techniques, in-situ monitoring, and the stresses around underground caverns in salt mass.

Nelson and Kocherhans (1984) have estimated the in-situ stresses by loading salt strata to the point of hydraulic fracture. They conclude that the in-situ stress data reveal reasonable values of average lithostatic vertical stress and minimum horizontal stresses. The data give an average lithostatic stress gradient of 1.15 psi per foot of

depth. The maximum horizontal stress calculated from elastic stress methods is about 1.5 times lithostatic, which seems high. The deeper loading tests lacked a distinct peak pressure, which implies an increase of the plastic behavior at greater depths.

Crotogino (1984) has studied the in-situ testing techniques on salt cavern. The current methods and the new methods are described. The current methods use the technique of convergence of cavern volume to evaluate the in-situ stresses. Gas and brine are normally used to fill the caverns for monitoring cavern closures that refer to the in-situ stresses acting on the cavern. For the new methods, the borehole test, reduced internal pressure test, and laser and sonar surveys are presented. In conclusion, the selection and necessity for in-situ tests depend on the specific project and the sufficient explored data.

Dreyer (1984) uses finite element technique to calculate roof and pillar stresses around the crude oil storage cavern. The stresses acted around the cavern are the horizontal, vertical and tangential stresses under both oil filled and atmospheric internal pressures. The horizontal stresses in the roof tend to decrease as the distance above the cavern roof increases. In contrast, the vertical stresses tend to increase as the distance above the cavern roof increases. The horizontal and vertical stresses in the pillars increase with the distance from the cavern wall. The tangential stresses are higher near the cavern wall. These findings hold true for both oil filled case and atmospheric pressure case. The effect of roof shape is also examined. The horizontal, vertical and maximum shear stresses reduce as the height of the caverns roof approached the width of the cavern. This shape is considered to be the most stable form for the cavern roof.

Fischer et al. (1988) analyze the behavior of salt caverns used for oil and gas storages. The cavern and surrounding salt mass are modeled to predict stresses and displacement within the salt as a function of time. The outer-to-inner radius ratio is defined as four and the overburden stress is 2500 psi. The outer radius is fixed, corresponding to a multiple cavern configuration, and the pressure on the cavern wall is rapidly decreased from the in-situ value of 3775 psi to 1300 psi and then held constant. These conditions correspond to a brined-filled cavern at a depth of 2500 ft with a maximum excess lateral stress. The results show that the radial and tangential stresses increase as the outer-to-inner radius ratio increases. Lux (1988) has classified the lifetime of underground cavern structure into three significant load situations. The first phase over a period of several months to a few years presents a more or less constant internal pressure corresponding to the brine pressure. For the operating phase, short-term internal pressure drops at a high rate causing by removal of the stored gaseous product. The latest phase is operational phase with a fictitious constant mean internal pressure over a period of some decades. These imply that the radial stresses around cavity decrease from the leaching phase to the operational phase.

Hardy (1993) uses acoustic emission to evaluate the in-situ stress in salt. Laboratory loading testes are carried out on specimens of salt obtained from borehole coring methods. During loading, micro-level seismic activity (acoustic emission) occurring within the material is recorded. Suitable analysis of these data provides information on in-situ state of stress at the point in structure where the test specimen is originally located. Rolfs et al. (1996) analyze the post-operational geotechnical stability of a waste disposal cavern constructed in rock salt. Numerical calculation

has been used to determine the interaction between the stored waste material and the surrounding rock. The results indicate that the stress in rock salt formation for deeper lying caverns only diminishes slightly in the first few years. However, the stress is released more rapidly once the stored material has compacted significantly under the influence of rock deformation. As a result, the stress is virtually completely released within 100 years.

The virgin stress measurement and its distribution around designed structures in salt, especially borehole and cavities, have been studied by several researchers (Clerc et al., 1980; Eriksson and Michalski, 1986; Pudewills, 1988; Heusermann, 1988; Hugout, 1988; Berest and Blum, 1993; and Massier, 1996). Various techniques have been used including calculation, monitoring, and computer simulation. Some results show that the vertical and radial stresses appear to be high near the borehole wall and decrease as distance from borehole wall increases. The radial stresses reduce rapidly with respect to time (Wallner, 1988 and Schmidt, 1993).

The research results above have indicated that the magnitude and direction of the virgin in-situ stresses should be known in order to achieve a safe and optimum structural design. The stress field around the salt cavern depends on the geometry, depth, distance of cavern wall, internal pressures and operational phases. The stresses highly concentrate on the irregular profile of the cavern which may cause instability. At great depth, the cavities are subjected to high stress magnitudes. The tangential stresses are high at the cavern wall. Cycles of the internal pressure also affect the state of field stresses. The stresses are also influenced by changing the constructional and operational phases. As the result, a true loading sequence for triaxial test may be required to obtain salt properties that realistically represent the stresses state around underground caverns.

2.5 Constitutive Law used in This Study

The constitutive law used in this study is developed by Fuenkajorn and Serata (1992, 1993, 1994) and Serata and Fuenkajorn (1992). The rheological constitutive model used here is capable of simulating the elastic, viscoelastic, viscoplastic, strain-softening and dilation behavior of time-dependent materials, such as rock salt. These equations have been incorporated into a finite element code, named GEO. A brief discussion identifying its unique derivation of the constitutive equations is given below.

The von Mises criterion is used to describe the failure surface and to develop a strain-softening model for geologic materials. It is proposed that the octahedral shear strength K_O increases with an increase of the mean stress σ_m toward an ultimate value. The rate change of K_O with respect σ_m can be expressed as,

$$\partial K_O / \partial \sigma_m = \alpha (K^B - K_O), \quad (2.3)$$

where α is a yield surface coefficient, and K^B is an ultimate octahedral shear strength. Equation (2.3) leads to the following expression of a compressive failure criterion, which is applicable for brittle to ductile materials,

$$K_O = K^A + (K^B - K^A) [1 - \exp(-\alpha \sigma_m)], \quad (2.4)$$

where K^A is an unconfined octahedral shear strength. During strain softening, the strength of rock decreases or deteriorates. The ultimate deterioration of the material is defined as the state at which the inter-crystalline cohesive bonds are completely lost, as in a mass of loose sand. The strength K_O in this state then becomes the residual

strength K^R , which reflects the internal friction strength in the pulverized mass, given by the function of confinement σ_m ,

$$K^R = K^B \sigma_m/P, \quad (2.5)$$

where K^B/P is friction tangent ($\tan \phi$), P is the plastic transition pressure, and ϕ is the angle of internal friction. Rock deterioration progresses from the intact to the residual strength (K_O to K^R) with an increase in the excess octahedral shear strain $\Delta\gamma_O$. The K_O of the deteriorated rock can be determined by adding the residual strength K^R to the variable portion ΔK_O , which varies from 0 to 100 %, depending on the amount of the deterioration. Thus the strength can be defined as,

$$K_O = f_D \Delta K_O + K^R, \quad (2.6)$$

where f_D is the deteriorating function and ΔK_O is the variance portion of the strength which equals $[K^A + (K^B - K^A) (1 - \exp(-\alpha\sigma_m))] - K^R$. f_D can be related to the excess octahedral shear strain as,

$$f_D = \exp[-C(\gamma_O - \gamma_C)/\gamma_C]; \gamma_O > \gamma_C, \quad (2.7)$$

where C is a deterioration coefficient, γ_C is a critical strain of elastic limit, and γ_O is the induced octahedral shear strain. By introducing equation (2.7) into equation (2.6), the strength deterioration function describing the strain-softening behavior of rock after γ_O exceeds γ_C , can be established,

$$K_O = \exp[-C(\gamma_O - \gamma_C)/\gamma_C] \{ [K^A + (K^B - K^A) (1 - \exp(-\alpha\sigma_m))] - K^B \sigma_m/P \} + K^B \sigma_m/P. \quad (2.8)$$

For viscoelastic behavior (VE), its state is defined as the state in which the octahedral shear stress τ_{oct} is less than the octahedral shear strength K_o . No viscoplastic creep tanks place in this state. The VE strain can be directly identified using the results from creep testing (Serata et al., 1991). The time-dependent strain resulting from viscoelastic creep can best be described by a set of three or more Kelvin components as,

$$\begin{aligned}\gamma_{total}^{VE} &= \gamma_{23}^{VE} + \gamma_{22}^{VE} + \gamma_{21}^{VE} \\ &= (\tau_o/\eta_{21}) \exp(-G_{21}t/\eta_{21}) + (\tau_o/\eta_{22}) \exp(-G_{22}t/\eta_{22}) \\ &\quad + (\tau_o/\eta_{23}) \exp(-G_{23}t/\eta_{23})\end{aligned}\tag{2.9}$$

where $\gamma_{23}^{VE}, \gamma_{22}^{VE}, \gamma_{21}^{VE}$ = short-, medium-, and long-term viscoelastic strain rates; G_{21}, G_{22}, G_{23} = retarded shear moduli for short-, medium-, and long-term VE strain; $\eta_{21}, \eta_{22}, \eta_{23}$ = elastoviscosity coefficients for short-, medium-, and long-term VE strains.

Figure 2.1 shows the behavioral system of GEO model. The formulation separates the octahedral shear stress-strain (σ_m - ϵ_m) relation. These relations act in parallel and are related via failure and post-failure conditions (i.e. deterioration coefficient C). The program carries out the explicit time-domain integration, and hence allows updating the element strength and state (elastic or plastic) through different time steps. The formulation is designed such that when the induced shear strain (γ_o) is less than the critical shear strain (γ_c), element behaves as an elastic or visco-elastic, and does not dilate. Immediately after γ_o exceeds γ_c and σ_m is less than

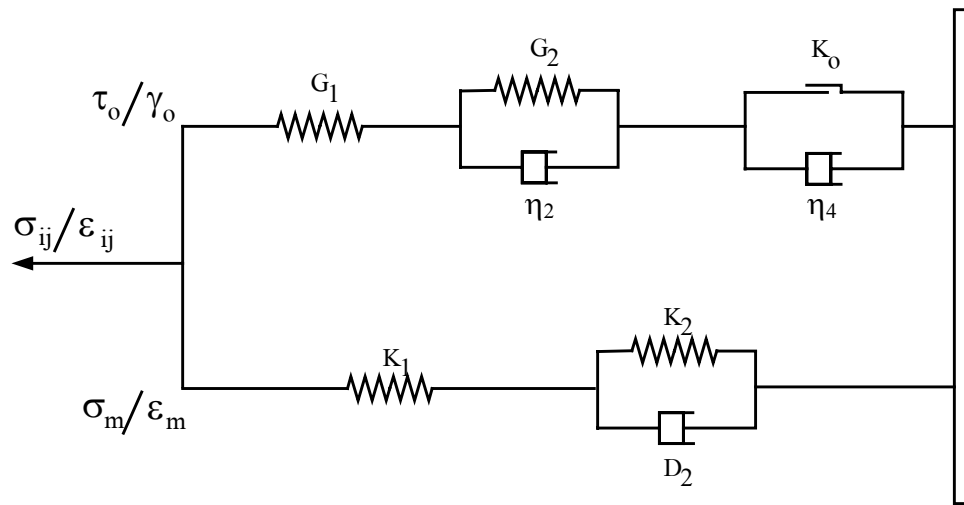


Figure 2.1 Modular component of GEO constitutive equation (Modified from Serata and Fuenkajorn, 1993).

P , K_O decreases, and results in a strain-softening behavior. Under this condition, the calculation for a new failure surface and volumetric dilation will be carried out for that particular element. The new K_O is then returned to the main algorithm to compare with the current stress state. The calculated ε_{VD} is added to the elastic and plastic strain components in the minimum principal stress direction. Under large confinements ($\sigma_m > P$), the strength will not deteriorate, and dilation will not occur. The element may deform in strain hardening mode or may flow plastically, depending on the amount of γ_o .

2.6 Rock salt in the Maha Sarakham Formation

This section summarizes the geology of the salt in the Maha Sarakham Formation where the core samples have been obtained

Figure 2.2 shows the typical stratigraphic column of the Maha Sarakham Formation. The salt is in the Late Cretaceous (Hansen et al., 2002). At one time, there existed a single giant evaporate basin encompassing at least the area of the present day: Sakon Nakhon and Khorat Basins (Figure 2.3). These deposits represent one of the last saline giants preserved in the South-East Asia and suggest an extreme arid period during Cretaceous time. The sequence lacks $MgSO_4$ salts are in indicating a likely continental/basinal brine source (Warren, 1999). The Maha Sarakham Formation is 250 meters thick on average, and is composed of three distinctive evaporite units which are the Lower Salt, the Middle Salt and the Upper Salt members (Suwanich, 1986). Petrographic study of the cores collected from the salt members has been described and compiled by Suwanich and Ratanajaruraks (1982) and Suwanich (1986).

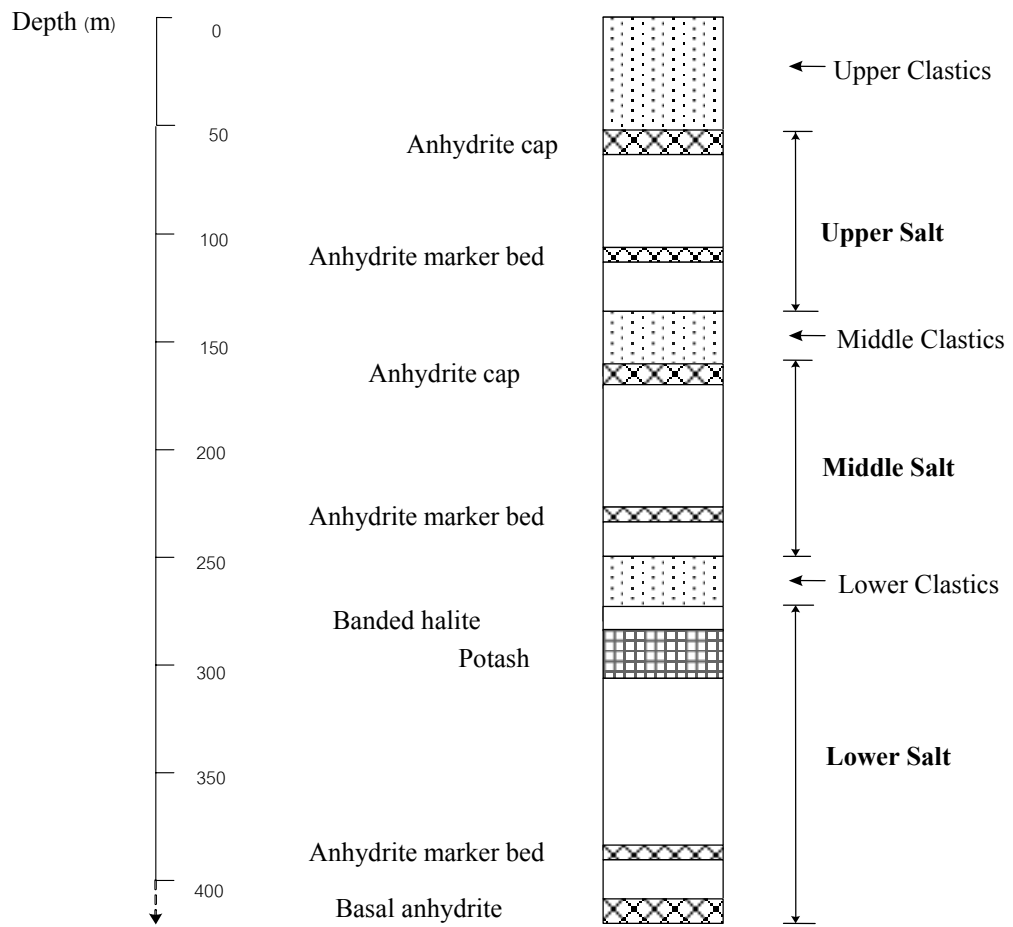


Figure 2.2 A typical section of the Maha Sarakham Formation (Modified from Suwanich, 1986).

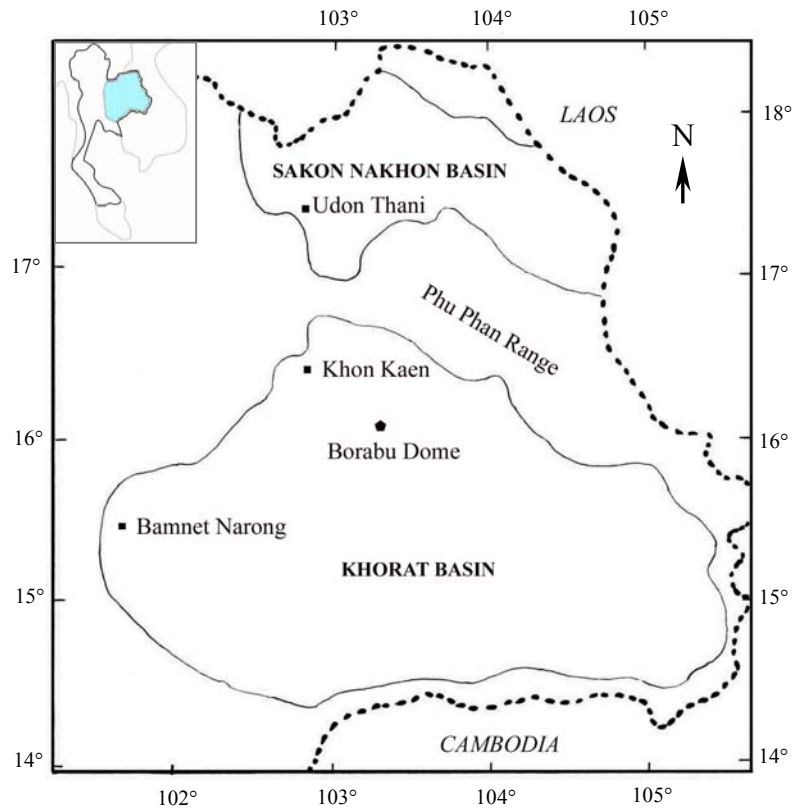


Figure 2.3 Korat and Sakon Nakhon salt basins in the northeast of Thailand.

(Modified from Japan International Cooperation Agency, 1981)

The core samples used in this research are obtained from the Middle Salt and Lower Salt. Suwanich (1986) states that the texture of upper part of Middle Salt is white and clear. The crystals are tightly interlocked. The orange carnallites are rarely found. The white and clear halite change to pale, medium and dark honey when the depths increase. The diameters of milky white halite are range from 0.1 to 0.3 centimeters and shows flow texture. Smoky dark halite is associated with anhydrite. The large recrystallized glassy halite is found interlayered with honey halite. The middle part of Middle Salt is moderate honey halite interbedded with smoky dark halite and anhydrite stringers. Minor orange halite is also found. Smoky dark bands of halite constitute 15 to 20%, and milky white halite is about 30 to 40%. The crystals of milky white halite are 0.5 to 1.0 centimeters in diameter. Flowage texture is common in this part and a flattened grain is 0.1 to 0.2 centimeter wide and 1.0 centimeter long. The lower part is moderate to dark honey halite containing dark orange and smoky dark halite bands. The associated mineral include local occurrence of sylvite and carnallite. Anhydrite stringers and milky white halite are rare or absent.

For the Lower Salt, the upper part is below the potash zone. It shows glassy-white, colorless or white halite. The crystal size is usually from 0.2 to 0.5 centimeters in diameter. However, some large crystals in the range from 2.0 to 5.0 centimeters locally occurred. The color of halite changes gradually from white to gray with 1 to 2 % of milky halite grained. In the middle part of Lower Salt, the milky white halite increases with depth and the crystal diameter increases from 0.3 to 0.7 centimeter. The amount of smoky dark halite is also increasing with the depth. The lower part shows flattened halite grains due to flowage. The salt forms sheets that break easily along the flowage directions.

CHAPTER III

LABORATORY EXPERIMENTS

3.1 Introduction

Two test schemes have been performed to investigate the mechanical and rheological properties of rock salt specimens. The characterization tests are conducted including the uniaxial compressive strength tests, Brazilian tensile strength tests and the triaxial compressive strength tests. To determine the creep parameters, the conventional triaxial creep test and the radially unloaded triaxial creep test have been carried out. All experiments are conducted under the scope and limitations of the study proposed in the first chapter. This chapter describes the sample preparation, test methods and results.

3.2 Sample Preparation

Core samples of salt are donated by Asia Pacific Potash Corporation, Udon Thani province. They have been collected from borehole number of BD99-1 located at Muang district (Figure 3.1). All samples are obtained from the Middle Salt and the Lower Salt members at depths between 250 meters and 650 meters in the Sakon Nakhon Basin. The cores as obtained are shown in Figure 3.2. Their diameter is 60 millimeters. They are cut to desired length using a standard cutting saw (Figure 3.3). A lathe is used to machine the triaxial test specimens (Figure 3.4). The dimensions of the test specimens are measured with vernier caliper to the nearest 0.02 millimeter.



Figure 3.1 Locations where the core samples are obtained and where the geologic sequences are used in the computer modeling.

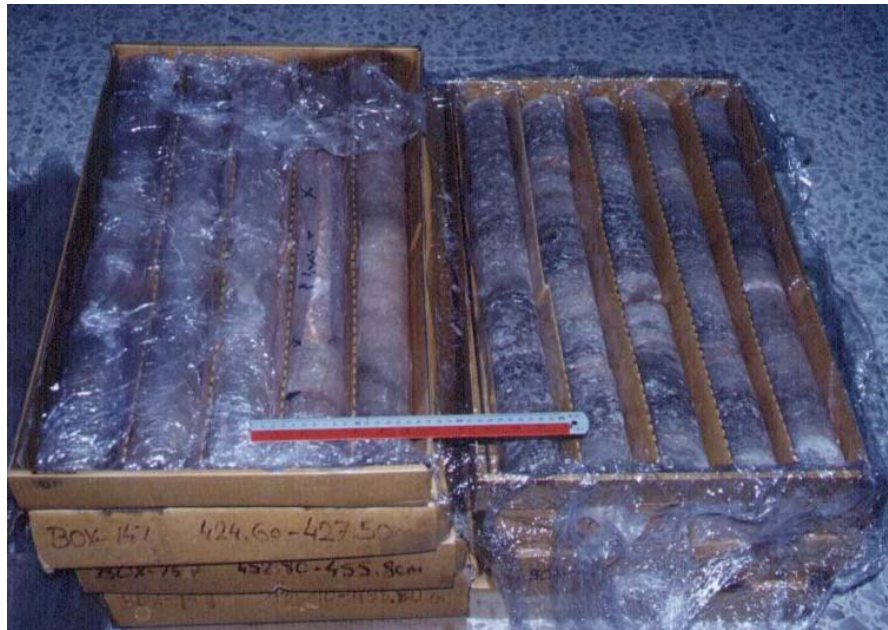


Figure 3.2 Some salt cores used in this research. They are donated by Asia Pacific Potash Corporation, Udon Thani province, Thailand.



Figure 3.3 A salt core is cut to desired length using cutting machine.

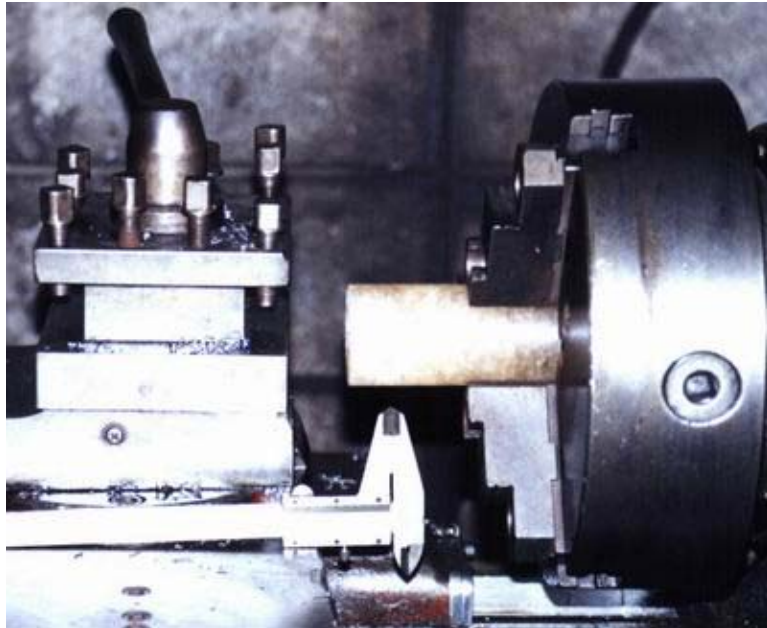


Figure 3.4 A salt specimen is machined to obtain specified dimensions for the triaxial tests.

The weight is measured to the nearest 0.1 g. Before testing, the borehole number, depth, dimensions, density and petrography are described. The specimen designation is identified (Figure 3.5). The prepared samples are wrapped with plastic sheet to prevent from moisture. The preparation procedure follows, as much as practical, the ASTM standard (ASTM D4543-85). The dimension requirements for each testing follow both the ASTM standards and the ISRM suggested methods.

The salt specimens are mostly dense honey halite. Milky white halite is about 10 to 30% of specimen volume. The smoky halite crystals are about 10%. The crystal sizes are from 0.5 to 3.0 millimeters. Non-uniform distribution of inclusions found includes anhydrite, clay, and iron oxides. The anhydrites are about 5% and the rest is less than 3% of specimen volume.

3.3 Characterization Tests

3.3.1 Uniaxial Compressive Strength Tests

The objective of uniaxial compressive strength tests is to determine the ultimate strength and the deformability of the salt specimens under uniaxial compression. The test procedures follow the ASTM standard (ASTM D2938-95) and the suggested methods by ISRM (Bieniawski et al., 1978). Five salt cylinders have been tested. They are from the depths between 265 and 625 meters. The nominal diameter is 60 millimeters with length-to-diameter ratio of 2.4-2.7.

3.3.1.1 Test Procedures

The test is performed by applying uniform axial stress to the salt cylinder and measuring the increase of axial strains as a function of time. The constant stress rate is maintained about 0.16 MPa/second by a compression machine.

BD99 - 1 - CTC - 3e



Borehole Name Borehole Number Test Type Specimen Number



- UX** = Uniaxial Compressive Strength Test
- BZ** = Brazilian Tensile Strength Test
- TS** = Triaxial Compressive Strength Test
- CTC** = Conventional Triaxial Creep Test
- RUTC** = Radially Unloaded Triaxial Creep Test

Figure 3.5 Specimen designations for each test type.

The maximum capacity of the compression machine (Elect/ADR2000 model) is 2000 kN (Figure 3.6). The axial displacements are monitored by dial gauges with a precision of 0.001 inch. The test is performed at room temperature. The specimen is loaded until failure which normally occurs within 15 minutes. Characteristics of the post-tested specimens are observed. Photographs are taken.

3.3.1.2 Test Results and Discussions

The uniaxial compressive strengths of the rock salt are summarized in Table 3.1. The strength (σ_c) is calculated from the applied axial load assuming that the specimen diameter does not change as the load increases (i.e. engineering stress). The following equation is used,

$$\sigma_c = P_{uf}/A \quad (3.1)$$

where P_{uf} is the failure load and A is the initial cross-sectional area. The axial strain (ϵ_{axial}) is calculated from the equation,

$$\epsilon_{axial} = \Delta l/l_0 \quad (3.2)$$

where Δl the axial deformation (positive for contraction) and l_0 is the original specimen length.

Figure 3.7 plots the stress-strain curves for all specimens. All specimens behave as a nonlinear material. The average strength is 34.7 ± 2.2 MPa. The strengths of the Maha Sarakham salt are relatively high as compared with those from other sources in the United States and Germany (Figure 3.8). This is probably due to the significant amount and non-uniform distribution of the inclusions and due to relatively large crystal sizes compared to the specimen diameter. The extension failure mode is observed. In the mid-length of some specimens, micro cracks are

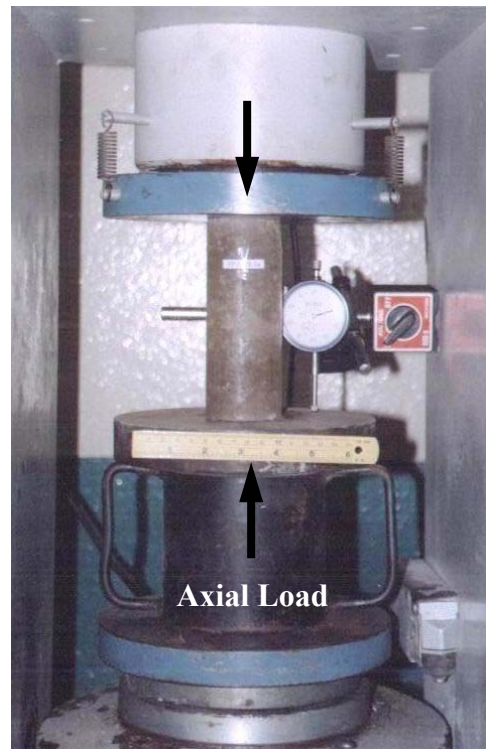


Figure 3.6 A compression machine (Elect/ADR2000 model) is used in the uniaxial compressive strength tests.

Table 3.1 Summary of test results from the uniaxial compressive strength testing.

Specimen No.	Average Diameter D_s (mm)	Average Length L (mm)	Depth (m)	Loading Rate (MPa/s)	Failure Load P_{uf} (kN)	Uniaxial Compressive Strength σ_c (MPa)	Failure Strain ϵ_f
BD99-1-UX01e	61.07	148.52	328.45 (MS)	0.16	108.4 6	37.07	0.051
BD99-1-UX02e	60.77	163.97	264.28 (MS)	0.16	94.63	32.65	0.037
BD99-1-UX03e	60.78	147.35	265.25 (MS)	0.16	109.1 9	36.93	0.046
BD99-1-UX05e	60.97	150.30	323.42 (MS)	0.16	99.34	34.03	0.041
BD99-1-UX06e	61.13	161.43	324.80 (MS)	0.16	96.01	32.74	0.039
Average Uniaxial Compressive Strength				34.68 ± 2.21 MPa ($5,030 \pm 321$ psi)			

Note: MS = Middle Salt

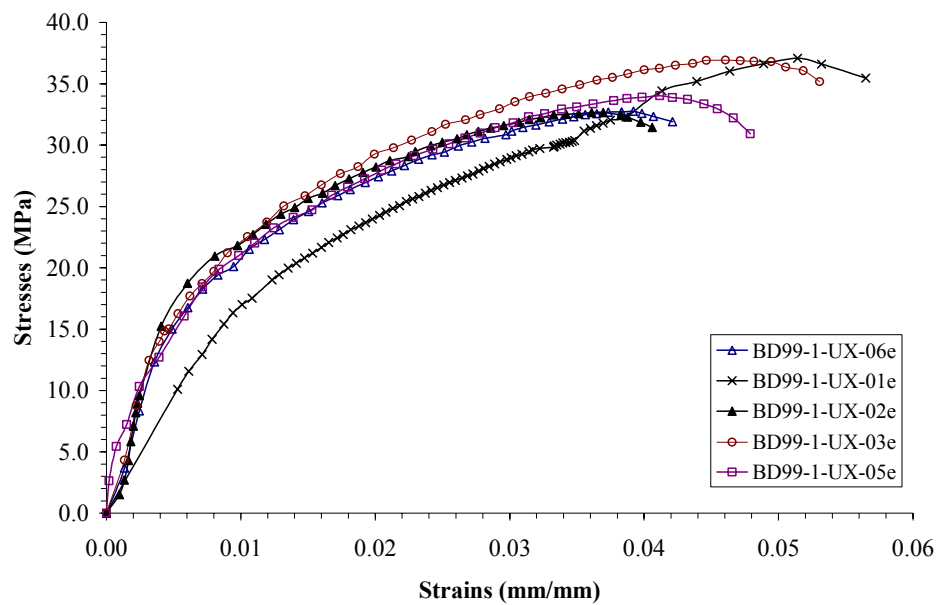


Figure 3.7 Results of uniaxial compressive strength test. The axial stresses are plotted as a function of axial strain.

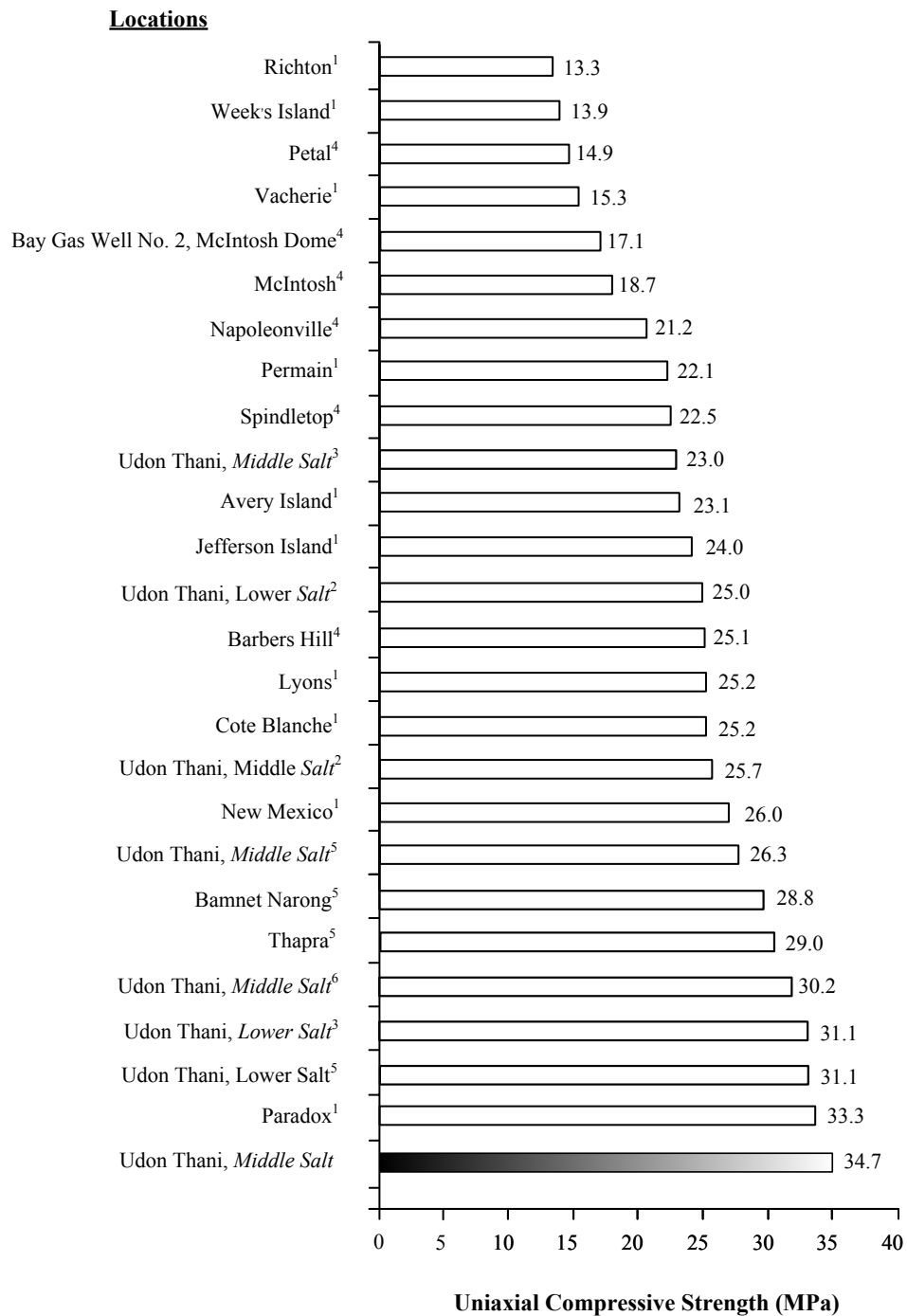


Figure 3.8 Comparison of the uniaxial compressive strength of salt tested here (shaded bar) with the results obtained from various sources (¹ Hansen et al., 1984; ² Bootongloan, 2000; ³ Wetchasat, 2002; ⁴ DeVries et al., 2002; ⁵ Fuenkajorn and Jandakaew, 2003 and ⁶ Phueakphum, 2003)

generated as detected by milky fragments of salt. This induces the radial expansion and the specimen dilation. Some cracks are extended parallel to the specimen axis. Photograph of some failed specimens is given in Figure 3.9, showing the failure plane making 60 degrees from the specimen axis.

3.3.2 Brazilian Tensile Strength Tests

The Brazilian tensile strength tests determine the indirect tensile strength of the salt specimens. The specimens are collected from depths between 250 and 405 meters. The test is performed in accordance with the ASTM standard (ASTM D3967-95) and the ISRM suggested methods (Bieniawski and Hawkes, 1981). Twenty salt specimens have been tested. They have a nominal diameter of 60 millimeters with a length-to-diameter ratio of 0.5.

3.3.2.1 Test Procedures

The Brazilian tension test is conducted by applying diametrical load to the salt specimen. The constant stress rate is maintained about 0.1 MPa/second. The SBEL PLT-75 loading machine is used. Its maximum capacity is 350 kN. The laboratory arrangement is shown in Figure 3.10. The test is conducted at room temperature. The load is applied until failure which normally occurs under 2 minutes. Characteristics of the post-tested specimens are observed and photographed.

3.3.2.2 Test Results and Discussions

Table 3.2 shows the tensile strength results. The tensile strengths (σ_B) are calculated by the following formula,

$$\sigma_B = 2P_{bf}/\pi LD_s \quad (3.3)$$



Figure 3.9 Some post-tested specimens (BD99-1-UX01e and UX05e), failed at 37.07 MPa and 34.03 MPa. In the mid-length of the specimens, micro-cracks develop as indicated by milky fragments of the salt. Failure plane makes an angle of 60 degrees with the specimen axis.

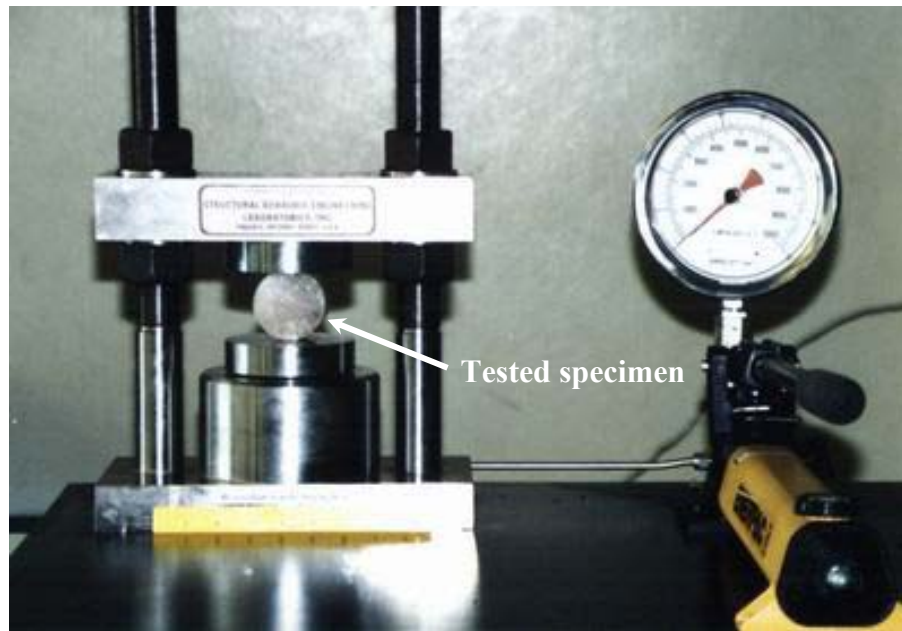


Figure 3.10 Laboratory arrangements for the Brazilian tensile strength test. SBEL PLT-75 loading machine with the maximum capacity of 350 kN is used.

Table 3.2 Summary of test results from the Brazilian tensile strength testing.

Specimen No.	Average Diameter D_s (mm)	Average Length L (mm)	Depth (m)	Failure Load P_{ur} (N)	Brazilian Tensile Strength σ_B (MPa)
BD99-2-BR-01e	61.27	33.50	329.13 (MS)	8.50	2.37
BD99-1-BR-02e	58.12	31.08	253.93 (MS)	6.50	2.06
BD99-1-BR-03e	60.85	36.08	254.05 (MS)	6.50	1.69
BD99-1-BR-04e	60.70	31.83	252.60 (MS)	5.00	1.48
BD99-2-BR-05e	61.13	31.82	329.18 (MS)	6.00	1.77
BD99-1-BR-06e	61.22	37.00	390.84 (LS)	8.00	2.02
BD99-2-BR-07e	60.82	35.55	405.00 (LS)	7.50	1.99
BD99-1-BR-08e	60.57	31.88	262.60 (MS)	7.50	2.22
BD99-1-BR-09e	61.40	43.60	392.30 (LS)	4.00	0.86
BD99-1-BR-10e	58.32	34.73	254.12 (MS)	6.00	1.70
BD99-2-BR-11e	60.77	32.52	404.15 (LS)	5.00	1.45
BD99-1-BR-12e	60.93	37.65	264.15 (MS)	9.50	2.37
BD99-1-BR-13e	58.98	37.30	254.07 (MS)	7.50	1.95
BD99-2-BR-14e	61.17	29.52	404.95 (LS)	6.00	1.90
BD99-1-BR-15e	60.72	34.68	254.09 (LS)	5.00	1.36
BD99-2-BR-16e	61.07	27.35	323.35 (LS)	7.00	2.40
BD99-2-BR-17e	60.78	30.37	328.63 (LS)	7.50	2.33
BD99-1-BR-18e	61.27	32.90	443.69 (MS)	5.00	1.42
BD99-1-BR-19e	61.22	32.30	443.78 (MS)	5.50	1.59
BD99-1-BR-20e	61.13	31.92	443.84 (MS)	3.50	1.03
Average Brazilian Tensile Strength (MS)			1.97 ± 0.37 MPa (286 ± 54 psi)		
Average Brazilian Tensile Strength (LS)			1.53 ± 0.43 MPa (222 ± 62 psi)		

Note: MS = Middle Salt

LS = Lower Salt

where P_{bf} is the applied load at failure indicated by the testing machine, L is the thickness of specimen, and D_s is the diameter of specimen.

The average tensile strengths of the specimen obtained from the Middle Salt and the Lower Salt members are 1.97 ± 0.37 MPa and 1.53 ± 0.43 MPa, respectively. The strengths are in the same range with the test results from other sites (Figure 3.11). Failure surface along diameter load appears clear which reflects the tensile stress initiation. Contact zones between the platens and the specimen are spited to form rock wedges created in the final splitting phase. This agrees with other investigator (Andreev, 1995). The standard deviations of the tensile strengths for the Middle Salt and the Lower Salt member are 0.43 MPa (28%) and 0.37 MPa (18%), respectively. The large variations may be cause by non-uniform distribution of the inclusions. In addition, the salt crystals are relatively large as compared to the specimen diameter. The average crystal size of the salt is 10x10x10 millimeters and some specimens are 15x20x20 millimeters. A high tensile strength is obtained if the tensile crack is induced through the salt crystals or if the crystals align in the loading direction. A lower strength is obtained if the cracks are induced along the crystal boundaries. This suggests that the tensile strength of the inter-crystalline boundaries is lower than that of salt crystals. This agrees with those observed by Fuenkajorn and Daemen (1988). Photograph of some failed specimens is given in Figure 3.12.

3.3.3 Triaxial Compressive Strength Tests

The purpose of the triaxial compressive strength test is to determine the strength of the salt specimens under the triaxial stress states. Other properties are also determined, including the Poisson's ratio, the internal friction angle and the cohesion. In addition, the deformation characteristics, failure mode, and the effect of confining pressure are observed. The specimens are collected from depths between 250 and 445 meters.

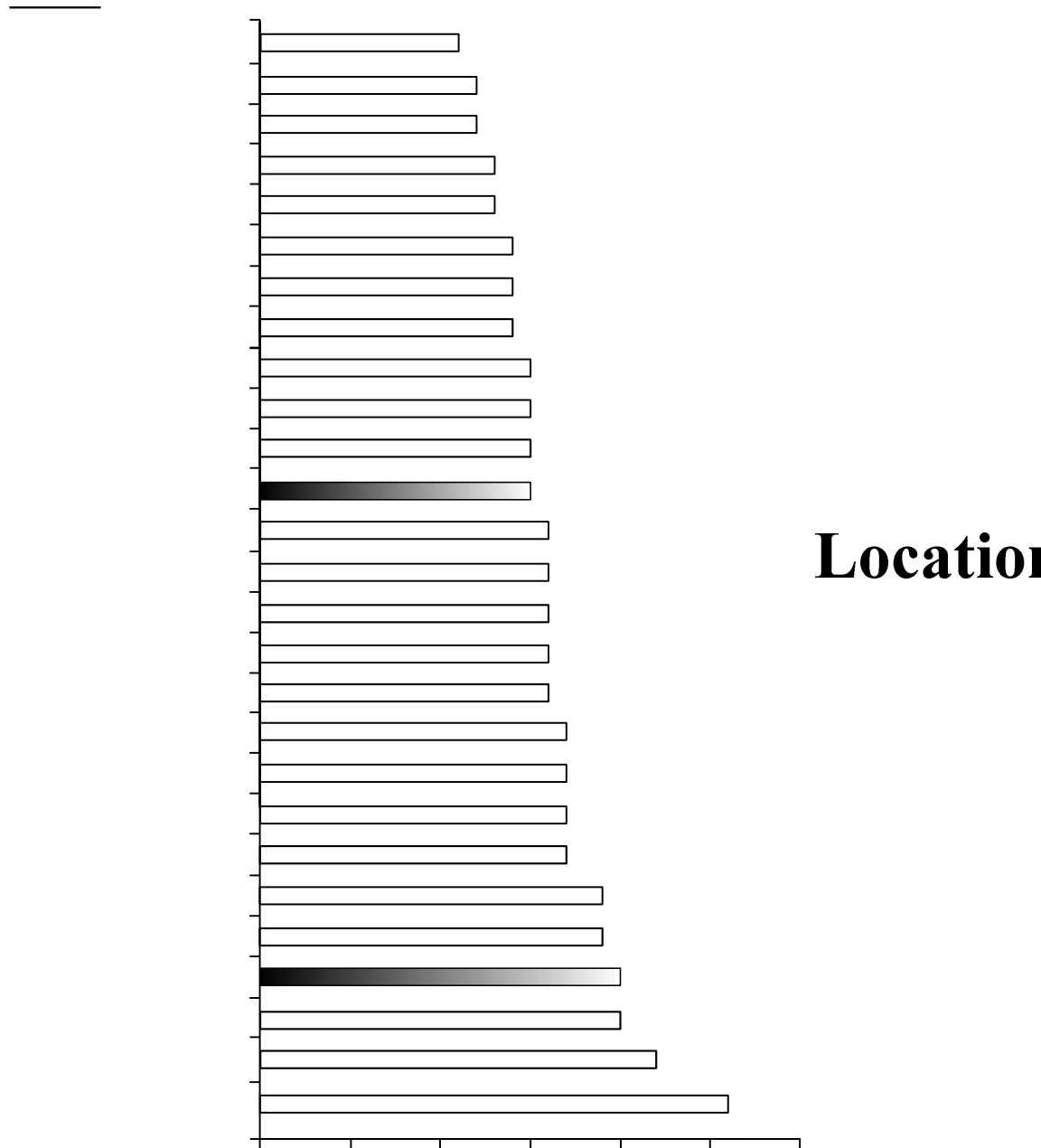


Figure 3.11 Comparison of the Brazilian tensile strength obtained here (shaded

bars) with the results obtained from various sources (¹Hansen et al., 1984; ²Bootongloan, 2000; ³Wetchasat, 2002; ⁴DeVries et al., 2002; ⁵Fuenkajorn and Jandakaew, 2003 and ⁶Phueakphum, 2003).

Bay Gas Well No. 2,



Figure 3.12 The Brazilian test specimens after failure. Tensile crack is induced along the loading diameter. The failure plane cuts through the salt crystals.

The test is performed in accordance with the ASTM standard (ASTM D2664-95) and the ISRM suggested methods (Vogler and Kovari, 1978). Seven salt specimens have been tested. They have a nominal diameter of 54 millimeters with a length-to-diameter ratio of 2.0. The constant confining pressure for this test ranges from 5.5 to 19.3 MPa (800-2800 psi).

3.3.3.1 Test Procedures

The triaxial compressive strength test is performed by applying compressive stress parallel to the specimen axis and confining pressures around the salt cylinder. The axial stress continuously increases while the confining pressures are maintained constant. The axial load is applied by a compression machine (Elect/ADR2000 model). Its maximum capacity is 2000 kN. A Hoek cell (Hoek and Franklin, 1968) is used as a triaxial chamber. The specimen is enclosed in a rubber jacket and pressurized by hydraulic oil. To determine axial strain, the axial deformations are monitored by dial gauges with a precision of 0.001 inch. The volumetric strains are measured by measuring the change of oil volume. The laboratory arrangement is shown in Figure 3.13. The test is performed at the room temperature. The axial load is applied until failure which normally occurs within 5-10 minutes. Characteristics of the post-tested specimens are observed and photographed.

3.3.3.2 Test Results and Discussions

Table 3.3 presents the results of triaxial testing. The cohesion and the internal friction angle can be calculated by Coulomb criterion,

$$\tau = c + \sigma \tan \phi \quad (3.4)$$

where τ is shear strength at various confining pressures, c is the cohesion intercept, σ is the normal stress, and ϕ is the internal friction angle. These parameters are

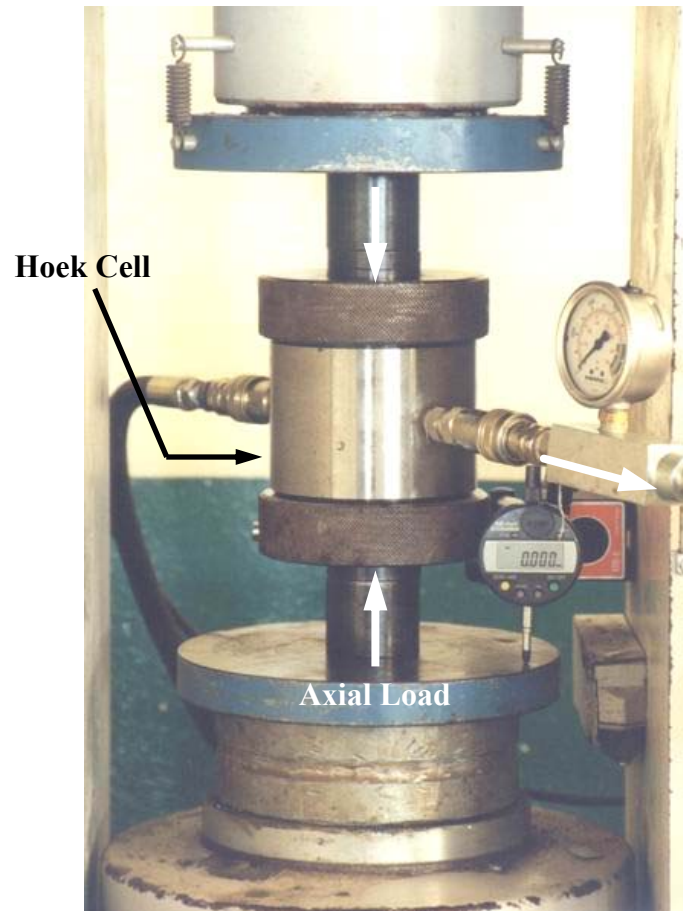


Figure 3.13 A compression machine (Elect/ADR2000 model) and a Hoek cell are used for the triaxial testing.

Table 3.3 Summary of test results from the triaxial compressive strength testing.

Specimens No.	Average Diameter D_s (mm)	Average Length L (mm)	Depth (m)	Axial Stress at Failure σ_1 (MPa)	Constant Confining Pressure σ_3 (MPa)	Average Poisson's Ratio ν
BD99-1-TS-3e	55.17	110.28	421.50 (LS)	79.1	14.1	-
BD99-1-TS-4e	54.00	109.97	250.43 (MS)	94.2	6.9	0.46
BD99-1-TS-5e	53.88	109.91	249.88 (MS)	82.4	5.5	0.35
BD99-1-TS-9e	53.55	107.39	249.71 (MS)	113.7	12.4	0.35
BD99-1-TS-10e	53.73	107.24	208.82 (MS)	125.4	15.2	0.34
BD99-1-TS-12e	52.78	105.90	426.95 (LS)	142.5	19.3	0.37
BD99-1-TS-13e	52.87	106.24	326.92 (MS)	108.9	8.3	0.32

Note: The Poisson's ratio calculated from unloading curves.

MS = Middle Salt

LS = Lower Salt

determined by graphical method which presents in the normal-shear stress diagram (Figure 3.14). The volumetric strain is monitored from the oil volume change in the confined chamber while the confining pressure is held constant. It can be calculated by equations,

$$V_{oil} = V_{steel} + (V_m - V_{ro}) \quad (3.5)$$

where V_{oil} is the hydraulic oil bleeding from the Hoek cell, V_{steel} is the volume of the moving steel platen, V_m is the new rock volume, and V_{ro} is the original rock volume. For this relation, volumetric strain (ε_{vol}), lateral strain (ε_{lat}) and axial strain (ε_{axial}) can be determined as follows.

$$\varepsilon_{vol} = (V_m - V_{ro}) / V_{ro}, \quad (3.6)$$

$$\varepsilon_{axial} = (L_m - L_{ro}) / L_{ro}, \quad (3.7)$$

$$\varepsilon_{lat} = (D_m - D_{ro}) / D_{ro} \quad (3.8)$$

where L_m is the new length, L_{ro} is the original length, D_m is the new diameter, and D_{ro} is the original diameter of specimen.

The test results are plotted in the differential stress-strain diagram showing the axial, lateral and volumetric strains in Figures 3.15 to 3.20. The Poisson's ratio can be calculated by the relations given by Jaeger and Cook (1979),

$$\sigma_1 = (\lambda + 2G_1) \varepsilon_1 + \lambda\varepsilon_2 + \lambda\varepsilon_3, \quad (3.9)$$

$$\sigma_3 = \lambda\varepsilon_1 + \lambda\varepsilon_2 + (\lambda + 2G_1) \varepsilon_3 \quad (3.10)$$

where σ_1 is the maximum principal stress (axial stress), σ_3 is the minimum principal stress (confining stress), ε_1 is the major principal strain, and ε_3 is the minor principal)

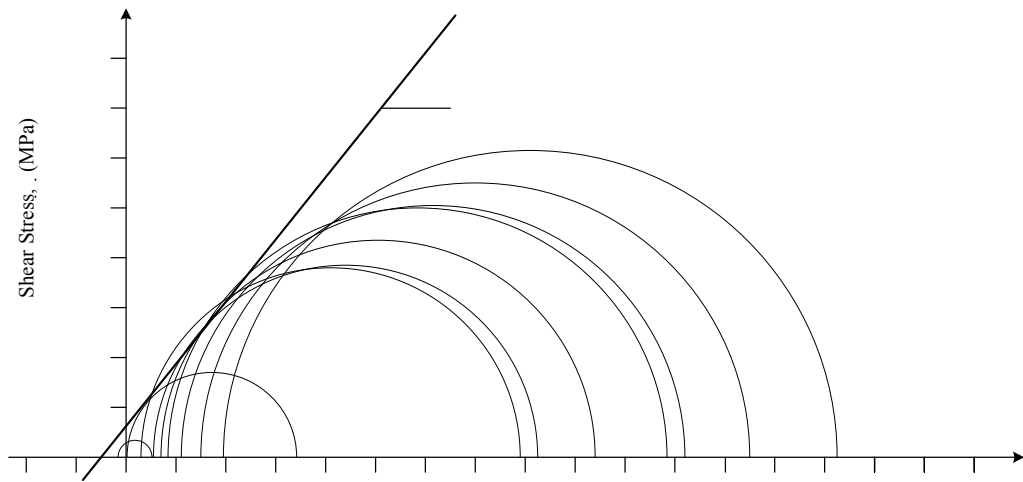


Figure 3.14 Mohr circles and Coulomb criterion used to represent the triaxial compressive strengths.

80

60

 τ

40

20

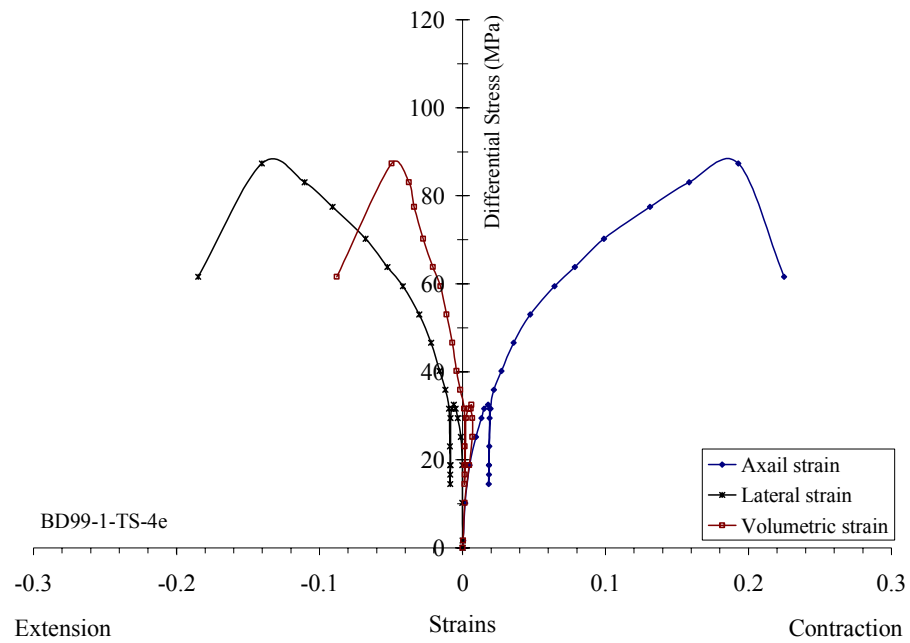


Figure 3.15 Differential stress ($\sigma_1 - \sigma_3$) versus strains from triaxial test result at confining pressure of 6.9 MPa.

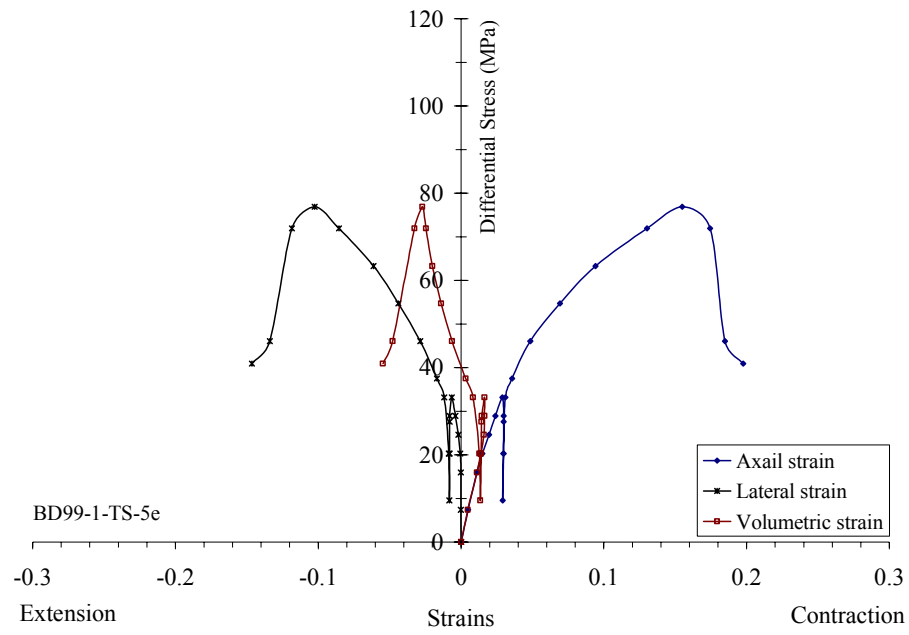


Figure 3.16 Differential stress ($\sigma_1 - \sigma_3$) versus strains from triaxial test result at confining pressure of 5.5 MPa.

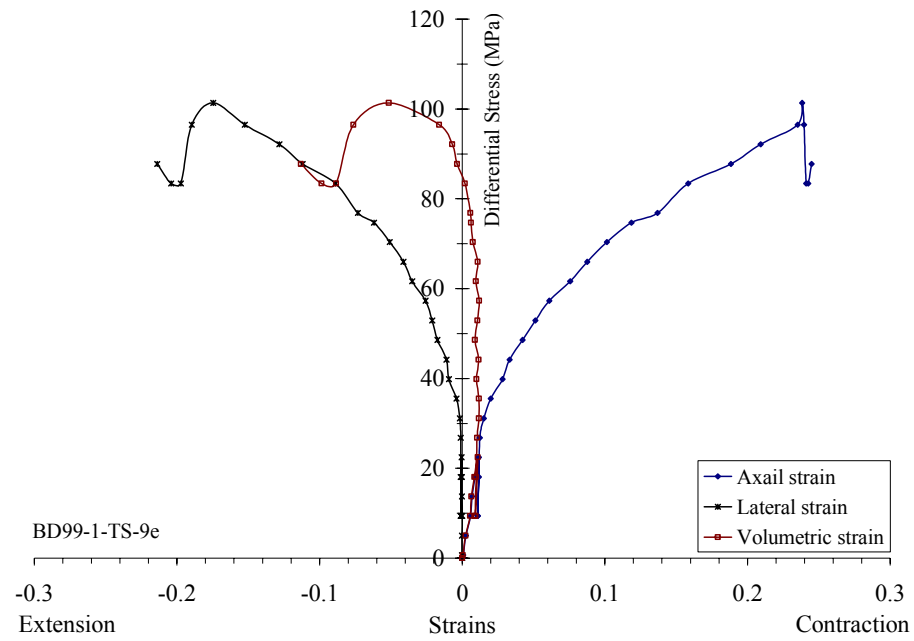


Figure 3.17 Differential stress ($\sigma_1 - \sigma_3$) versus strains from triaxial test result at confining pressure of 12.4 MPa.

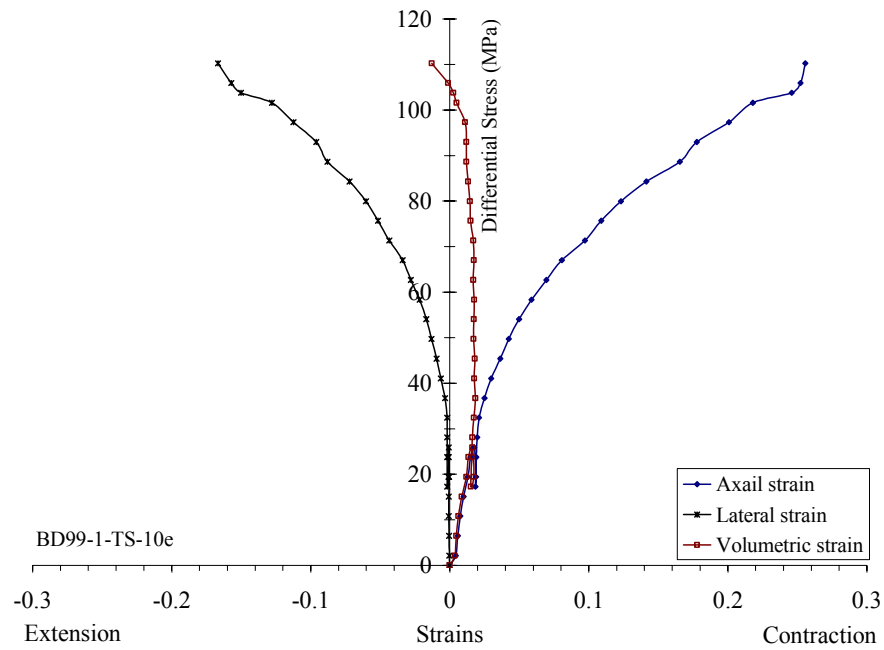


Figure 3.18 Differential stress ($\sigma_1 - \sigma_3$) versus strains from triaxial test result at confining pressure of 15.2 MPa.

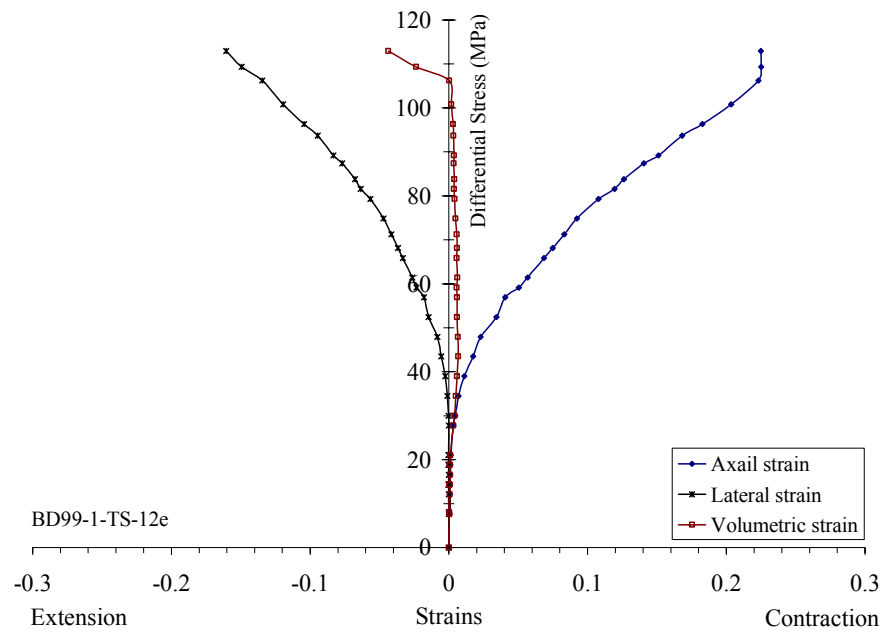


Figure 3.19 Differential stress ($\sigma_1 - \sigma_3$) versus strains from triaxial test result at confining pressure of 19.3 MPa.

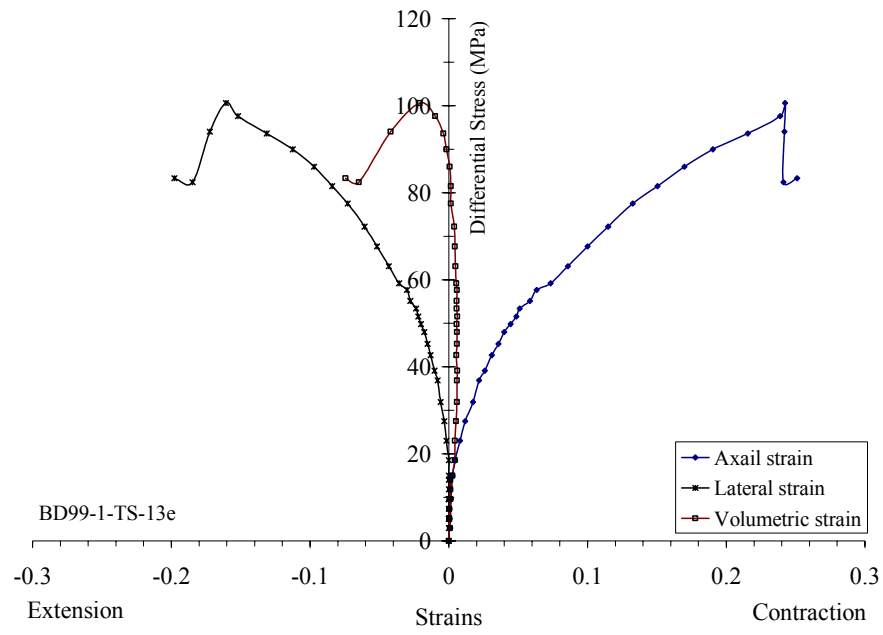


Figure 3.20 Differential stress ($\sigma_1 - \sigma_3$) versus strains from triaxial test result at confining pressure of 8.3 MPa.

strain, G_1 is the shear modulus, and λ is Lamé constant. The minor and intermediate principal stresses are equal ($\sigma_3 = \sigma_2$). It can be written as,

$$\sigma_1 = (\lambda + 2 G_1) \varepsilon_1 + 2\lambda\varepsilon_3, \quad (3.11)$$

$$\sigma_3 = \lambda\varepsilon_1 + \lambda\varepsilon_2 + (\lambda + 2 G_1)\varepsilon_3. \quad (3.12)$$

The equations (3.11) and (3.12) can be substituted by λ and G constants,

$$G_1 = [(\sigma_1 - \sigma_3) / (\varepsilon_1 - \varepsilon_3)] / 2, \quad (3.13)$$

$$\lambda = (\sigma_1 - 2 G_1\varepsilon_1) / (\varepsilon_1 + 2\varepsilon_3). \quad (3.14)$$

From the general relation of linearly elastic, it can be expressed as:

$$\lambda / G_1 = 2\nu / (1 - 2\nu), \text{ or} \quad (3.15)$$

$$\nu = \lambda / 2(G_1 + \lambda). \quad (3.16)$$

Then the Poisson's ratio where the minor and intermediate principal stresses are equal ($\sigma_3 = \sigma_2$), can be written as:

$$\nu = \frac{\{(\sigma_1 - 2 G_1\varepsilon_1) / (\varepsilon_1 + 2\varepsilon_3)\} / \{[(\sigma_1 - \sigma_3) / (\varepsilon_1 - \varepsilon_3)] + 2[(\sigma_1 - 2 G_1\varepsilon_1) / (\varepsilon_1 + 2\varepsilon_3)]\}}{1} \quad (3.17)$$

The Poisson's ratio is determined by unloading curve (ASTM D5407-95).

Table 3.3 summarizes the dimensions, test parameters and the results of the triaxial tests. The average Poisson's ratio for six salt specimens is 0.37 using the Coulomb criterion, the cohesion is 6.0 MPa and the internal friction angle is 50 degrees.

The post-tested specimens show different modes of failure depending on the magnitude of the confining pressures. The shear failure exhibits

when the specimen subjected to low confining pressures (5.5, 6.9, 8.3, 12.4 and 14.1 MPa). The failure planes make the angle between 45 and 80 degrees with the core axis (Figure 3.21). The multiple shear failure appears on the specimens when subjected to high confining pressures (15.2 and 19.3 MPa). The differences between the original diameters and the final diameter of the salt specimens are between 15 and 26%. The volumetric expansion or dilation is described by the stress-strain curves (Figures 3.15 to 3.20). The initiation of the volumetric dilation occurs in positive values (specimen under contraction). This phenomenon implies that the salt crystals are compacted by the axial load before the radial expansion of the specimen starts. After that, the volumetric dilation rapidly changes to negative particularly when specimen subjected to low confining pressures. The change is more gradual when the specimen subjected to high confining pressure. The volumetric strains are changed from positive to negative at the axial strains between 0.0107 and 0.0587. This transition (positive to negative value) has been observed by many investigators (Dreyer, 1972; Price, 1979; Lux and Rokahr, 1984; Fuenkajorn and Daemen, 1988; and Fuenkajorn and Serata, 1993). Jaeger and Cook (1979) suggest that this phenomenon occurs due to the initiation of micro-cracks. Beyond this point, the dilation increases as the deviatoric stress increases.

Figures 3.22 to 3.24 compare the triaxial compressive strength obtained here with those obtained elsewhere, in terms of cohesion, internal friction angle, and Poisson's ratio. The Maha Sarakham salt gives the result in the same range with salt from other locations.



Figure 3.21 Some post-tested specimens subjected to the triaxial stresses. Specimen on the left shows the multi-shear failure at confining pressure of 15.2 MPa. Specimen on the right shows single shear failure at confining pressure of 12.4 MPa.

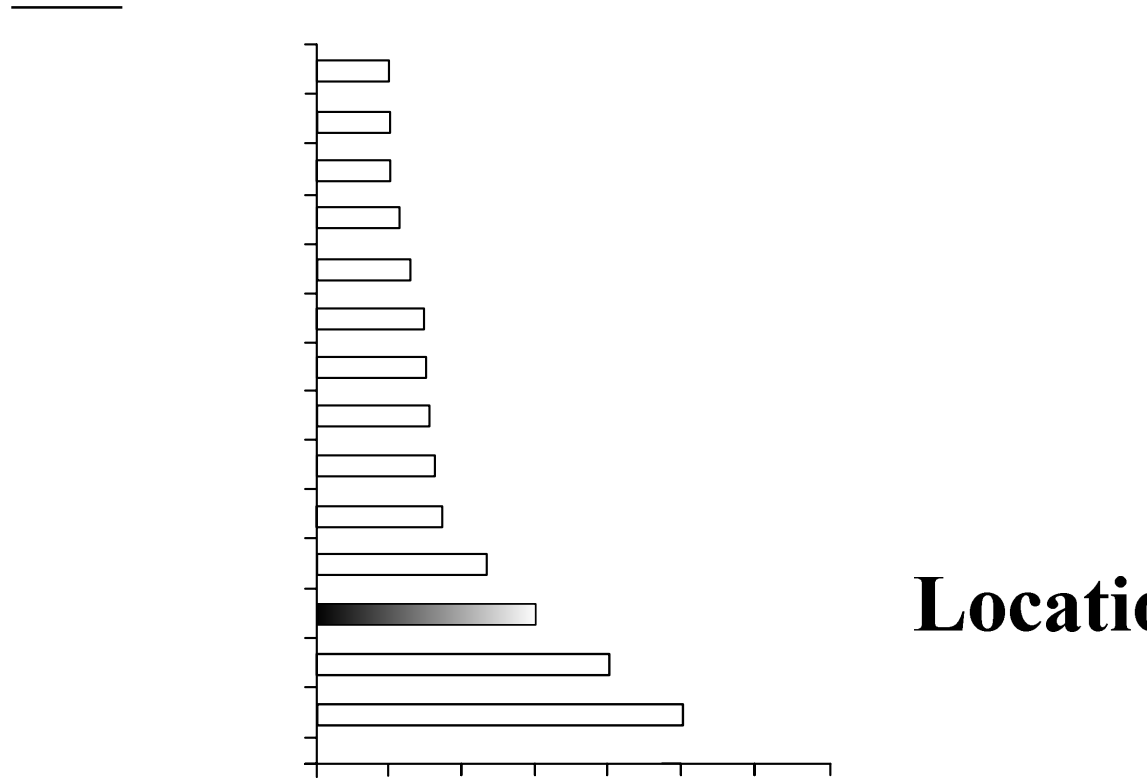


Figure 3.22 Comparison of the cohesion from the triaxial compressive strength tests

obtained here (shaded bar) with the results from various sources (¹

Hansen et al., 1984; ²Lux and Rokahr, 1984; and ³Wetchasat, 2002).

S.E. New Me

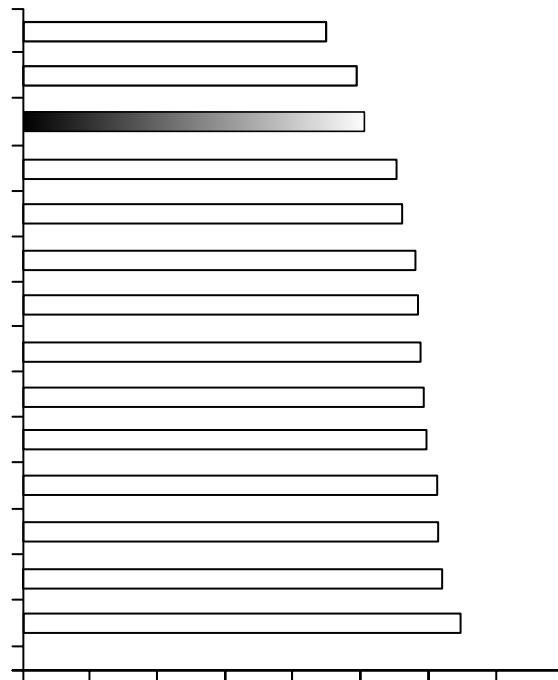


Figure 3.23 Comparison of the internal friction angles obtained here (shaded bar) with the results from various sources (¹ Hansen et al., 1984; ² Lux and Rokahr, 1984; and ³ Wetchasat, 2002)

Loc

Ud

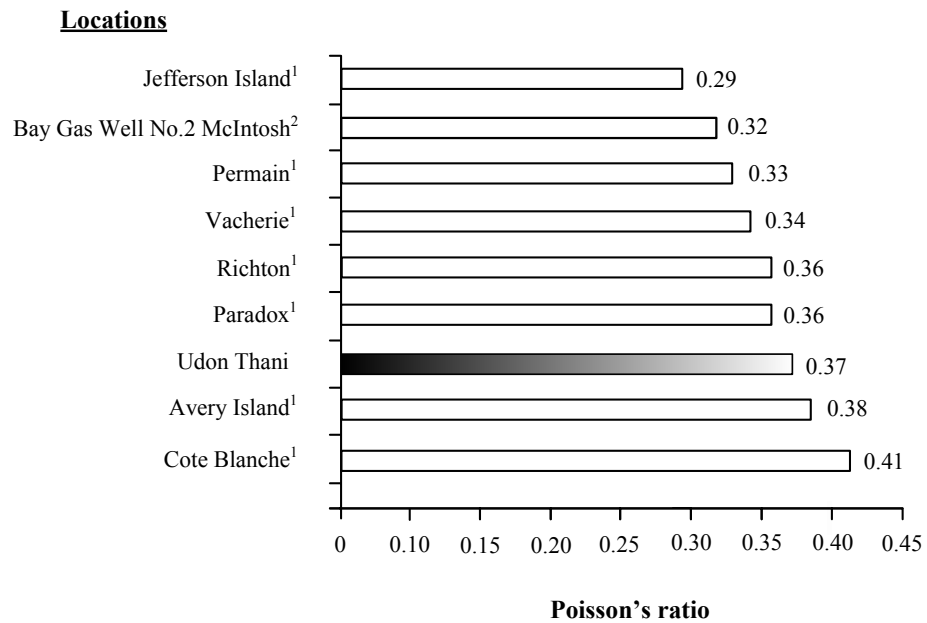


Figure 3.24 Comparison of the Poisson's ratio obtained from the triaxial compressive strength tests performed here (shaded bar) with the results from various sources (¹ Hansen et al., 1984; and ² DeVries et al, 2002)

3.4 Triaxial Creep Tests

The objectives of the triaxial creep tests are to determine time dependent behavior and to compare the creep deformation of salt specimens obtained from two different stress paths (Figures 3.25) under triaxial stress state. This test series consist of two methods: the conventional triaxial creep test (CTC) and the radially unloaded triaxial creep test (RUTC).

3.4.1 Conventional Triaxial Creep Tests (CTC)

The conventional triaxial creep test is performed here to investigate the time dependent behavior of salt. Its main purposes are to monitor the axial strain of the salt specimens under constant triaxial stress conditions and to obtain the results to compare with those from the radially unloaded triaxial creep test. The deformation characteristics and the mechanical properties are determined. These include elastic, viscoelastic and viscoplastic behaviors. The specimens are collected from the depths between 250 and 445 meters. The conventional test is performed in accordance with the ASTM standard (ASTM D4406-93) and the suggested methods by Wawersik and Preece (1981). Four salt specimens have been tested. They have a nominal diameter of 54 millimeters with a length-to-diameter ratio of 2.0. Each specimen is subjected to two loading stages. For the first stage, the octahedral shear stresses are 2.0, 3.5, 4.1 and 5.1 MPa. For the second stage, the octahedral shear stresses are 8.7, 9.6, and 10.6 MPa.

3.4.1.1 Test Procedures

The test is performed by quasi-static loading with two loading stages. For the first stage, the axial stress and confining pressure are simultaneously applied and maintained constant for five days. In the second stage, the axial stress is

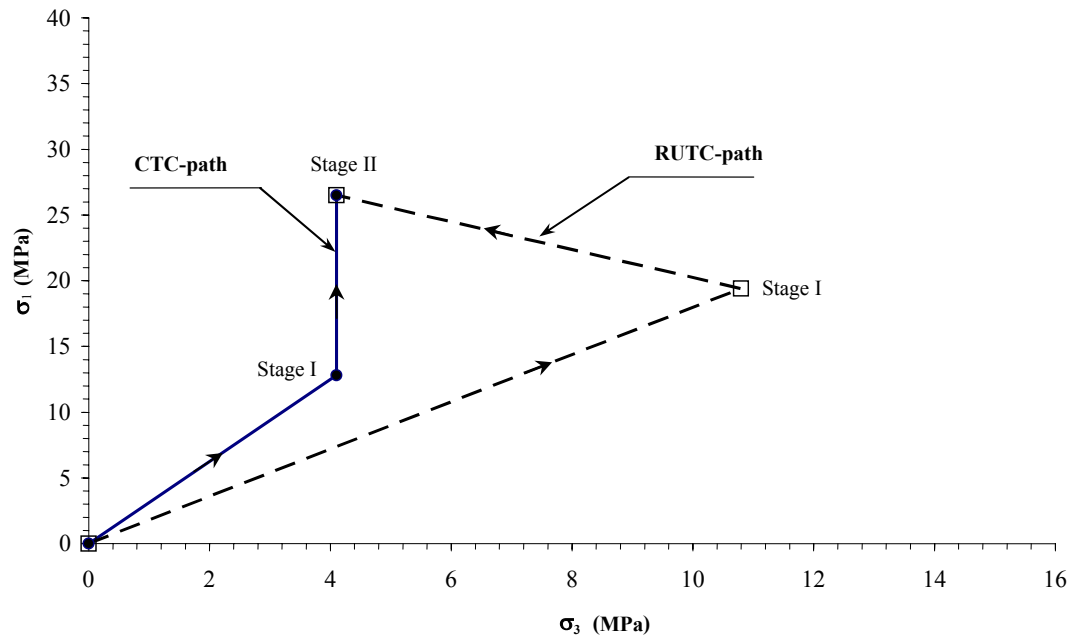


Figure 3.25 Comparison of stress paths between the conventional method (CTC) and the radially unloaded method (RUTC) in major-minor principal stresses diagram.

increased while the confining pressure remains unchanged for 10 days. Table 3.4 shows the test matrix of all test series. The axial load is applied and maintained by a lever arm consolidometer. The load beam gives a load ratio of 20:1. The specimen is enclosed in a rubber jacket inside the Hoek cell and pressurized by hydraulic oil. The confining pressure is applied by hand pump (the maximum capacity is 69 MPa). The confining pressure is maintained by adjusting the controlled valves. The axial deformations are monitored by two digital gauges with a precision of 0.001 millimeter. The laboratory arrangement is given in Figure 3.26. The tests are performed at the room temperature. Post-tested of specimen are observed. Photographs are taken.

3.4.1.2 Test Results and Discussions

The creep test results under conventional triaxial compression loading are presented in Figures 3.27 to 3.30. They show the creep behavior of the salt specimens under different octahedral shear stresses in the creep strain-time diagram for 15 days. The octahedral shear stress (τ_{oct}) and strain (γ_{oct}) can be calculated by equations,

$$\tau_{\text{oct}} = 1/3 [(\sigma_1 - \sigma_2)^2 + (\sigma_2 - \sigma_3)^2 + (\sigma_3 - \sigma_1)^2]^{1/2} \quad (3.18)$$

$$\gamma_{\text{oct}} = 1/3 [(\varepsilon_1 - \varepsilon_2)^2 + (\varepsilon_2 - \varepsilon_3)^2 + (\varepsilon_3 - \varepsilon_1)^2]^{1/2} \quad (3.19)$$

where σ_1 is the maximum principal stress (axial stress), σ_2 is the intermediate principal stress (confining pressure), σ_3 is the minimum principal stress (confining pressure), ε_1 is the major principal strain, ε_2 is the intermediate principal strain, and ε_3 is the minor principal strain.

Table 3.4 Test matrix for the conventional triaxial creep testing.

Specimen No.	Test Stage	Duration (Days)	Axial Stress σ_1 (MPa)	Confining Pressure σ_3 (MPa)	Octahedral Shear Stress τ_{oct} (MPa)	Mean Stresses σ_m (MPa)
BD99-1-CTC2e	1	5	10.2	2.8	3.5	5.3
	2	5	21.3	2.8	8.7	8.9
BD99-1-CTC3e	1	5	17.8	6.9	5.1	10.5
	2	10	27.3	6.9	9.6	13.7
BD99-1-CTC4e	1	5	12.8	4.1	4.1	7.0
	2	10	26.5	4.1	10.6	11.6
BD99-1-CTC5e	1	5	11.2	6.9	2.0	8.3
	2	10	27.3	6.9	9.6	13.7

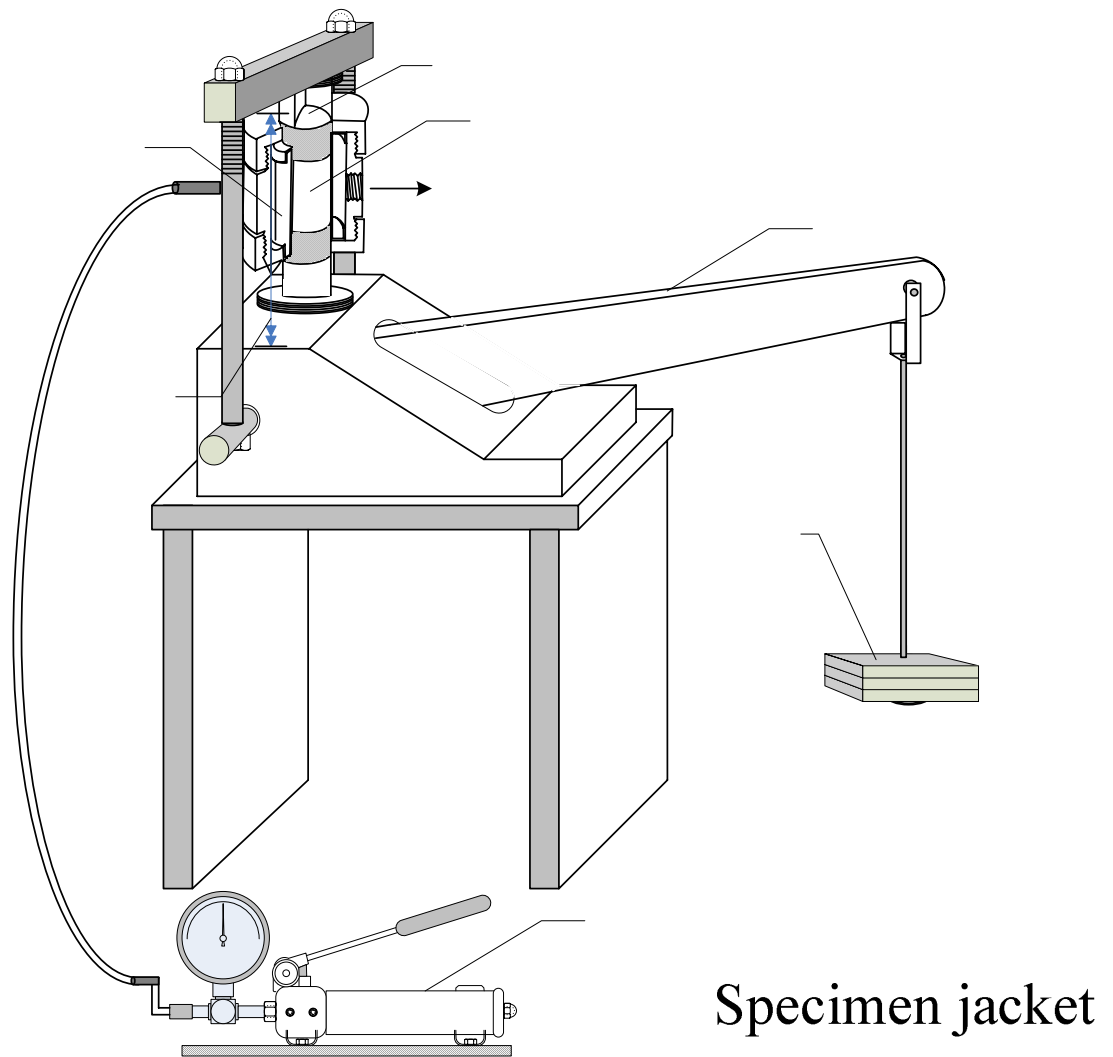


Figure 3.26 Schematic diagram for triaxial creep testing. The axial load is applied and maintained by dead weight through a level arm.

Axis of
deformation
measurement

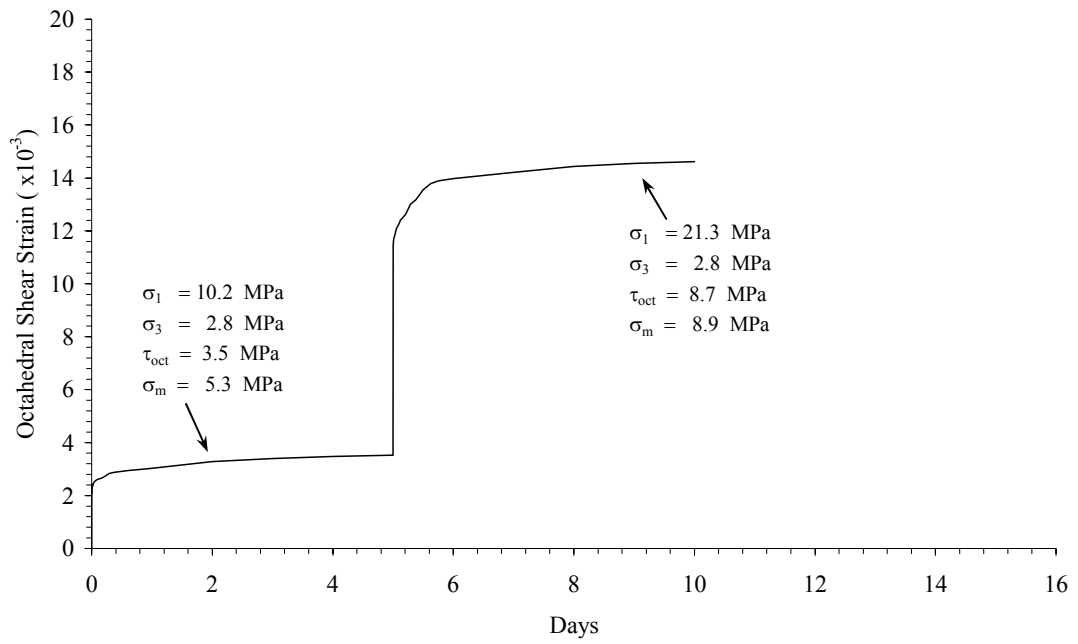


Figure 3.27 Result of conventional triaxial creep test for specimen number BD99-1-CTC2e.

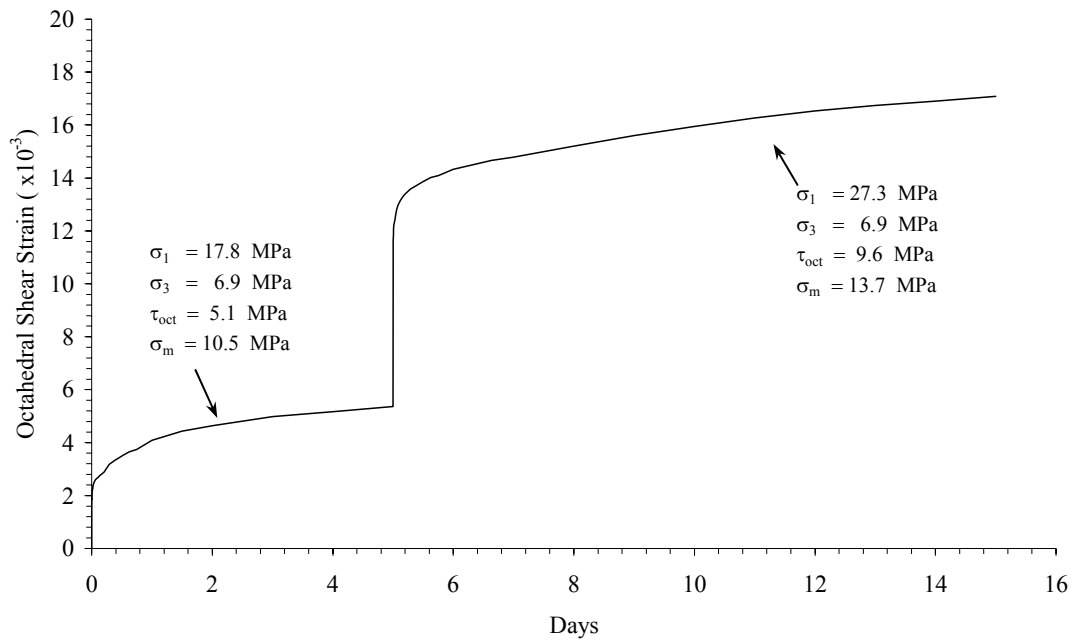


Figure 3.28 Result of conventional triaxial creep test for specimen number BD99-1-CTC3e.

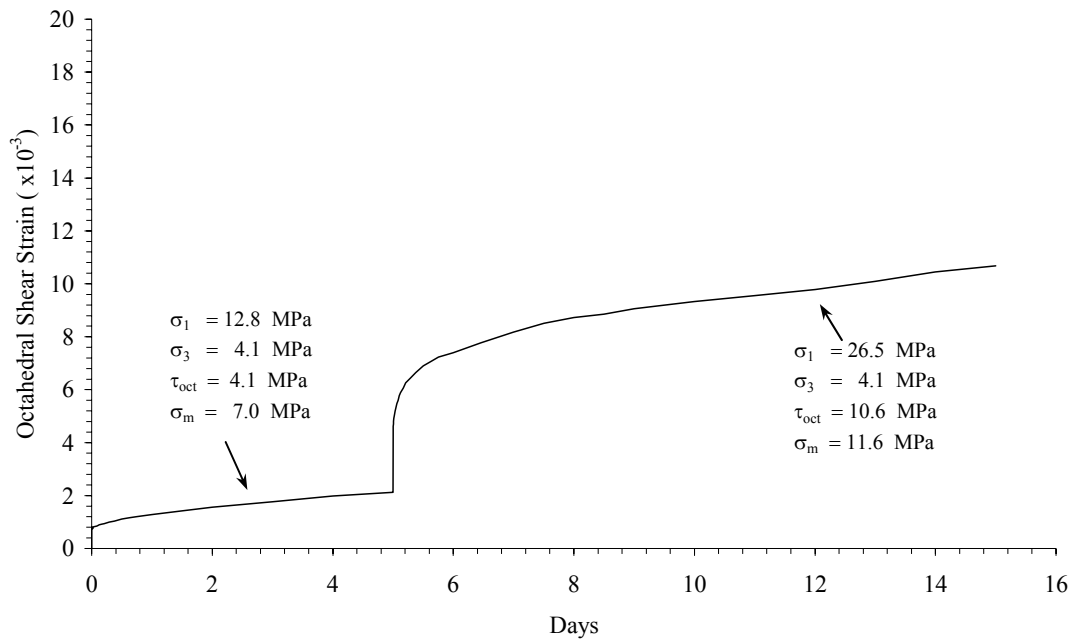


Figure 3.29 Result of conventional triaxial creep test for specimen number BD99-1-CTC4e.

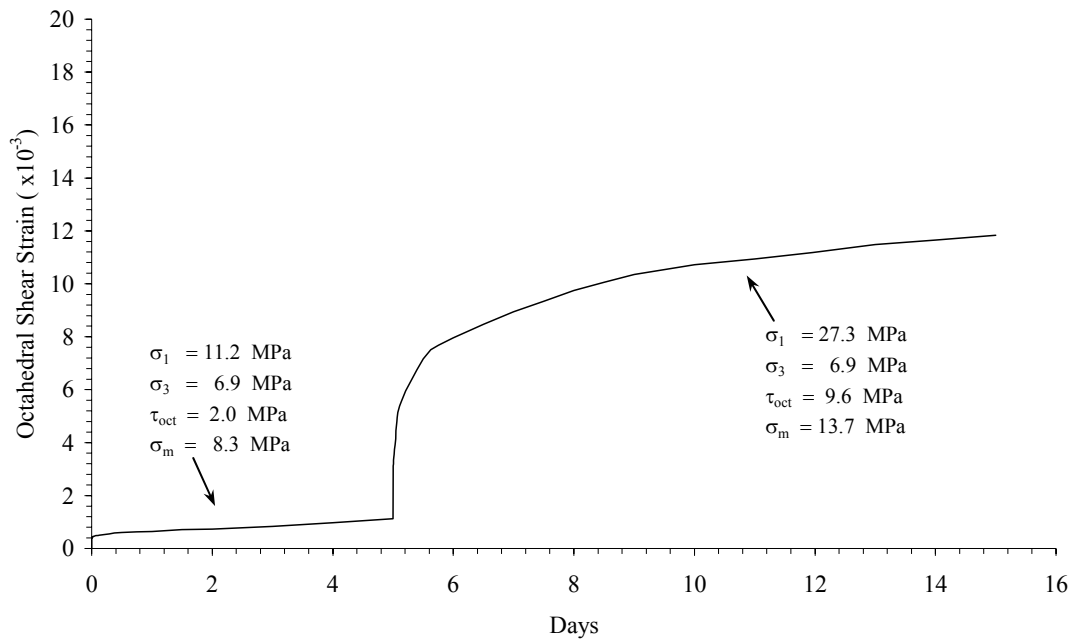


Figure 3.30 Result of conventional triaxial creep test for specimen number BD99-1-CTC5e.

Table 3.5 summarizes the test results. The instantaneous strains from both stages are presented in Table 3.6. Changing of the creep strains from the first stage to the second stage is clearly observed. Their quantitative differences are also shown.

The post-tested specimens show different modes of deformation depending on the magnitude of the octahedral shear stresses. A small deformation shows when the specimens subjected to low octahedral shear stress (8.7 MPa). For the specimens subjected to high octahedral shear stresses (9.6 and 10.6 MPa), they show more radial expansion. The tensile cracks are induced along inter-crystalline boundaries. The micro-cracks are extended parallel to the specimen axis. The difference between the original diameter and the final diameter of the salt specimens are between 3 and 5%. Figure 3.31 gives a photograph of some post-tested specimens. The strain-time curves are illustrated in Figures 3.27 to 3.30. The instantaneous strains tend to increase as the octahedral shear stresses increase. The octahedral shear strain rate in the first stage is lower than that in the second stage. The creep deformation is strongly dependent on the increment of the octahedral shear stresses. The deformation characteristics of the specimens subjected to the quasi-static loading presented here are similar to the tested data from many investigators (e.g., Wawersik and Hannum, 1980; Yin, 1998; and Devries et al., 2002). Additional discussions of the test results as compared to the RUTC test results are presented in the Chapter VI.

3.4.2 Radially Unloaded Triaxial Creep Tests (RUTC)

The objective of the radially unloaded triaxial creep test is to assess the effect of the different stress path by comparing the results with those from the conventional triaxial creep test. The comparison will be made in terms of the instantaneous and creep strains.

Table 3.5 Summary of the results for the conventional triaxial creep testing.

Specimen No.	Average Diameter D_s (mm)	Average Length L (mm)	Depth (m)	Test Stage	Total Octahedral Shear Strain (1×10⁻³)	Octahedral Shear Strain Rate (1×10⁻⁹/second)
BD99-1-CTC2e	53.57	106.94	248.90 (MS)	1	3.50	0.91
				2	14.60	1.59
BD99-1-CTC3e	55.45	110.00	250.10 (MS)	1	5.40	2.25
				2	17.18	2.84
BD99-1-CTC4e	55.50	110.17	210.25 (MS)	1	2.12	2.04
				2	10.70	3.24
BD99-1-CTC5e	54.03	107.94	444.76 (LS)	1	1.12	1.50
				2	11.83	2.58

Note: MS = Middle Salt

LS = Lower Salt

Table 3.6 Summary of the instantaneous strains calculated from the results of CTC test.

Specimen No.	Test Stage	Octahedral Shear Stress τ_{oct} (MPa)	Different Octahedral Shear Stress $\tau_{oct}^2 - \tau_{oct}^1$ (MPa)	Instantaneous Strain (1×10^{-3})
BD99-1-CTC2e	1	3.5	5.2	2.02
	2	8.7		11.57
BD99-1-CTC3e	1	5.1	4.5	1.70
	2	9.6		11.87
BD99-1-CTC4e	1	4.1	6.5	0.73
	2	10.6		4.71
BD99-1-CTC5e	1	2.0	7.6	0.38
	2	9.6		3.19

Note: τ_{oct}^1 = the octahedral shear stress in the first stage

τ_{oct}^2 = the octahedral shear stress in the second stage



Figure 3.31 Some post-tested specimens subjected to the conventional triaxial stress path. Both specimens show the tensile crack induced along inter-crystalline boundaries. Specimens on the left and right are subjected to the octahedral shear stresses in the second stage of 9.6 MPa and 10.6 MPa, respectively.

3.4.2.1 Experimental Procedures

To study the effect of different stress paths, the loading directions and sequences for RUTC are different from the conventional triaxial creep test. The test duration and the test parameters for each stage are in the same. For the first stage, the axial stress and confining pressure are simultaneously applied and maintained constant for five days. After that, the axial stress is increased while the confining pressure is decreased. The salt specimens are subjected to this stage for 10 days. Table 3.7 shows the test matrix for all test series. All test equipments and accessories are the same with that of the conventional test. The test parameters are also controlled under the same conditions. Post-tested of specimens are observed and photographed.

3.4.2.2 Experimental Results and Discussions

Figures 3.32 to 3.35 present the results of the radially unloaded triaxial creep test. The curves illustrate the deformation characteristics at different octahedral shear stresses in the creep strain-time diagram for 15 days. The creep strain can be calculated by equation (3.19).

Table 3.8 summarizes the test results. The instantaneous strains for both stages are presented in Table 3.9. Difference of the creep strains from the first stage to the second stage is significant.

The post-tested specimens show a small creep deformation. Some specimens show the micro-cracks extending along crystalline boundaries. The different between the original diameters and the final diameter of the salt specimens are between 1.5 and 4.5%. Figure 3.36 gives a photograph of some post-tested specimens. For the first stage, the creep deformations tend to increase as the octahedral shear stresses increase. Similar to the conventional triaxial stress path, the

Table 3.7 Test matrix for the radially unloaded triaxial creep testing.

Specimen No.	Test Stage	Duration (Days)	Axial Stress σ_1 (MPa)	Confining Pressure σ_3 (MPa)	Octahedral Shear Stress τ_{oct} (MPa)	Mean Stress σ_m (MPa)
BD99-1-RUTC2e	1	5	14.9	7.5	3.5	10.0
	2	5	21.3	2.8	8.7	8.9
BD99-1-RUTC3e	1	5	21.9	11.0	5.1	14.6
	2	10	27.3	6.9	9.6	13.7
BD99-1-RUTC4e	1	5	19.4	10.8	4.1	13.7
	2	10	26.5	4.1	10.6	11.6
BD99-1-RUTC5e	1	5	16.1	11.8	2.0	13.2
	2	10	27.3	6.9	9.6	13.7

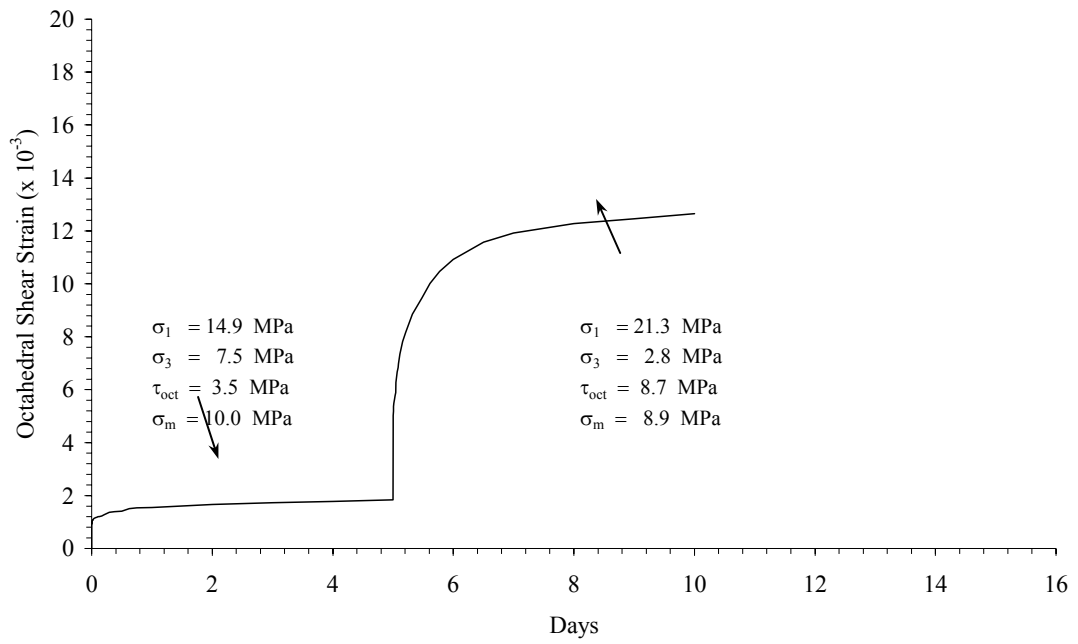


Figure 3.32 Result of radially unloaded triaxial creep test for specimen number BD99-1-RUTC2e.

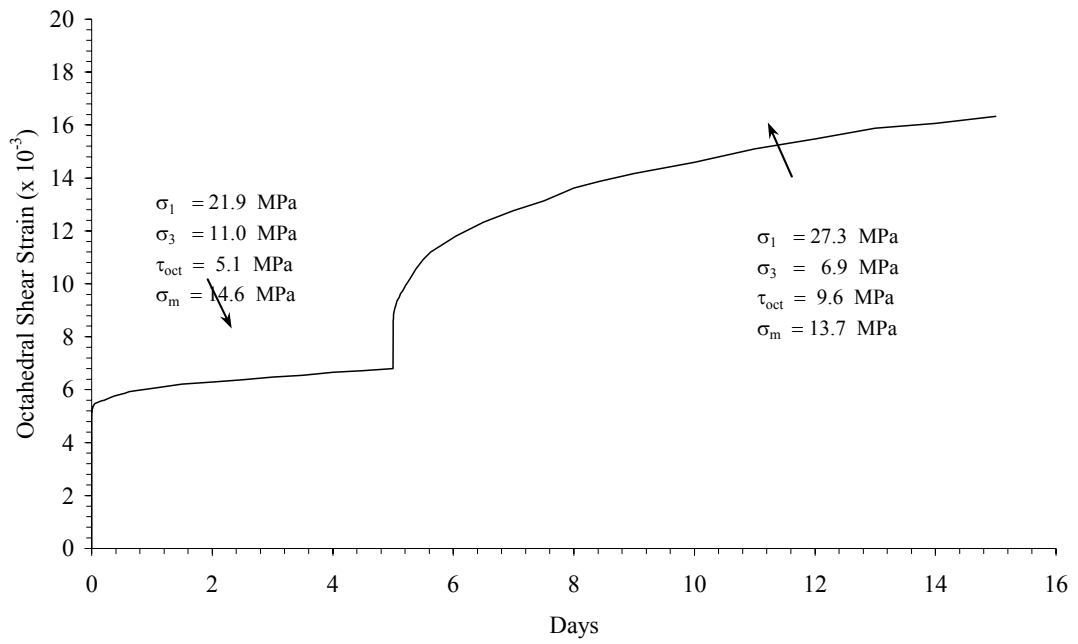


Figure 3.33 Result of radially unloaded triaxial creep test for specimen number BD99-1-RUTC3e.

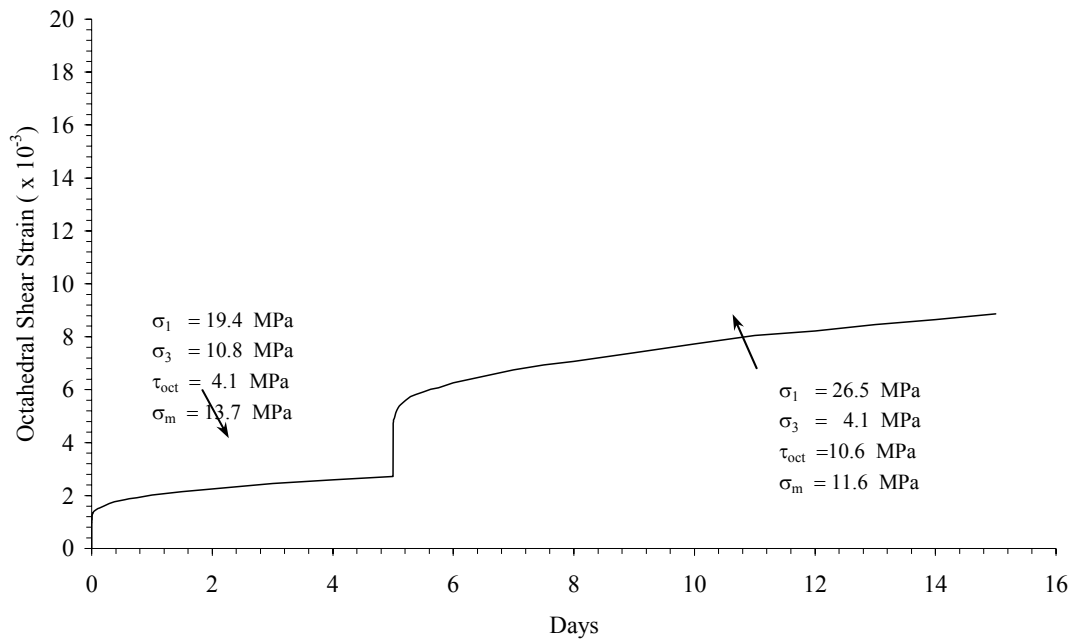


Figure 3.34 Result of radially unloaded triaxial creep test for specimen number BD99-1-RUTC4e.

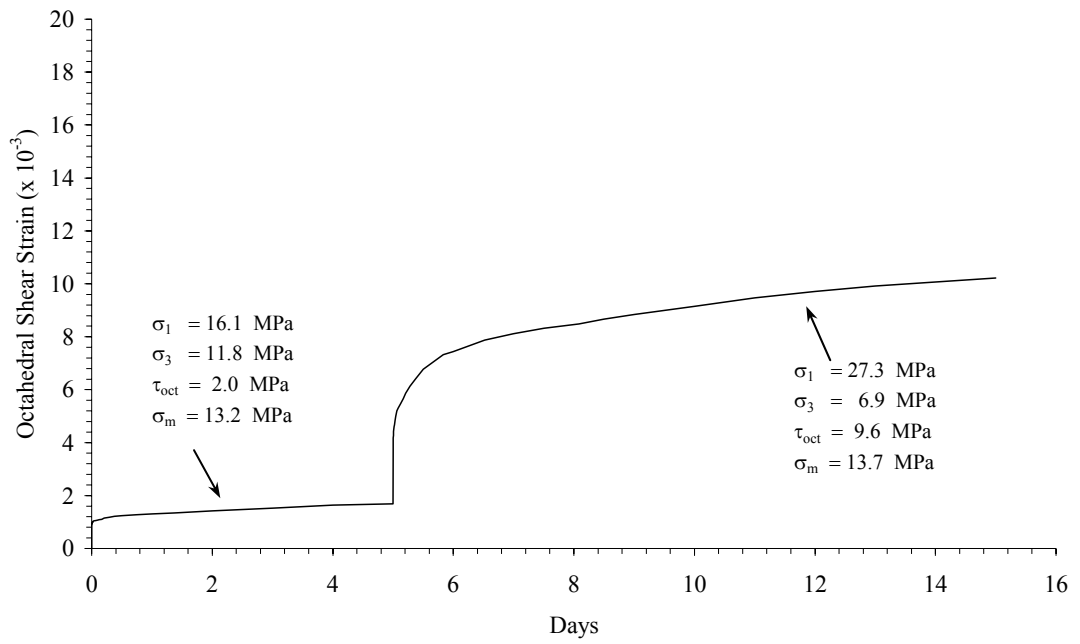


Figure 3.35 Result of radially unloaded triaxial creep test for specimen number BD99-1-RUTC5e.

Table 3.8 Summary of test results for the radially unloaded triaxial creep testing.

Specimen No.	Average Diameter D_s (mm)	Average Length L (mm)	Depth (m)	Test Stage	Total Octahedral Shear Strain (1×10^{-3})	Octahedral Shear Strain Rate ($1 \times 10^{-9}/S$)
BD99-1-RUTC2e	53.54	107.12	251.03 (MS)	1	1.80	0.68
				2	12.65	2.17 ⁹
BD99-1-RUTC3e	55.52	110.02	251.75 (MS)	1	6.79	1.95
				2	16.32	5.07
BD99-1-RUTC4e	55.50	111.00	210.40 (MS)	1	2.72	1.80
				2	8.85	2.61
BD99-1-RUTC5e	53.99	107.85	426.64 (LS)	1	1.69	1.09
				2	10.22	2.47

Note: MS = Middle Salt

LS = Lower Salt

Table 3.9 Summary of the instantaneous strains calculated from the results of RUTC tests.

Specimens No.	Test Stage	Octahedral Shear Stress τ_{oct} (MPa)	Different Octahedral Shear Stress $\tau_{oct}^1 - \tau_{oct}^2$ (MPa)	Instantaneous Strain (1×10^{-3})
BD99-1-RUTC2e	1	3.5	5.2	0.93
	2	8.7		5.19
BD99-1-RUTC3e	1	5.1	4.5	5.03
	2	9.6		8.70
BD99-1-RUTC4e	1	4.1	6.5	0.97
	2	10.6		4.80
BD99-1-RUTC5e	1	2.0	7.6	0.89
	2	9.6		4.27

Note: τ_{oct}^1 = the octahedral shear stress in the first stage.

τ_{oct}^2 = the octahedral shear stress in the second stage.



Figure 3.36 Some post-tested specimens subjected to the radially unloaded triaxial stress path. Both specimens show the tensile crack induced along inter-crystalline boundaries but specimen on the right show more expansion. Specimens on the left and right are subjected to the octahedral shear stresses in the second stage of 9.6 MPa and 10.6 MPa, respectively.

deformation for the first stage depends on the octahedral shear stress. The test results obtained from here agree reasonably well with those from Allemandou and Dusseault (1993). Comparison between CTC and RUTC results are given in Chapter VI.

CHAPTER IV

CALIBRATION OF SALT PROPERTIES

4.1 Introduction

The purpose of this chapter is to describe the determination of the salt property parameters in the constitutive equation. The data used in the calibration are obtained from two different loading paths of the triaxial creep tests. Nonlinear curve fitting technique and calculation of creep equations are used to determine the parameter values. These parameters include the elastic, the viscoelastic and the viscoplastic parameters.

4.2 Calibration of Salt Property Parameters

The objective of the calibration is to determine the property parameters of the salt specimens subjected to the different loading paths. A viscoelastic-viscoplastic model in GEO program as described in Chapter II is used here to describe the salt behavior. A single finite element mesh is constructed to simulate the geometry, boundary and loading conditions of the triaxial creep test specimen. The mesh is designed for axis-symmetric analysis by using the salt specimen axis as a centerline. Figure 4.1 shows the representative top-right quarter of the salt specimen to be modeled. The model dimension is 27 mm in diameter and 54 mm in height. The left boundary of the mesh represents the centerline of the specimen. It is fixed in horizontal direction. The bottom boundary of the mesh does not allow displacement

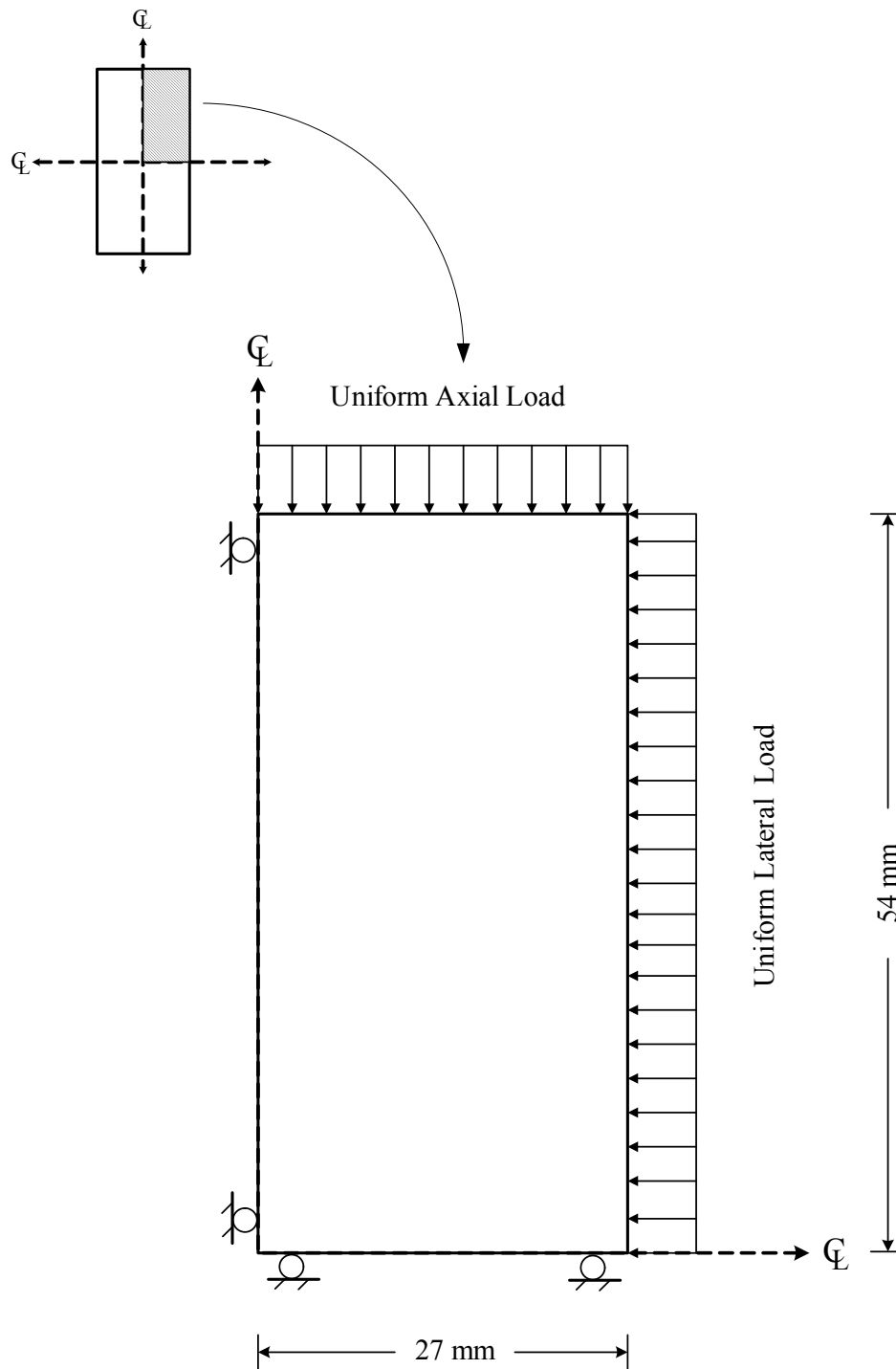


Figure 4.1 Model of salt specimen by using a single element used in the calibration of property parameters.

in vertical direction. To simulate the triaxial stress-strain, the top and the right are subjected to axial and lateral loads. Back analysis techniques are used to determine the parameter values in the GEO model. The initial parameters that included in the GEO model, but are not studied here are K^A , K^B , D_2 , P and γ_c . Their values are given in Table 4.1. The calibration is performed by adjusting the coefficients in the model until the calculated results agree as closely as possible with each set of test data in terms of the strain-time curves. After numerous trials, a set of numerical values will provide a relatively good fit to the test results. The parameters calibrated here include the shear modulus (G_1), the ultimate bulk modulus (K_1), the retarded shear modulus (G_2), the retarded bulk modulus (K_2), the elastoviscosity (η_2) and the plastoviscosity (η_4).

4.2.1 Determination of Elastic Parameters

The basic parameters in the elastic state include the Poisson's ratio (ν), the modulus of elasticity (E_1), the shear modulus (G_1) and the ultimate bulk modulus (K_1). The average value of the Poisson's ratio is 0.37. It is obtained from the triaxial compressive strength tests. The average modulus of the elasticity obtained from the same salt member is 25 GPa (Fuenkajorn and Jandakaew, 2003). This value is assumed to be the same with the all salt specimens tested here. The salt specimens are assumed to be an isotropic linearly elastic solid, and hence relation of the elastic parameters can be expressed as (Jaeger and Cook, 1979),

$$G_1 = E_1/2(1+\nu), \quad (4.13)$$

$$K_1 = 2G_1(1+\nu)/3(1-2\nu). \quad (4.14)$$

Table 4.1 The initial salt property parameters obtained from GEO database (Serata and Fuenkajorn, 1993).

Property	Symbol	Unit	Values used in this study
Unconfined Octahedral Shear Strength	K^A	MPa	0.38
Ultimate Octahedral Shear Strength	K^B	MPa	3.80
Hydrostatic Elastoviscosity	D_2	GPa·day	48
Critical strain at failure	γ_c	10^{-3}	0.001
Plastic transition pressure	P	MPa	41.4

Tables 4.2 and 4.3 give the values of G_1 and K_1 obtained from the triaxial tests under both loading paths. Their average values are 9.1 GPa and 31.9 GPa for G_1 and K_1 , respectively.

4.2.2 Determination of Viscoelastic Parameters

The viscoelastic state is defined as the state in which the octahedral shear stress (τ_o) is less than the octahedral shear strength (K_o) (Serata and Fuenkajorn, 1993). Three parameters in this state have been determined, including the retarded shear modulus (G_2), the elastoviscosity (η_2), and the retarded bulk modulus (K_2). Since the viscoelastic behavior of the salt specimens can be best shown in short-term period. The strain-time curve from the transient creep phase is used in the calibration. The curve fitting is applied for determining the value of G_2 , and η_2 . Their values are adjusted until the slope and the curvature from the computer simulation match the actual strain-time curves. The K_2 can be calculated from relation (Jaeger and Cook, 1979),

$$K_2 = \tau_{oct} / \gamma_{oct}^i \quad (4.15)$$

where τ_{oct} is the octahedral shear stress and γ_{oct}^i is the viscoelastic octahedral shear strain. Tables 4.2 and 4.3 summarize the viscoelastic parameters of the salt specimens obtained from the computer modeling for the first loading stage.

4.2.3 Determination of Viscoplastic Parameter

The viscoplastic state is defined as the state in which τ_o is equal to or greater than K_o (Serata and Fuenkajorn, 1993). The key parameter in this state is the plastoviscosity (η_4). The value of η_4 can be calculated by (Goodman, 1989),

$$\eta_4 = \tau_{oct} / 3\gamma_{oct}^s \quad (4.16)$$

Table 4.2 Salt property parameters calculated from the results obtained from the CTC tests using the finite element code GEO and the creep equations (Jaeger and Cook, 1979 and Goodman, 1989).

Phase	Property	Symbol	Unit	Stage	BD99-1-CTC				Average
					2e	3e	4e	5e	
Elastic	Poisson's ratio	ν	-	1-2	0.37				0.37
	Elastic modulus	E_1	GPa	1-2	25.0				25.0
	Shear modulus	G_1	GPa	1-2	9.1				9.1
	Ultimate bulk modulus	K_1	GPa	1-2	32.0				32.0
Viscoelastic	Retarded shear modulus	G_2	GPa	1	0.7	0.6	0.7	3.1	1.3 ± 1.22
				2	0.4	0.4	0.5	0.4	0.4 ± 0.05
	Retarded bulk modulus	K_2	GPa	1	0.5	0.5	0.6	0.3	0.5 ± 0.13
				2	0.4	0.5	0.5	0.7	0.5 ± 0.13
	Elastoviscosity	η_2	GPa·day	1	7.0	7.2	6.9	7.9	7.3 ± 0.45
				2	7.7	7.0	7.1	7.9	7.4 ± 0.44
Viscoplastic	Plastoviscosity	η_4	GPa·day	1	14.8	8.7	7.8	5.1	9.1 ± 4.10
				2	21.1	13.0	12.6	14.4	15.3 ± 3.96

Table 4.3 Salt property parameters calculated from the results obtained from the RUTC tests using the finite element code GEO and the creep equations (Jaeger and Cook, 1979 and Goodman, 1989).

Phase	Property	Symbol	Unit	Stage	BD99-1-RUTC				Average
					2e	3e	4e	5e	
Elastic	Poisson's ratio	ν	-	1-2	0.37				0.37
	Elastic modulus	E_1	GPa	1-2	25.0				25.0
	Shear modulus	G_1	GPa	1-2	9.1				9.1
	Ultimate bulk modulus	K_1	GPa	1-2	32.0				32.0
Viscoelastic	Retarded shear modulus	G_2	GPa	1	1.1	1.5	1.8	4.0	2.1 ± 1.30
				2	0.2	0.4	1.0	0.5	0.5 ± 0.34
	Retarded bulk modulus	K_2	GPa	1	1.4	0.3	0.6	1.2	0.9 ± 0.51
				2	0.6	0.5	0.5	0.5	0.5 ± 0.05
	Elastoviscosity	η_2	GPa-day	1	7.3	7.9	6.9	9.0	7.8 ± 0.91
				2	7.2	7.2	6.9	9.0	7.6 ± 0.96
Viscoplastic	Plastoviscosity	η_4	GPa-day	1	19.8	10.1	8.8	7.1	15.5 ± 5.70
				2	15.5	7.3	15.6	15.0	13.4 ± 4.04

where τ_{oct} is the octahedral shear stress and $\dot{\gamma}_{\text{oct}}^s$ is the octahedral shear strain rate in the steady state phase. Since the viscoplastic behavior of the salt specimens can be best shown under long-term loading, the results from the steady state phase for the triaxial creep tests have been used to calibrate this value. Tables 4.2 and 4.3 show the value of η_4 obtained from the conventional triaxial creep tests and the radially unloaded triaxial creep tests, respectively.

4.3 Discussions

Figures 4.2 and 4.3 compare the calculated results with the actual experimental results from the salt specimens subjected to CTC and RUTC loading sequences, respectively. Good agreements between the two are obtained for both stages. This also suggests that the GEO model can satisfactorily describe the test results from different loading paths for time dependent material. The elastic parameters are obtained from the linear portion of the curve that is not affected by the stress path. The values are mainly governed by the intrinsic property of the salt specimens. The viscoelastic coefficients are affected by the applied octahedral shear stresses. The retarded shear modulus and elastoviscosity tend to be higher when subjected to low octahedral shear stresses. This is not true for the retarded bulk modulus. For the viscoplastic state, the scatter of the data can be seen. The coefficient values of plastoviscosity in the first stage are slightly less than that in the second stage. The parameters obtained from both stress paths are similar. This indicates that the viscoplastic behavior pronounces more under higher octahedral shear stress. Comparisons of the results between the two testing techniques are given in Chapter VI.

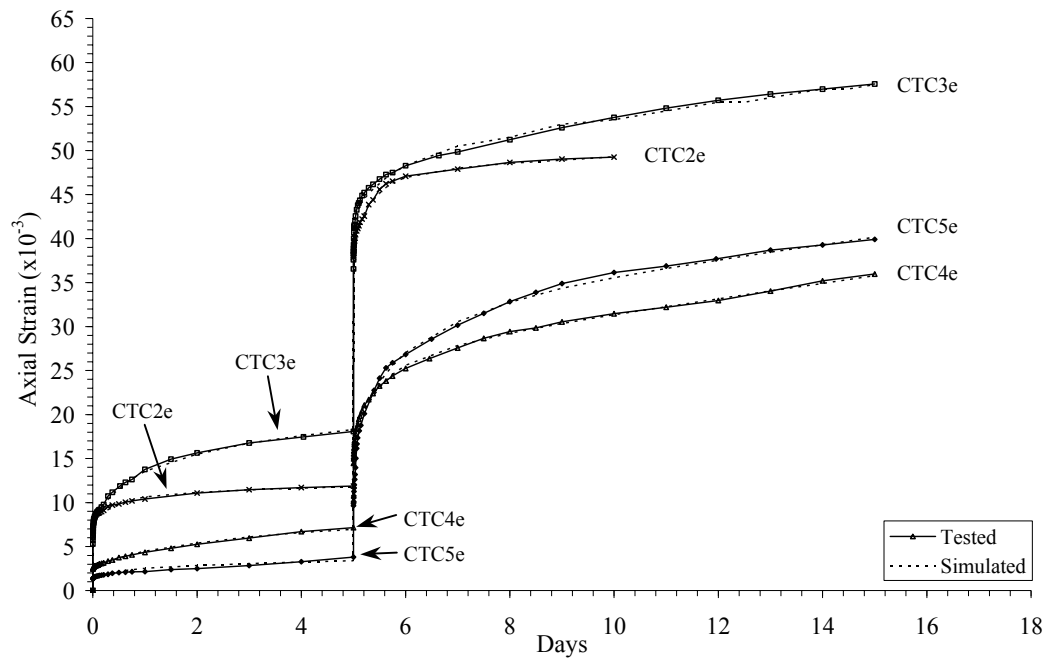


Figure 4.2 Comparison of the strain-time curves between GEO simulation (dot line) and the actual creep test results (solid line) obtained from the conventional triaxial tests.

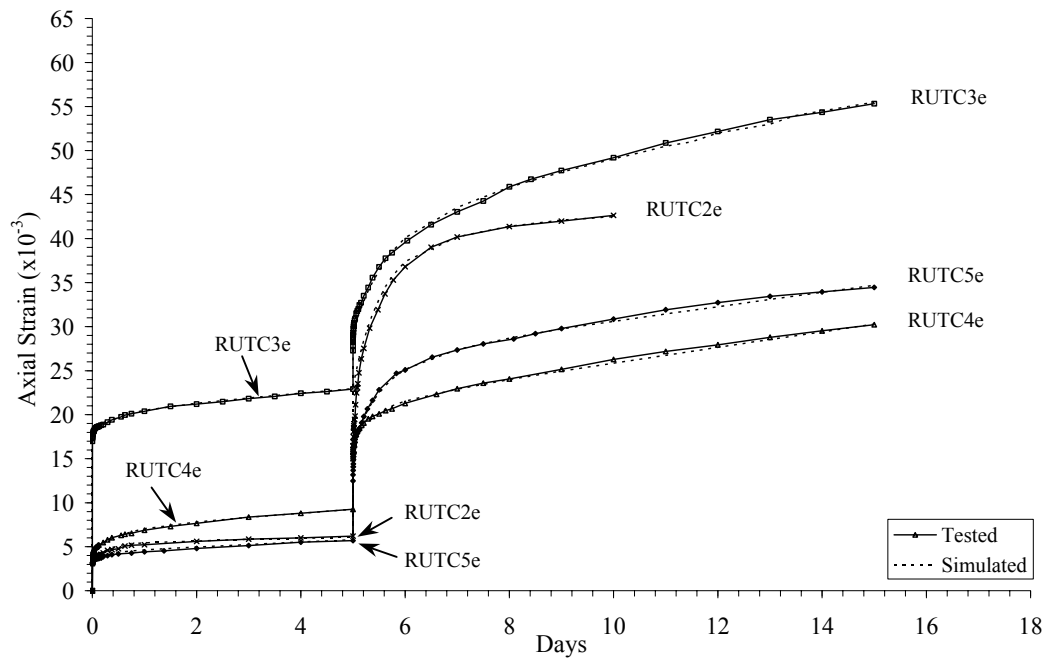


Figure 4.3 Comparison of the strain-time curves between GEO simulation (dot line) and the actual creep test results (solid line) obtained from the radially unloaded triaxial tests.

CHAPTER V

COMPUTER MODELING

5.1 Introduction

The purpose of the study presented in this chapter is to determine the significance of the difference between the CTC and RUTC tests, in terms of the predictions of salt cavern behavior. An isolated spherical cavern and cylindrical cavern are simulated to determine the time-dependent behavior of the surrounding salt mass. The two cavern shapes represent the typical geometries for solution mining, natural gas storage, and waste disposal. The comparison between the two loading paths puts emphasis on the cavern convergence and ground surface subsidence. The non-linear finite element code GEO (Serata and Fuenkajorn, 1992 and Fuenkajorn and Serata, 1992, 1993, 1994) is used in the simulation.

5.2 Area of Study

The geologic sequence used in the modeling is in the area of Ban Kudjig, Wanon Niwat district, Sakon Nakhon province. The core logged data obtained from this area is from borehole number K055 of the Department of Mineral Resources which has been drilled for the potash exploration project in the northeast of Thailand (Japan International Cooperation Agency, 1981).

Description of the stratigraphic sequences of borehole (K055) is provided by Suwanich and Ratanajanuraks (1982). These sequences can be reclassified here based

on their geomechanics properties into three main groups: 1) sediments and clastic rocks, 2) rock salt, and 3) sandstone/siltstone groups (Figure 5.1). The sediments and clastic rocks include all geological formations between and above the salt formations (e.g., anhydrite, mudstone, clay, claystone, siltstone, conglomerate, terrain sediment, alluvial deposits). The rock salt group represents the Upper Salt, Middle Salt, and Lower Salt members. The sandstone/siltstone group represents all rock formations below the salt formations.

5.3 Model Characteristics

The finite element meshes of the spherical and cylindrical caverns are constructed in two dimensions. The vertical cross-sections cover the ground surface to the sandstone and siltstone layers underlying the Lower Salt. Figure 5.2 shows the mesh constructed for the spherical model. It is designed for axis-symmetric analysis using the cavern axis as a centerline. The model covers a horizontal distance of 400 meters and depth of 1000 meters. The cavern roof and floor are at 585 and 625 meters depth. Its diameter is 40 meters. The mesh comprises 1154 elements and 1226 nodes. The left boundary represents the cavern centerline and is laterally constrained. The right boundary is subjected to lithostatic pressure gradient, which pre-calculated from the rock density. The overburden is included in the analysis in order to provide the gravitational weight on the salt cavern, and to allow an assessment of the ground surface subsidence.

Figure 5.3 shows the cylindrical model. The cavern is 40 meters in diameter and 40 meters high. The model covers a horizontal distance of 400 meters. Cavern roof and floor are at 585 and 625 meters depth. The mesh comprises 1196 elements

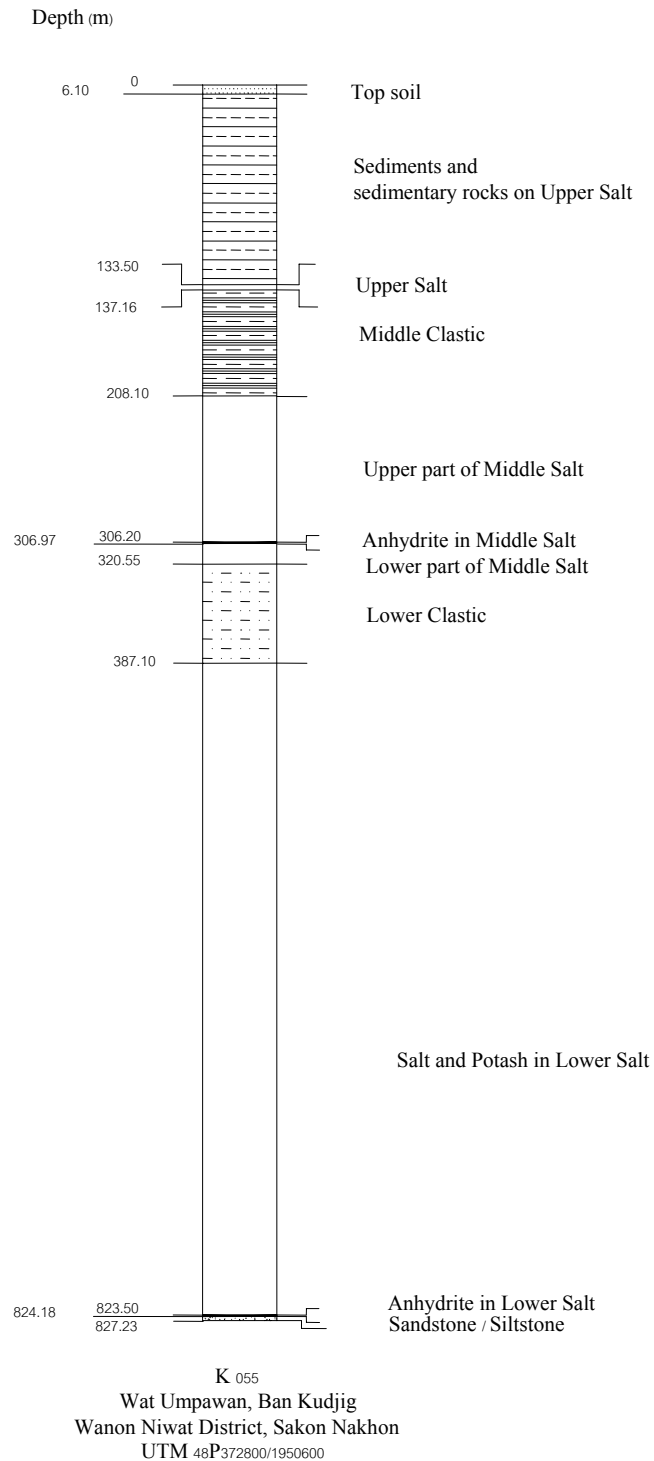


Figure 5.1 Reclassified rock sequences for geomechanics analysis for borehole number K 055 at Wanon Niwat District, Sakon Nakhon.

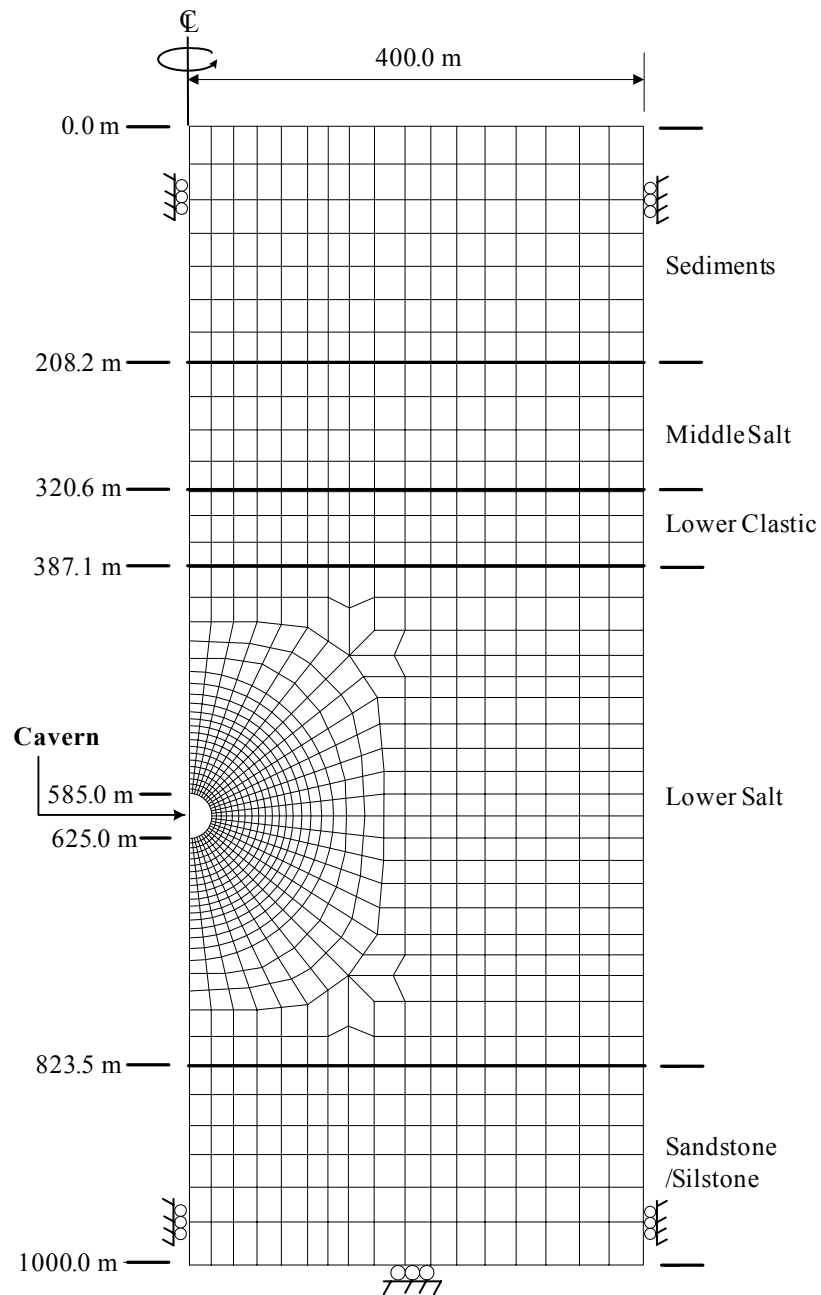


Figure 5.2 Finite element meshes for spherical model showing the spherical cavern and rock stratigraphy at Wanon Niwat District, Sakon Nakhon. The cavern diameter is 40 meters.

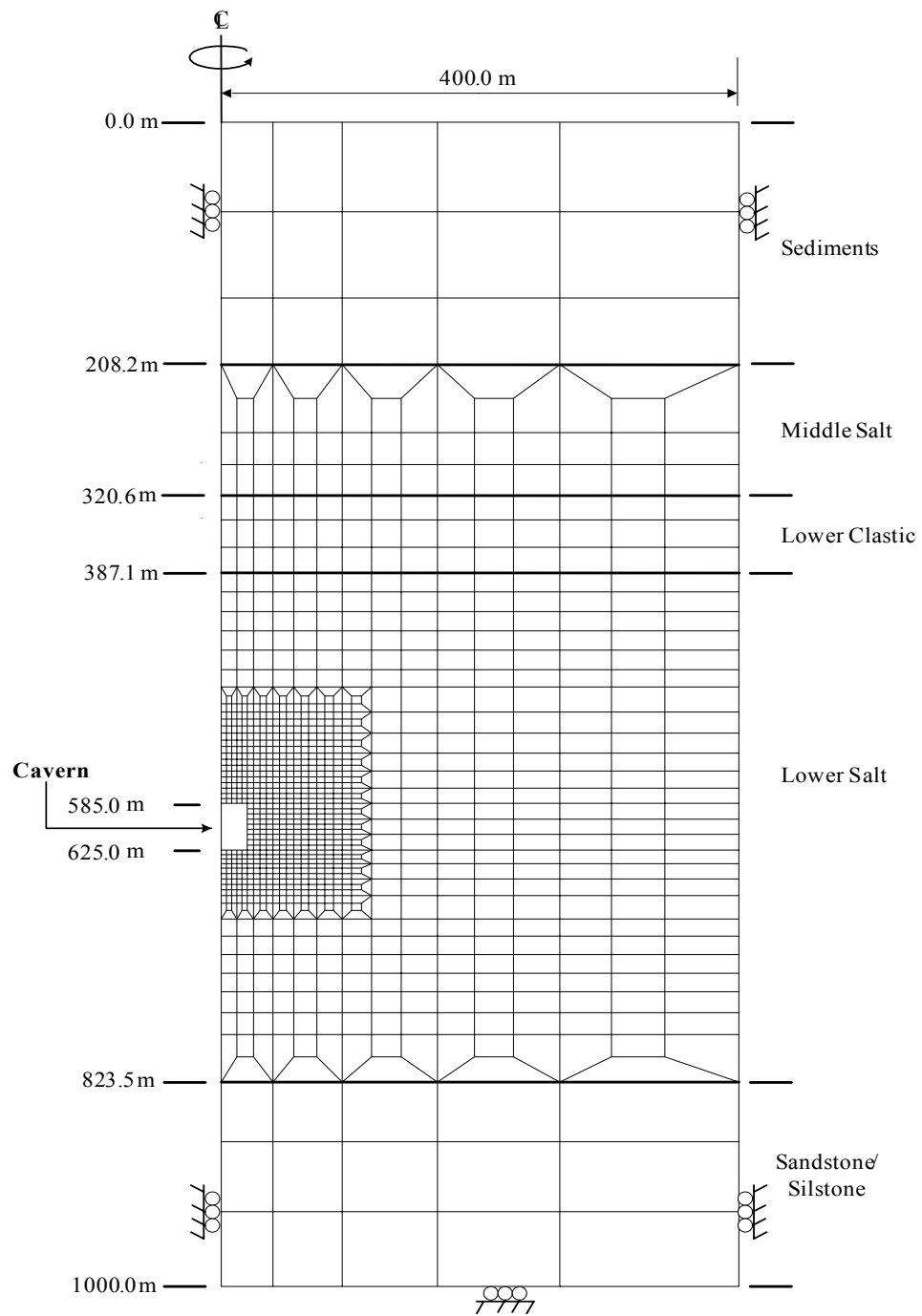


Figure 5.3 Finite element meshes for the cylindrical model showing the cavern and rock stratigraphy at Wanon Niwat District, Sakon Nakhon. The cylindrical cavern is 40 meters high with a diameter of 40 meters.

and 1252 nodes. The boundary conditions of the cylindrical model are similar to those of the spherical model.

Both caverns are simulated under the hydrostatic pressure of brine inside the cavern from the beginning of the cavern development until the next 20 years. The internal pressure is assumed to be uniform at 0.37 MPa. This pressure is calculated by taking the brine density gradient of 0.0061 MPa per meter.

5.4 Rock Properties

The property parameters of rock salt are obtained from the calibration of the test results from CTC and RUTC tests (hereafter called CTC properties, and RUTC properties). The properties of sediments and clastic rocks, and sandstone/siltstone are given by GEO database (Fuenkajorn and Serata, 1993) (Table 5.1). Table 5.2 summarizes the property parameters conservatively selected in the modeling.

5.5 Computer Simulation Results

5.5.1 Spherical Model

Figures 5.4 and 5.5 show the surface subsidence induced by the spherical cavern using CTC properties and RUTC properties, respectively. These curves represent the vertical displacement of ground cavern surface at the cavern center line. The results show that the subsidence rapidly increases at the beginning of cavern development. The subsidence rate decreases with time during the following six months, and tends to be constant through the end of 20 years. The ultimate surface subsidence is 1.14 centimeters and 0.78 centimeter for CTC properties and RUTC properties, respectively.

**Table 5.1 Coefficient values for associated rocks selected from the GEO database
(Fuenkajorn and Serata, 1993).**

Description	Unit	Sediment	Sandy Shale	Sandstone Siltstone	Anhydrite
Shear Modulus	GPa	1.0	6.9	13.8	30.3
Retarded Shear Modulus ($\tau_0 < K_0$)	GPa	0.3	6.9	13.8	27.6
Retarded Shear Modulus ($\tau_0 > K_0$)	GPa	0.3	6.9	13.8	27.6
Elastoviscosity ($\tau_0 < K_0$)	GPa.day	0.3	3.4	3.4	3.4
Elastoviscosity ($\tau_0 > K_0$)	GPa.day	0.3	3.4	3.4	3.4
Plastoviscosity	GPa.day	0.7	13.8	13.8	13.8
Ultimate Bulk Modulus	GPa	1.7	69.0	82.8	69.0
Retarded Bulk Modulus	GPa	1.4	69.0	82.8	82.8
Hydrostatic Elastoviscosity	GPa.day	4.8	69.0	82.8	82.8
Unconfined Octahedral Shear Strength	MPa	0.069	0.690	0.690	1.379
Ultimate Octahedral Shear Strength	MPa	0.690	6.897	6.897	13.793
Yield Surface Coefficient	10^{-3} MPa	0.0007	0.0069	0.0069	0.0103
Critical Strain of Failure		0.001	0.001	0.002	0.002
Density Gradient	MPa/m	-0.0226	-0.0278	-0.0278	-0.0278
Power Coefficient of Plastoviscosity		1.0	1.0	1.0	2.0
Deterioration Coefficient of Shear		2.0	1.0	2.0	0.2
Transition Pressure	MPa	*	*	*	*
Volume Expansion Coefficient		*	*	*	*
Shear Expansion Coefficient		*	*	*	*
Confinement Coefficient		*	*	*	*
Permeability Constant	microdarcy	*	*	*	*
Stress coefficient		*	*	*	*
Minimum Stress Coefficient		*	*	*	*

* Not included in this study

Table 5.2 Summary of salt property parameters for computer models.

Phase	Property	Symbol	Unit	CTC	RUTC
Elastic	Poisson's ratio	ν	-	0.37*	
	Elastic modulus	E_1	GPa	25.0*	
	Shear modulus	G_1	GPa	9.1*	
	Ultimate bulk modulus	K_1	GPa	32.0*	
Viscoelastic	Retarded shear modulus	G_2	GPa	0.9**	1.3**
	Retarded bulk modulus	K_2	GPa	2.8*	2.3*
	Elastoviscosity	η_2	GPa-day	7.4**	7.7**
Viscoplastic	Plastoviscosity	η_4	GPa-day	12.2*	14.5*
Strength	Unconfined octahedral shear	K_o^A	MPa	0.3	
	Ultimate octahedral shear	K_o^B	MPa	6.4	
	Critical shear strain of failure	γ_c	10^{-3}	2.0	

Note: * = Calculated

** = Calibrated

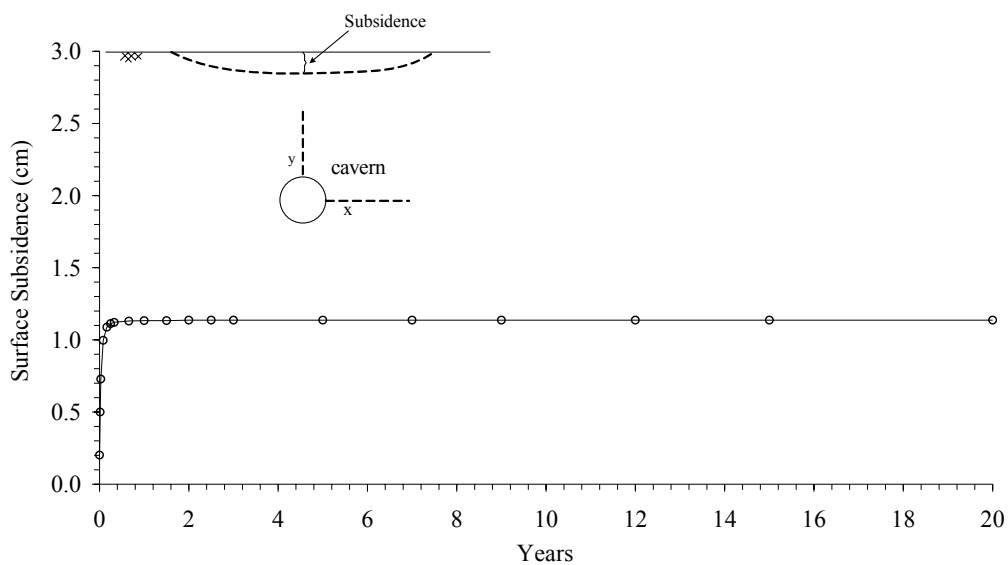


Figure 5.4 Surface subsidence induced by the spherical cavern with the properties calibrated from the results of CTC test.

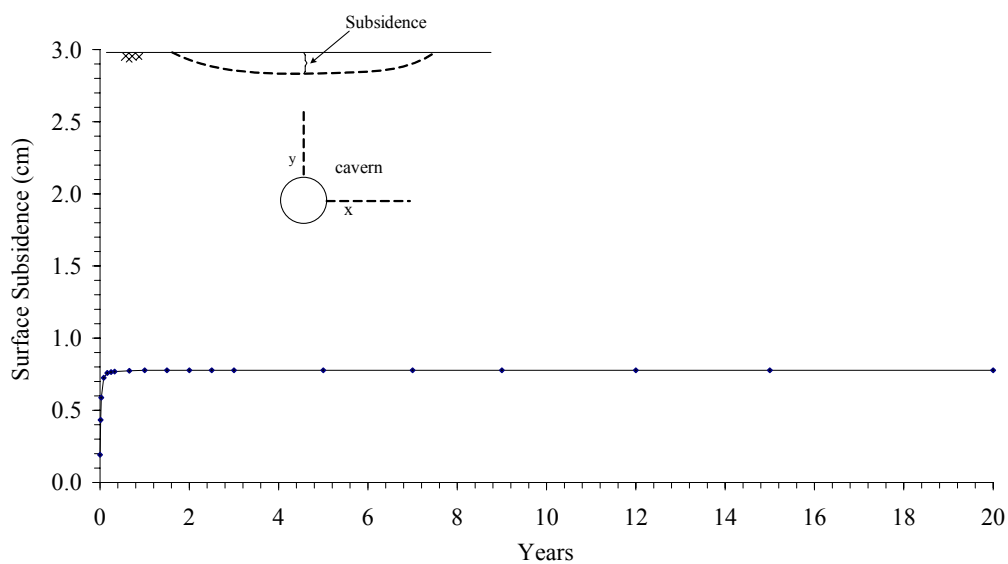


Figure 5.5 Surface subsidence induced by the spherical cavern with the properties calibrated from the results of RUTC test.

The vertical and horizontal closures of the spherical model are shown in Figures 5.6 and 5.7. The vertical closure is about twice higher than that of the horizontal closure for both cases. For the CTC properties, the vertical and horizontal closures reach 17.5 and 8.7 centimeters. For RUTC properties, the vertical closure is 12.9 centimeters and the horizontal closure is 6.5 centimeters after 20 years.

5.5.2 Cylindrical Model

Figures 5.8 and 5.9 show the surface subsidence induced by the cylindrical cavern with CTC properties and RUTC properties, respectively. The results show that the subsidence rapidly increases at the beginning of cavern development. The closure rate decreases with time during the following six months, and tends to be constant through the end of 20 years. The surface subsidence is 1.79 and 1.26 centimeters for CTC properties and RUTC properties.

The vertical and horizontal closures of the cylindrical model are shown in Figures 5.10 and 5.11. The vertical closure is approximately twice higher than that of the horizontal closure. For CTC properties, the vertical and horizontal closures are 24.5 and 12.3 centimeters. For RUTC properties, the vertical closure is 18.8 centimeters and the horizontal closure is 9.4 centimeters after 20 years.

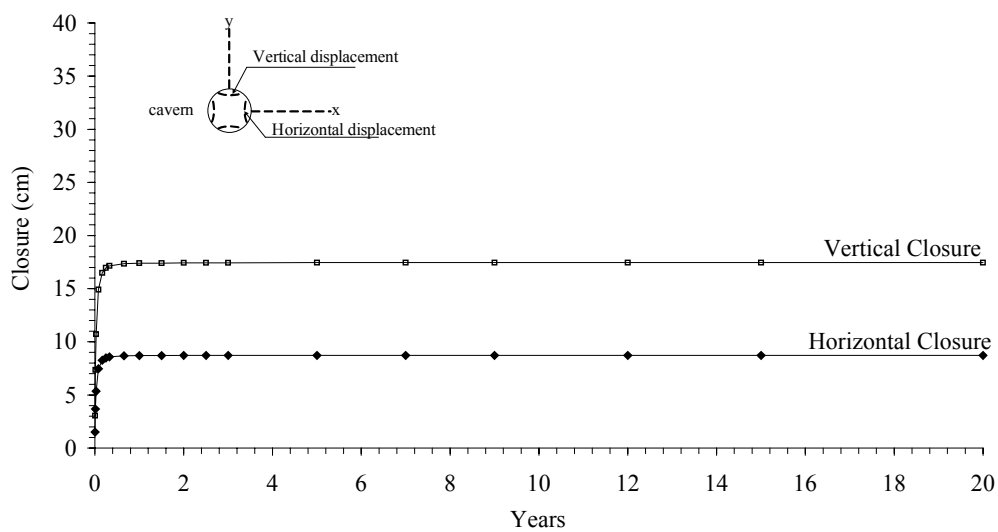


Figure 5.6 Diameter closure of the spherical cavern with the properties calibrated from the results of CTC test.

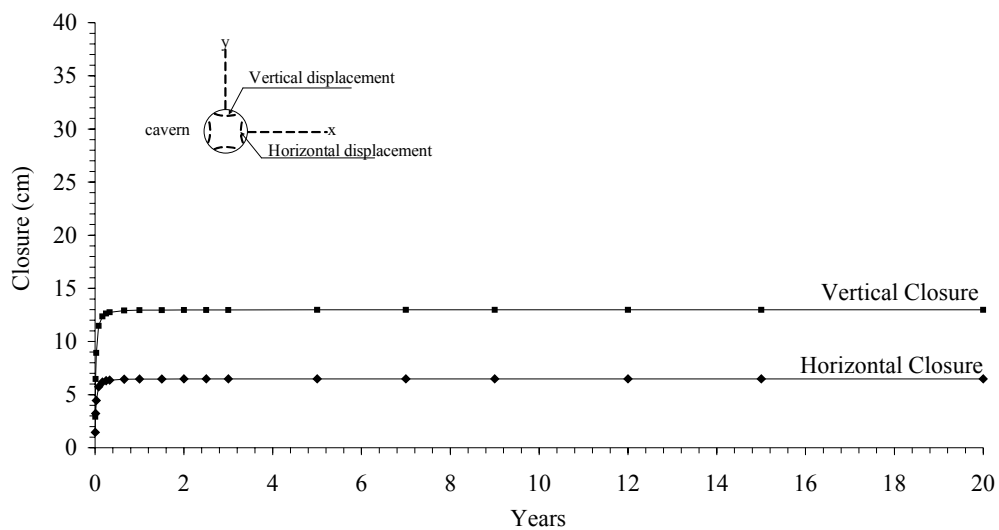


Figure 5.7 Diameter closure of the spherical cavern with the properties calibrated from the results of RUTC test.

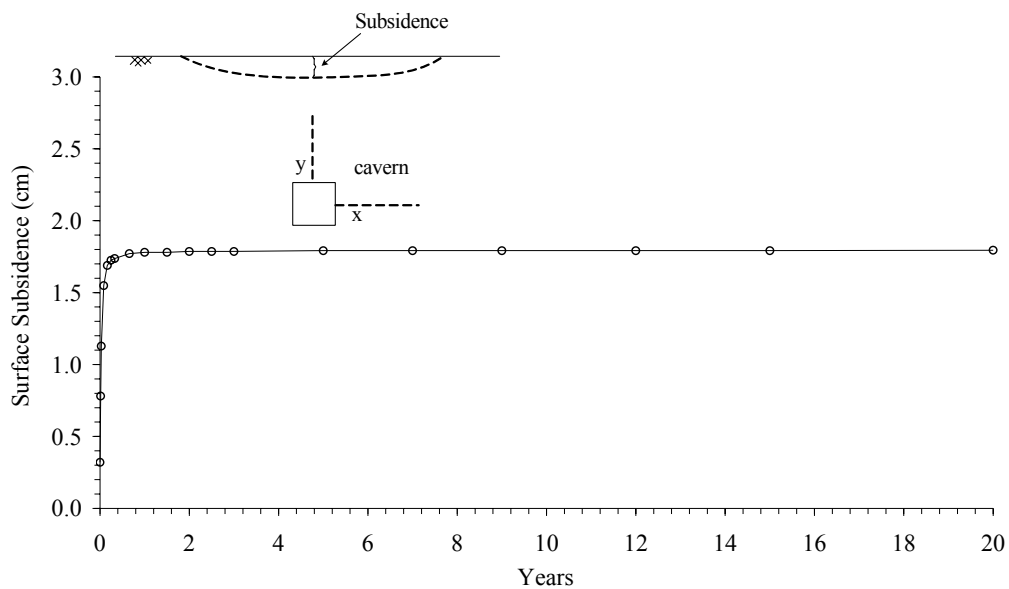


Figure 5.8 Surface subsidence induced by the cylindrical cavern with the properties calibrated from the results of CTC test.

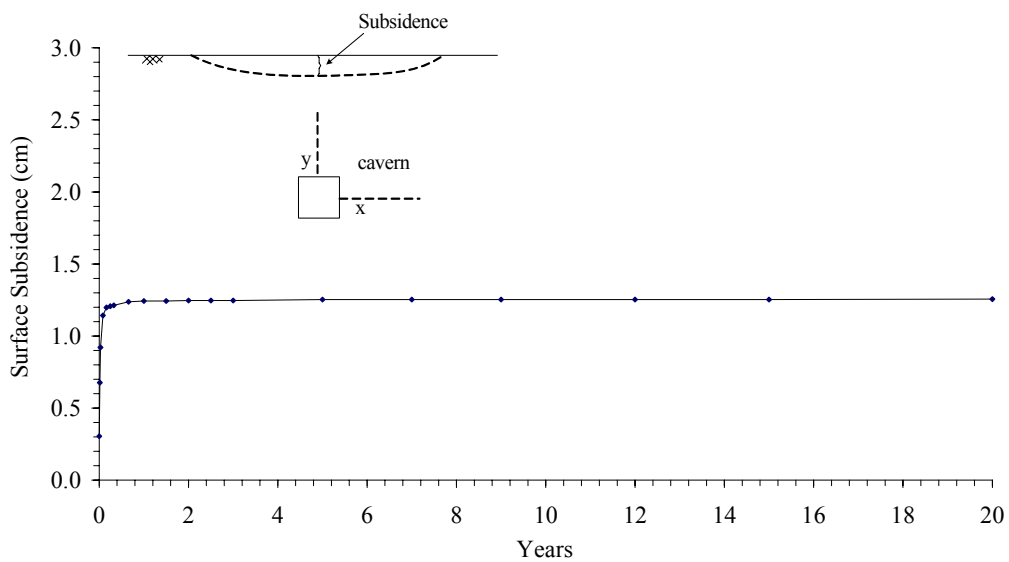


Figure 5.9 Surface subsidence induced by the cylindrical cavern with the properties calibrated from the results of RUTC test.

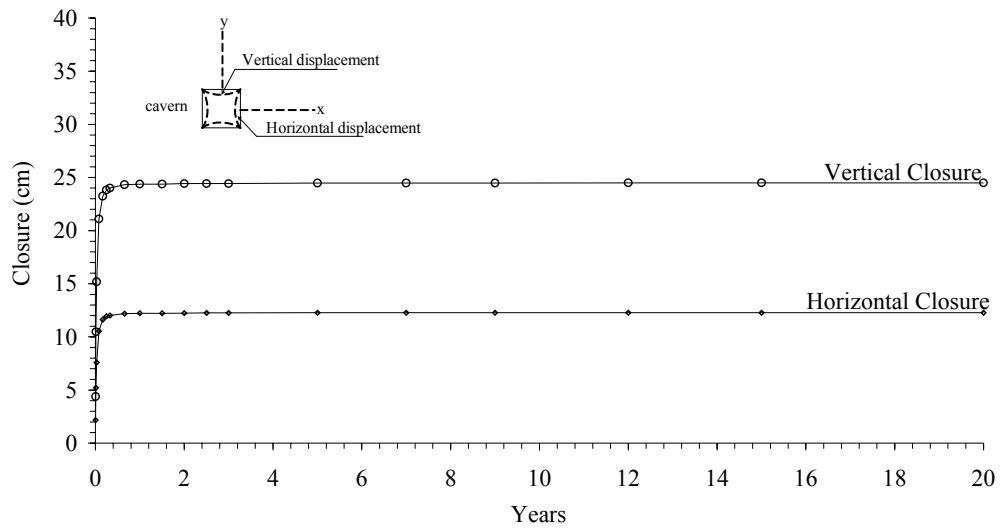


Figure 5.10 Diameter closure of the cylindrical cavern with the properties calibrated from the results of CTC test.

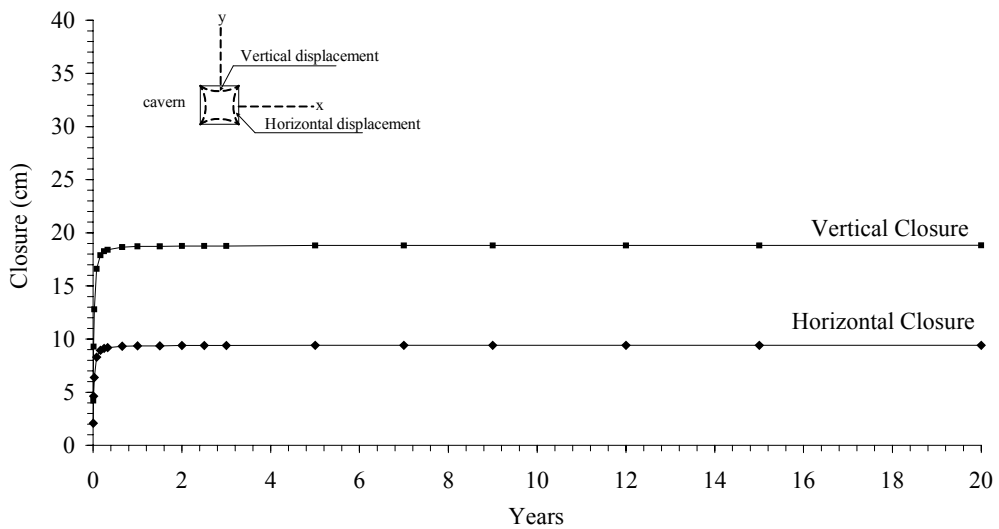


Figure 5.11 Diameter closure of the spherical cavern with the properties calibrated from the results of RUTC test.

CHAPTER VI

COMPARISONS AND DISCUSSIONS

6.1 Introduction

The objectives of this chapter are to compare the results of applying different loading paths on the salt specimens and to discuss the stress path dependency of the salt.

6.2 Comparison of the Experimental Results

The results discussed in this section are obtained from Chapter III. Comparisons of the creep behavior of salt subjected to different triaxial loading paths in octahedral shear strain-time curves are illustrated in Figures 6.1 through 6.4. For the first stage, since the specimens are subjected to relatively low octahedral shear stress and short-term duration, the elastic behavior of the salt in this stage becomes dominant. The differences in the deformations caused by applying loading paths in the CTC test and the RUTC test are not clearly seen. However, the specimens subjected to the RUTC test (hereafter called RUTC specimens) tend to show a greater deformation than that of the CTC test (hereafter called CTC specimens) except specimen number CTC-2e and RUTC-2e. The differences of the total octahedral shear strains are between 26% and 50%. For the second stage, the CTC specimens notably show a higher total octahedral shear strain than that occurred in the RUTC specimens. The differences of their magnitudes are between 5% and 21%.

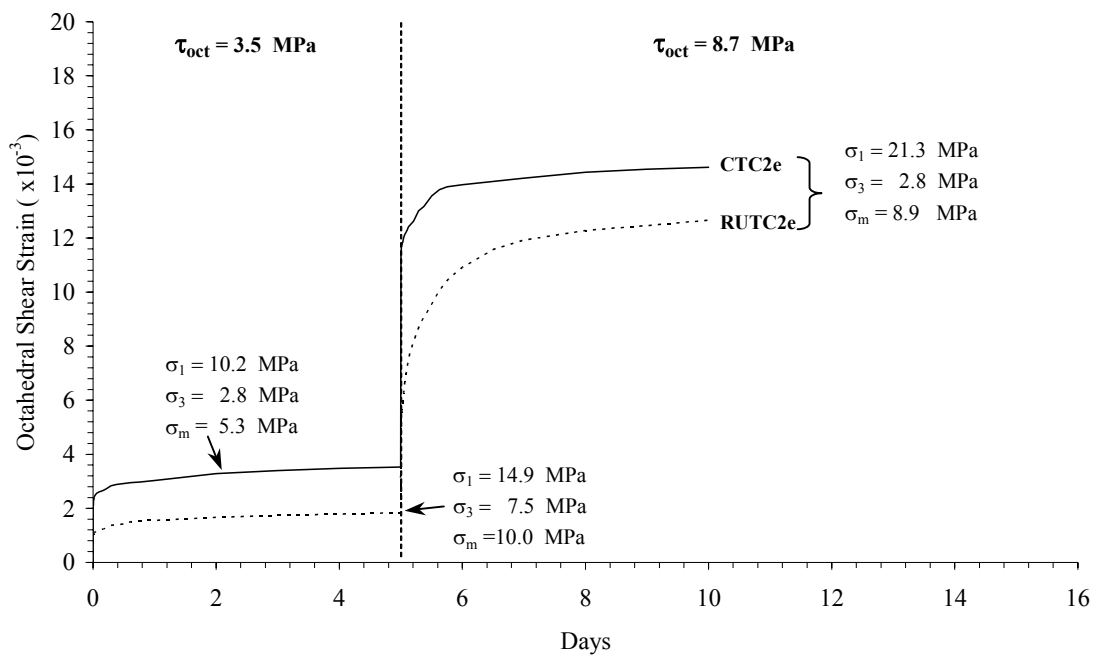


Figure 6.1 Comparison of the creep test results from different loading paths on salt specimens (no. BD99-1-CTC2e and BD99-1-RUTC2e)

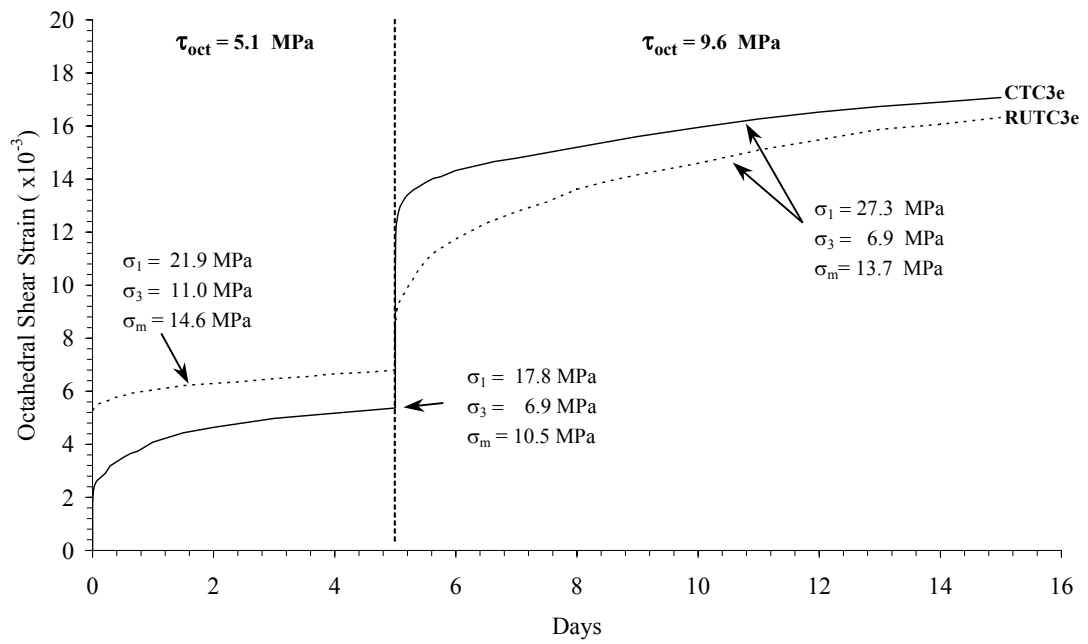


Figure 6.2 Comparison of the creep test results from different loading paths on salt specimens (no. BD99-1-CTC3e and BD99-1-RUTC3e)

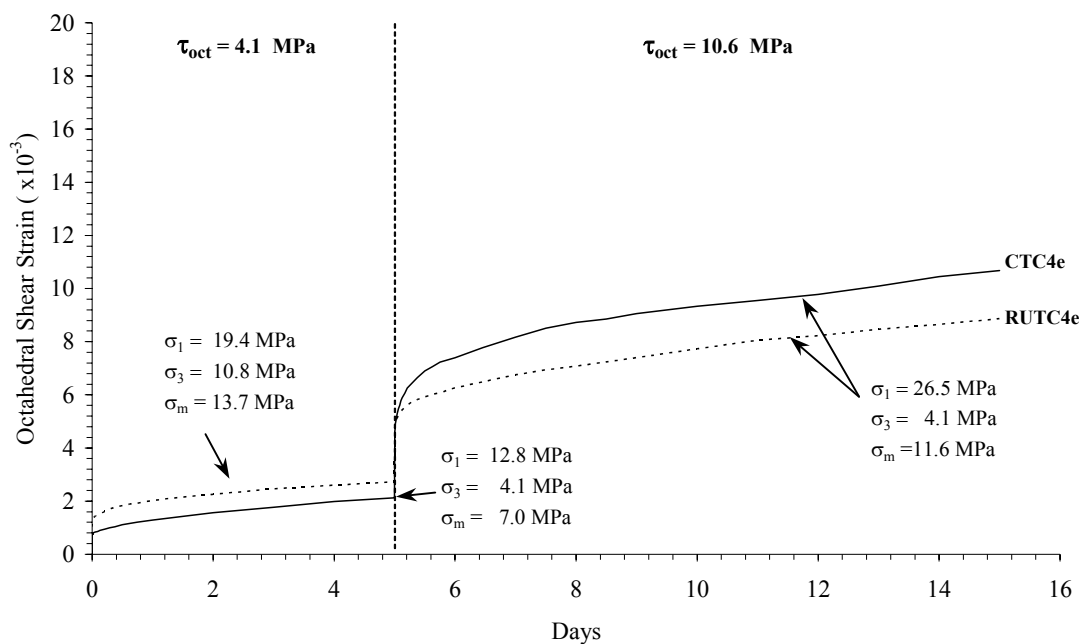


Figure 6.3 Comparison of the creep test results from different loading paths on salt specimens (no. BD99-1-CTC4e and BD99-1-RUTC4e)

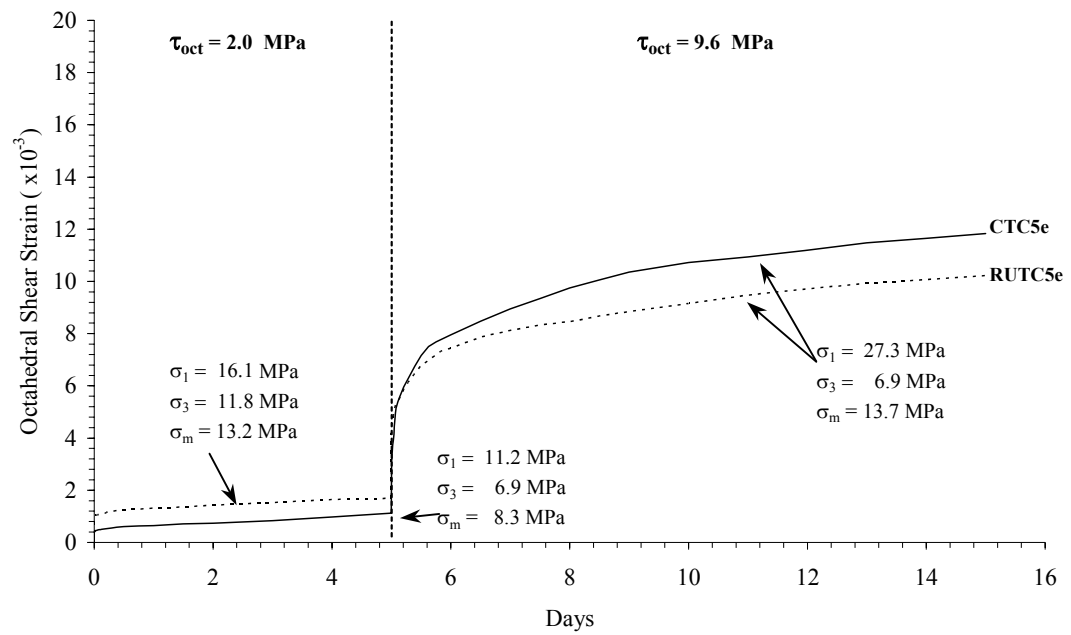


Figure 6.4 Comparison of the creep test results from different loading paths on salt specimens (no. BD99-1-CTC5e and BD99-1-RUTC5e)

6.3 Comparison of Calibrated Property Parameters

Comparisons of the results of calibrated property parameters from CTC and RUTC test results are illustrated in Tables 6.1 and 6.2. The parameters listed in Table 6.1 are averaged from the two stages of loading from Tables 4.2 and 4.3. The parameters listed in Table 6.2 are averaged from the four specimens tested for each loading path. The key parameters presented here are obtained from Chapter IV. The elastic constants are obtained from the linear portion of the curve. According to theoretical implications and experimental results, the elastic constants are not affected by the stress path. For the viscoelastic parameters, the retarded shear modulus and the elastoviscosity calibrated from the CTC test results are smaller than that from the RUTC test results. The differences of their magnitudes are 44% and 4% for the retarded shear and the elastoviscosity, respectively. The retarded bulk modulus calibrated from the CTC test results is greater than that from the RUTC test results. The difference of their magnitudes is 22%. For the viscoplastic parameter, the plastoviscosity coefficient calibrated from the RUTC test results is slightly greater than that from the CTC test results. The difference of their magnitudes is 19%.

6.4 Comparison of the Computer Modeling Results

The results presented here are obtained from Chapter V. Figures 6.5 through 6.10 compare the computer modeling results for the salt cavern using the parameters calibrated from different stress paths. The magnitudes of the surface subsidence obtained from the RUTC properties are less than that from the CTC properties (Figures 6.5 and 6.8). The subsidence is 31.6% for the spherical cavern and 30.1% for the cylindrical cavern. The vertical and horizontal closures simulated from the

Table 6.1 Comparison of salt property parameters calculated from different loading paths.

Stage	Symbol	Unit	BD99-1-CTC-2e	BD99-1-RUTC-2e	BD99-1-CTC-3e	BD99-1-RUTC-3e	BD99-1-CTC-4e	BD99-1-RUTC-4e	BD99-1-CTC-5e	BD99-1-RUTC-5e
Viscoelastic	G_2	GPa	0.6	0.7	0.5	1.0	0.6	1.4	1.8	2.3
	K_2	GPa	1.25	2.8	1.9	1.1	4.0	3.2	4.2	2.3
	η_2	GPa-day	7.4	7.1	7.3	7.6	7.0	7.1	6.9	9.0
Viscoplastic	η_4	GPa-day	18.0	17.7	10.9	8.7	10.2	12.2	9.8	11.1

Table 6.2 Properties of salt used in the simulation. They are averaged from four specimens for each loading path.

Stage	Property	Symbol	Unit	CTC	RUTC
Viscoelastic	Retarded shear modulus	G_2	GPa	0.9 (0.4-3.1)	1.3 (0.2-4.0)
	Retarded bulk modulus	K_2	GPa	2.8 (0.8-5.6)	2.3 (1.0-4.2)
	Elastoviscosity	η_2	GPa-day	7.4 (6.9-7.9)	7.7 (7.2-9.0)
Viscoplastic	Plastoviscosity	η_4	GPa-day	12.2 (5.1-21.1)	14.5 (7.1-19.8)

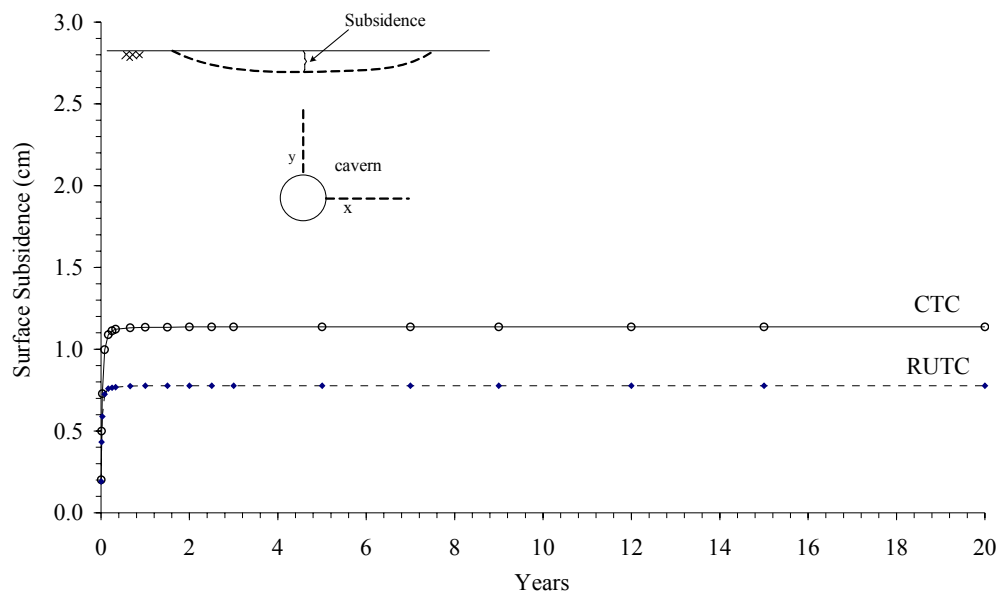


Figure 6.5 Comparison of surface subsidence induced by the spherical cavern with the CTC properties and RUTC properties.

RUTC properties are less than that from the CTC properties (Figures 6.6, 6.7, 6.9 and 6.10). The closure is 25.7% for the spherical cavern and 23.3% for the cylindrical cavern.

6.5 Discussions

6.5.1 Discussions on the Experiments

Within the first loading stage, since the specimens used in both loading paths are subjected to relatively low octahedral shear stresses under short duration, the deformation in the elastic mode of specimen is only affected by the intrinsic properties of salt, such as size, shape and orientation of crystal and inclusions. This phenomenon reveals that the results of this study are similar to the research results of Allemandou and Dusseault (1993). In the transient creep phase, the conventional triaxial method shows lower deformation than that of the RUTC test method. The results here agree with the findings from Assis and Kaiser (1991).

In the second loading stage, the CTC specimens notably show a higher total octahedral shear strain than that occurred in the RUTC specimens. This may be caused by the difference of the loading paths from the previous stage. As the RUTC specimens have been subjected to a higher mean stress than the CTC specimens, their crystals may be more compacted than the CTC specimens. Therefore, the CTC specimens would be able to provide a higher deformation in the second stage. The specimen number RUTC-2e however shows less deformation than that from the CTC specimens in the first stage. These results imply that its intrinsic properties may be softer than those of the CTC specimens.

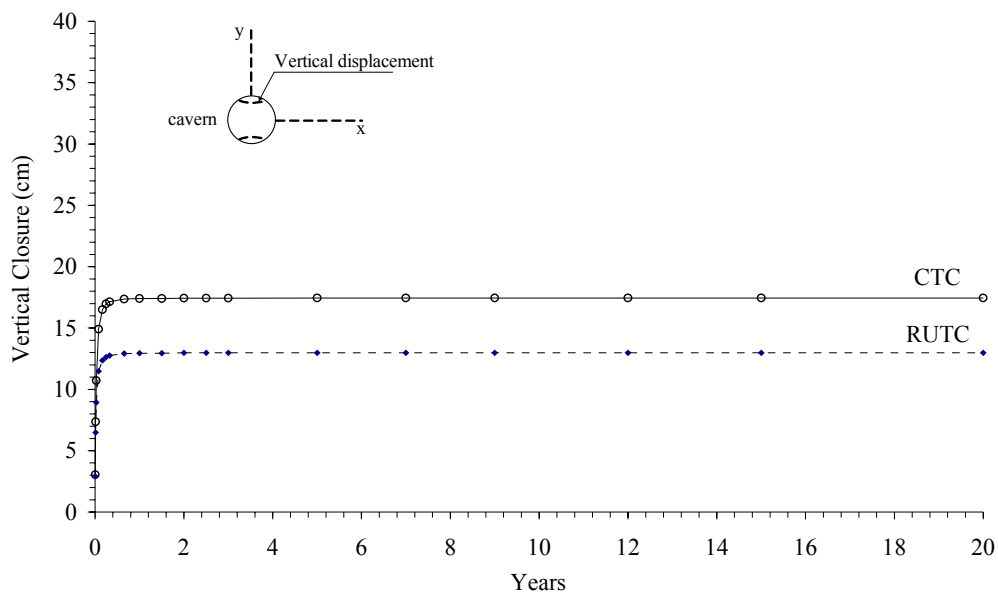


Figure 6.6 Comparison of vertical closure of the spherical cavern with the CTC properties and RUTC properties.

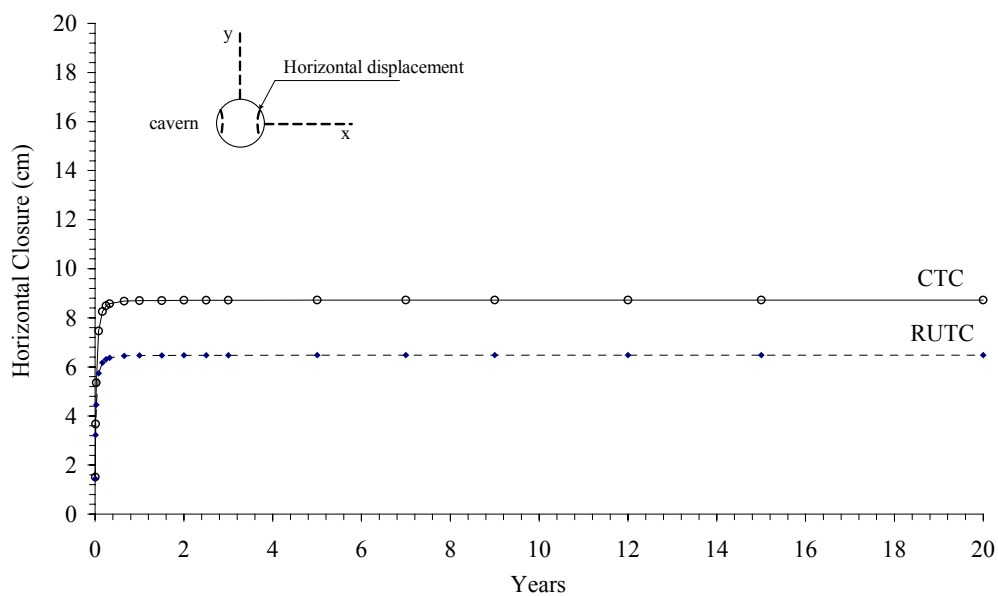


Figure 6.7 Comparison of horizontal closure of the spherical cavern with the CTC properties and RUTC properties.

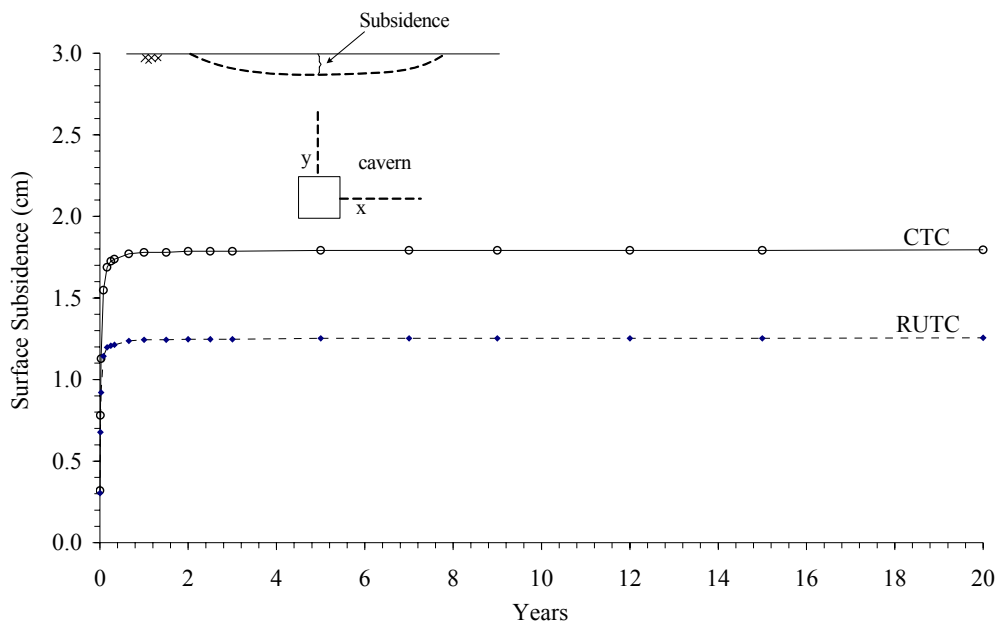


Figure 6.8 Comparison of surface subsidence induced by the cylindrical cavern with the CTC properties and RUTC properties.

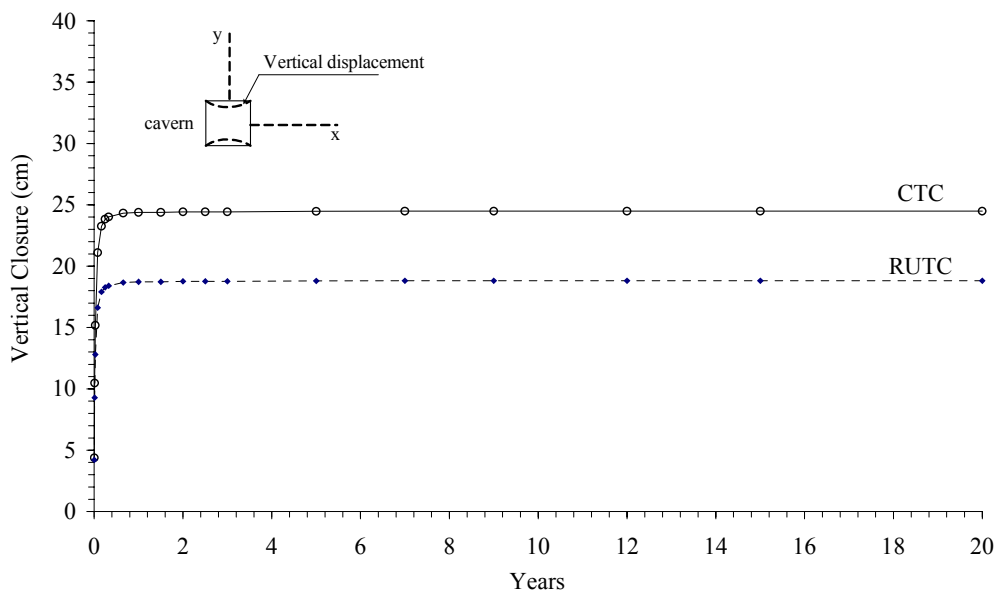


Figure 6.9 Comparison of vertical closure of the cylindrical cavern with the CTC properties and RUTC properties.

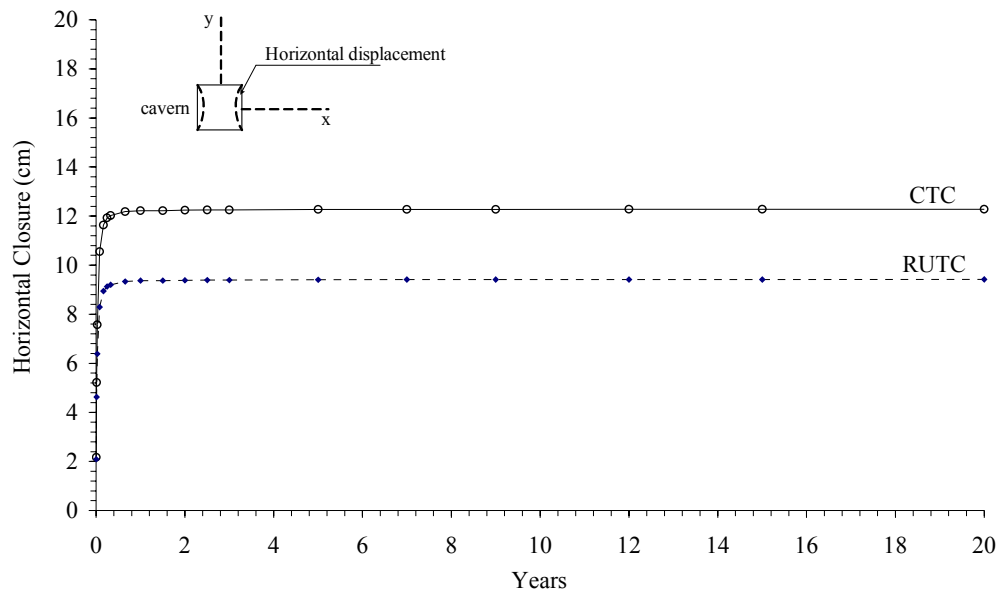


Figure 6.10 Comparison of horizontal closure of the cylindrical cavern with the CTC properties and RUTC properties.

The results from both loading paths suggest that the effect of the variation of the intrinsic properties of salt could be minimized by conducting the experiments on a larger number of specimens, collecting from the same depth or as near as possible. The effect of stress path may be more pronounced in plastic mode under higher stresses. Higher load may be required to apply more octahedral shear stress on the test specimens. Longer test duration should be taken to show the viscoplastic behavior. Larger specimen size may be needed to observe the plastic behavior because the dislocation climb is a main mechanism in the viscoplastic phase. The specimen diameter should be at least ten times the crystal size.

A difference in the increase of loading from zero to a constant value may occur at the beginning of the test. This may cause a difference in the instantaneous deformation for each specimen. Automatic test machine may be needed to reduce this effect. Viscosity of the hydraulic oil used for pressuring inside the Hoek cell should be increased to reduce the variation of confining pressures affected from the temperature. Volumetric change should be monitored to detect the effect of loading direction on the deformation.

6.5.2 Discussions on the Property Calibration

The elastic constants are obtained from the linear portion of the curves which should be independent of the stress path. The viscoelastic parameters may be influenced by the difference in loading directions and sequences. The viscoelastic parameters from the two loading paths are different. This suggests that the constitutive law and creep equations may not truly represent the viscoelastic behavior of the salt specimens. This may be solved by using other constitutive laws to describe the behavior and to compare the results in this viscoelastic phase. For the viscoplastic

phase, the magnitudes of the viscoplastic coefficient parameters calibrated from the RUTC test results are slightly greater than that from the CTC results. These might be caused by the difference in the mean stresses within the first stage. A larger difference of the plastoviscosity may be obtained if the CTC and the RUTC specimens are under higher octahedral shear stress for a longer period.

6.5.3 Discussions on the Computer Modeling

All simulation results show that the ultimate surface subsidence and cavern closures obtained from the CTC properties are less than that from the RUTC properties. This is due to that the CTC parameters are smaller than the RUTC parameters. The effect of stress path is significant for computer modeling. The spherical and cylindrical caverns show mechanically stable as evidenced by the predicted surface subsidence and cavern closures.

Since the characteristics of stress state around salt cavern can be changed to stress reduced condition during operational construction (Lux, 1988; Wallner, 1988; Assis and Kaiser, 1991; Schmidt, 1993 and Rolfs et al., 1996), RUTC technique represents more realistic in-situ stress than that of CTC technique. On the other hand, due to the creep deformation of CTC specimens is higher than that of RUTC specimens, the parameters calibrated from the CTC test are more conservative.

CHAPTER VII

CONCLUSIONS AND RECOMEMDATIONS FOR FUTURE STUDIES

7.1 Conclusions

The objective of this research is to assess the effect of stress path on the mechanical behavior of rock salt by means of mechanical laboratory testing and numerical analysis. The creep property parameters calibrated from the results of conventional triaxial creep test (CTC) and radially unloaded triaxial creep test (RUTC) are compared to reveal the effect of stress path. The significance of the stress path dependency is evaluated by performing numerical modeling of salt behavior around storage caverns.

This research consists of five tasks, including literature review, sample collection and preparation, laboratory experiments, numerical modeling, and comparative analysis. Results from the existing researches have suggested that under the assumption of the elastic principle, the effect of different loading directions and sequences is ignored. For the material in the plastic range, its behavior depends on the influence of stress path or loading sequence and direction. Since salt exhibits complex mechanical behavior due to the plastic deformation and time dependency, the stress path effect on the engineering structures in the salt formation should be considered in the design. This concept agrees reasonably with the results of laboratory testing on the inelastic material. For linearly elastic, the influence of stress

path remains ambiguous. The different stress paths are used for various objectives, such as to construct yield surface or failure surface and to describe models. However, no published research has revealed the effect of stress path to evaluate the mechanical parameters of rocks. The analysis of stress state around salt cavern has been an important issue due to the changes of stress orientation generated by the constructional and operational phases.

Series of laboratory tests have been performed to investigate the mechanical and rheological properties of rock salt specimens obtained from the Middle and Lower Salt members of the Maha Sarakham Formation. The characterization tests include the uniaxial compressive strength tests, Brazilian tensile strength tests and the triaxial compressive strength tests. To determine the creep parameters, the conventional triaxial creep test (CTC) and the radially unloaded triaxial creep test (RUTC) have been carried out. The average uniaxial compressive strengths is 34.7 ± 2.2 MPa. The average tensile strengths of the salt specimen is 1.75 ± 0.40 MPa. The compressive and tensile strengths of the Maha Sarakham salt are relatively high as compared with those from various sources. The average Poisson's ratio is 0.37. Using the Coulomb criterion, the cohesion is 6.0 MPa and the internal friction angle is 50 degrees. For the triaxial creep tests (CTC and RUTC), two loading stages have been applied. The octahedral shear stresses of 2.0, 3.5, 4.1 and 5.1 MPa are applied for the first stage (5 days). The second stage uses the shear stresses of 8.7, 9.6, and 10.6 MPa (10 days). The instantaneous strains tend to increase as the octahedral shear stresses increase. The octahedral shear strain rate in the first loading stage is lower than that in the second stage because the octahedral shear stress in the first stage is less than in the second stage. Since the specimens are subjected to relatively

low octahedral shear stress under short duration, the elastic behavior of the salt in this stage becomes dominant in the first loading stage. The differences in the deformations caused by applying loading paths in the CTC test and the RUTC test are not clearly seen. However, the specimens subjected to the RUTC specimen tend to show a greater deformation than that of the CTC specimens. The differences of the total octahedral shear strains are between 26% and 50%. For the second stage, the CTC specimens notably show a higher total octahedral shear strain than that occurred in the RUTC specimens. The differences of their magnitudes are between 5% and 21%.

Curve fitting technique using a finite element program is used to evaluate the property parameter values. The test results from the two loading paths are used to determine parameter sets include the elastic, viscoelastic and viscoplastic parameters of the salt specimens. From the theoretical implications and experimental results, the elastic constants are not affected by the stress path. For the viscoelastic parameters, the retarded shear modulus and the elastoviscosity calibrated from the CTC test results are smaller than that from the RUTC test results. The differences of their magnitudes are about 44% and 4% for the retarded shear and the elastoviscosity. The retarded bulk modulus calibrated from the CTC test results is greater than that from the RUTC test results. The difference of their magnitudes is about 22%. The plastoviscosity coefficient calibrated from the RUTC test results is slightly greater than that from the CTC test results. The difference of their magnitudes is about 19%.

An isolated spherical cavern and cylindrical cavern are simulated to investigate the significance of the stress paths. Comparison of the simulated results from different property parameters has been made. The surface subsidence obtained from

the RUTC properties are 31.6% (for spherical) and 30.1% (for cylindrical) less than those from the CTC properties. The vertical and horizontal closures simulated from the RUTC properties are 25.7% (for spherical) and 23.3% (for cylindrical) less than those from the CTC properties.

The results presented above imply that the parameters calibrated from the RUTC test results may be more representative to the actual conditions. The creep deformation of CTC specimens is higher than that of RUTC specimens, and hence the parameters calibrated from the CTC test are more conservative. The creep behavior of rock salt under higher octahedral shear stress depends on the stress path. The difference between the CTC properties and the RUTC properties is significant when they are used to predict the salt cavern behavior.

7.2 Recommendations for Future Studies

Various test methods may be required to obtain a more understanding of the impact of the stress sequences and directions, such as true triaxial loading test, multi-step triaxial loading, and triaxial cyclic creep test. The micro-structural analysis may be desirable to study the crystal orientation in salt specimens after testing under different loading directions. The volumetric dilation should be measured during triaxial creep test to study the effect of loading paths.

The exponential law used in this study may not adequately describe the salt behavior. Other constitutive laws, such as power laws and structural laws may be needed to describe the salt behavior. The constitutive law can consider the stress path dependent that may be desirable.

REFERENCES

- Allemandou, X. and Dusseault, M.B. (1993). Procedure for cyclic creep testing of salt rock, results and discussion. In **Proceedings of the 3rd Conference on the Mechanical Behavior of Salt** (pp. 207-218). Clausthal-Zellerfeld: Trans Tech Publications.
- Andreev, G.E. (1995). **Brittle rock failure of rock materials: test results and constitutive model**. Rotterdam: A.A. Balkema.
- Assis A.P. and Kaiser, P.K. (1991). Stress path dependence of creep parameters, In **Proceedings of the 7th International Congress on Rock Mechanics** (pp. 177-181). Rotterdam: A. A. Balkema,
- ASTM D2664-95. Standard test method for triaxial compressive strength of untrained rock core specimens without pore pressure measurements. In **Annual Book of ASTM Standards**, (Vol. 04.08). Philadelphia: American Society for Testing and Materials.
- ASTM D2938-95. Standard test method for unconfined compressive strength of intact rock core specimens. In **Annual Book of ASTM Standards** (Vol. 04.08). Philadelphia: American Society for Testing and Materials.
- ASTM D3967-95. Standard test method for splitting tensile strength if intact rock core specimens. In **Annual Book of ASTM Standards**, (Vol. 04.08). Philadelphia: American Society for Testing and Materials.

- ASTM D4406-93. Standard test method for creep of cylindrical rock core specimens in triaxial compression. In **Annual Book of ASTM Standards** (Vol. 04.08). Philadelphia: American Society for Testing and Materials.
- ASTM D4543-85. Standard practice for preparing rock core specimens and determining dimensional and shape tolerances. In **Annual Book of ASTM Standards** (Vol. 04.08). Philadelphia: American Society for Testing and Materials.
- ASTM D5407-95. Standard test method for elastic moduli of untrained intact rock core specimens in triaxial compression without pore pressure measurement. In **Annual Book of ASTM Standards** (Vol. 04.09). Philadelphia: American Society for Testing and Materials.
- Aubertin, M., Julien, M.R., Servant, S. and Gill, E.D. (1999). A rate-dependent model for the ductile behavior of salt rocks. **Canadian Geotechnical Journal**. 36: 660 – 674.
- Berest, P. and Blum, P.A. (1993). In situ tests in salt caverns. In **Proceedings of the 7th Symposium on Salt** (Vol. I, pp.353-362). Amsterdam: Elsevier Science Publishers.
- Bieniawski, Z.T. and Hawkes, I. (1978). Suggested Methods for determining tensile strength of rock materials. **International Journal of Rock Mechanics and Mining Sciences & Geomechanics Abstracts** (pp. 118-121). International Society for Rock Mechanics Commission on Standardization of Laboratory and Field Tests.

- Bieniawski, Z.T., et al. (1978). Suggested Methods for determining the uniaxial compressive strength and deformability of rock materials. **International Journal of Rock Mechanics and Mining Sciences & Geomechanics Abstracts**. (pp. 135-140). International Society for Rock Mechanics Commission on Standardization of Laboratory and Field Tests.
- Boontongloan, C. (2000). **Engineering properties of the evaporitic and clastic rocks of Maha Sarakam formation, Sakon Nakhon evaporite basin**. M.S. thesis, Asian Institute of Technology, Thailand.
- Bylia, O.I., et al. (1997). The influence of simple and complex loading on structure change in two-phase titanium alloy. **Scripta Metall** 36: 949-954.
- Chan, K.S. (1993). **Final development of the Multimechanism Deformation Coupled Fracture (MDCF) constitutive model**. Monthly Technical Report Contract No. AQ-1458, prepared for the Southwest Research Institute, Sandia National Laboratories (February, FY'96-2).
- Chen, W.F. and Zhang, H. (1991). **Structural plasticity, theory, problems and CAE software**. New York-Berlin: Springer.
- Clerc, R.A. and Dubois, D. (1980). Long term operation of underground storage in salt. In **Proceedings of the 5th Symposium on Salt** (Vol. II, pp.3-11). Hamburg: Northern Ohio Geological Society.
- Crotogino, F.R. (1984). Salt cavern in situ testing from the constructor's and the operator's viewpoint. In **Proceedings of the 1st Conference on the Mechanical Behavior of Salt** (pp. 613-628). Clausthal-Zellerfeld: Trans Tech Publications.

- Crouch, S.L. (1972). A note on post-failure stress-strain path dependence in Norite. **International Journal of Rock Mechanics and Mining Sciences**. 9: 197-204.
- Devries, K.L., Mellegard, K.D. and Callahan, G.D. (2002). **Salt damage criterion proof-of-concept research**. Topical report, DE-FC26-00NT41026, prepared for the U.S. Department of Energy, Pennsylvania.
- Dreyer, W.E. (1984). Crude oil storage in a system of salt caverns. In **Proceedings of the 1st Conference on the Mechanical Behavior of Salt** (pp. 629-660). Clausthal-Zellerfeld: Trans Tech Publications.
- Eriksson, L.G. and Michalski, A. (1986). Hydrostatic conditions in salt domes—a reality or a modeling simplification. In **Proceedings of the International Symposium on Rock Stress and Rock Stress Measurement** (Vol. I, pp.121-132). Lulea, Sweden: Centek Publisher.
- Fairhurst, C., St. John, C.M., Midea, N.F., deEston, S.M., Fernandes, A.C., and Boniovanni, L.A. (1979). Rock mechanics studies of proposed underground mining potash in Sergipe, Brazil. In **Proceedings of the 4th International Congress on Rock Mechanics** (Vol. 1, pp. 131-137). Montreux.
- Fischer, F.J., Light, B.D. and Paslay, P.R. (1988). Salt-cavern closure during and after formation. In **Proceedings of the 2nd Conference on the Mechanical Behavior of Salt** (pp. 493-508). Clausthal-Zellerfeld: Trans Tech Publications.
- Fuenkajorn K. and Serata, S. (1993). Numerical simulation of strain-softening and dilation of rock salt. **International Journal of Rock Mechanics, Mining Sciences and Geomechanics Abstracts**. 30: 1303-1306.

- Fuenkajorn, K. and Daemen, J.J.K. (1988). **Borehole closure in salt**. Technical report NUREC/CR-5243, prepared for the U. S. Nuclear Regulatory Commission, Washington, D. C.
- Fuenkajorn, K. and Jandakaew, M. (2003). Compressed-air energy storage in salt dome at Borabu district, Thailand: Geotechnical Aspects. In **Proceedings of the 38th Symposium on Engineering Geology and Geotechnical Engineering** (pp. 377-391). Reno, Nevada: University of Nevada.
- Fuenkajorn, K. and Serata, S. (1992). Geohydrological integrity of CAES in rock salt. In **Compressed-Air Energy Storage: Proceedings of the 2nd International Conference** (pp. 4.1-4.21) San Francisco: Electric Power Research Institute.
- Fuenkajorn, K. and Serata, S. (1994). Dilation – induced permeability increase around cavern in rock salt. In **Proceedings of the 1st North American Rock Mechanics Symposium** (pp. 648-656). Rotterdam: A. A. Balkema.
- Fuenkajorn, K., Phueakphum, D., and Jandakaew, M. (2003). Healing of rock salt fractures. In **Proceedings of the 38th Symposium on Engineering Geology and Geotechnical Engineering**, (pp. 393-408). Reno, Nevada: University of Nevada.
- Goodman, R. E. (1989). **Introduction to rock mechanics**. New York: John Wiley & Sons.
- Guangzhi, Y., He, L. and Xuefn, X. (1988). The effect of the stress path on strength of rock. In **Proceedings of the 29th U.S. Symposium on Rock Mechanics** (pp. 95-101). Rotterdam: A. A. Balkema.

- Hansen, B.T., et al. (2002). Isotopic evidence for a Late Cretaceous age of the potash and rock salt deposit at Bamnet Narong, NE Thailand. In **The Symposium on Geology of Thailand**, 26-31 August, Bangkok, pp. 120.
- Hansen, F.D., Mellegard, K.D. and Senseny, P.E. (1984). Elasticity and strength of ten natural rock salts. In **Proceedings of the 1st Conference on the Mechanical Behavior of Salt** (pp. 71-83). Clausthal-Zellerfeld: Trans Tech Publications.
- Hardy, H.R. (1996). Application of the Kaiser effect for the evaluation of in-situ stress in salt. In **Proceedings of the 3rd Conference on the Mechanical Behavior of Salt** (pp. 85-100). Clausthal-Zellerfeld: Trans Tech Publications.
- Hardy, H.R. (1993). Evaluation of in situ stresses in salt using acoustic emission techniques. In **Proceedings of the 7th Symposium on Salt** (Vol. I, pp.49-58). Amsterdam: Elsevier Science Publishers.
- Heusermann, S. (1988). Aspects of overcoring stress measurements in rock salt. In **Proceedings of the 2nd Conference on the Mechanical Behavior of Salt** (pp. 273-289). Clausthal-Zellerfeld: Trans Tech Publications.
- Hoek, E. and Franklin, J.A. (1968). Simple triaxial cell for field or laboratory testing of rock. **Trans. Inst. Min. Metall.** 77A: 22-4.
- Hugout, B. (1988). Mechanical behavior of salt cavities- in situ tests-model for calculating the cavity volume evolution. In **Proceedings of the 2nd Conference on the Mechanical Behavior of Salt** (pp. 291-310). Clausthal-Zellerfeld: Trans Tech Publications.

- Hunsche, U. (1993). Failure behaviour of rock salt around underground cavities. In **7th Symposium on Salt** (Vol. 1, pp. 59-65). Amsterdam: Elsevier Science Publishers B. V.
- Hunsche, U. and Albrecht, H. (1990). Results of true triaxial strength tests on rock salt. **Engineering Fracture Mechanics**. 35: 867-877.
- Inoue, A., Kawakami, H. and Fujii, T. (1998). The effect of loading path on mechanical responses of a glass fabric composite at low cyclic fatigue under tension/torsion biaxial loading. In **American Society for Composite (ASC) the 13th Annual Technical Conference**. Maryland.
- Jaeger, J.C. (1967). Brittle fracture of rocks. In **Proceedings of the 8th U.S. Symposium on Rock Mechanics**. Baltimore: Port City Press.
- Jaeger, J.C. and Cook, N.G.W. (1979). **Fundamentals of rock mechanics**. London: Chapman and Hall.
- Japan International Cooperation Agency (1981). **Evaluation study report for ASEAN rock salt-soda ash project in the Kingdom of Thailand**, Tokyo, Japan.
- Khan, A.S. and Huang, S. (1995). **Continuum theory of plasticity**. New York: Wiley.
- Korshunov, A.A., et al. (1996). Grain-Structure refinement in titanium alloy under different loading schedules. **Journal of Material Sciences**. 31: 4635-4639.
- Lee, D.H., Juang, C.H., Chen, J.W., Lin, H.M. and Shieh, W.H. (1999). Stress paths and mechanical behavior of a sandstone in hollow cylinder tests. **International Journal of Rock Mechanics and Mining Sciences**. 36: 857-870.

- Lux, K.H. (1988). Some results of case history studies with respect to the mechanical behavior of existing caverns. In **Proceedings of the 2nd Conference on the Mechanical Behavior of Salt** (pp. 581-604). Clausthal-Zellerfeld: Trans Tech Publications.
- Lux, K.H. and Rokahr, R. (1984). Laboratory investigations and theoretical statements as a basis for the design of cavern in rock salt formation. In **Proceedings of the 1st Conference on the Mechanical Behavior of Salt** (pp. 169-179). Clausthal-Zellerfeld: Trans Tech Publications.
- Massier, D. (1996). Rate-type constitutive equations with application in the calculus of the stress state and of the displacement field around cavities in rock salt. In **Proceedings of the 3rd Conference on the Mechanical Behavior of Salt** (pp. 545-558). Clausthal-Zellerfeld: Trans Tech Publications.
- Nelson, R.A. and Kocherhans, M.W. (1984). In situ testing of salt in a deep borehole in Utah. In **Proceedings of the 1st Conference on the Mechanical Behavior of Salt** (pp. 493-510). Clausthal-Zellerfeld: Trans Tech Publications.
- Ottosen, N.S. and Krenk, S. (1979), Non linear analysis of cavities in rock salt. **International Journal of Rock Mechanics and Mining Sciences**. 16: 245-252.
- Padmanabhan, K.A., Vasin, R.A., and Enikeev, F.U. (2001). **Superplastic flow: Phenomenology and mechanics**. Berlin: Springer.
- Pueakphum, D. (2003). **Compressed-Air energy storage in rock salt of the Maha Sarakham Formation**. M.S. thesis, Suranaree University of Technology, Thailand.

- Price, A.M. (1979). **The effect of confining pressure on the post-yield deformation characteristics of rock.** Ph.D. Thesis, University of Newcastle-upon-Tyne.
- Pudewills, A. (1988). Thermomechanical calculations for a HLW borehole. In **Proceedings of the 2nd Conference on the Mechanical Behavior of Salt** (pp. 605-613). Clausthal-Zellerfeld: Trans Tech Publications.
- Rolfs, O., Schmidt, U. and Crocogino, F. (1996). Rock mechanical studies on the post-operational phase of a disposal cavern. In **Proceedings of the 3rd Conference on the Mechanical Behavior of Salt** (pp. 417-426). Clausthal-Zellerfeld: Trans Tech Publications.
- Schmidt, T. (1993). Fracture tests for determining primary stress conditions in salt deposits provide clues to the rock mechanics of salt caverns. In **Proceedings of the 7th Symposium on Salt** (Vol. I, pp.135-140). Amsterdam: Elsevier Science Publishers.
- Serata, S. (1968). Application of continuum mechanics to design of potash mines in Canada, **International Journal of Rock Mechanics and Mining Sciences**. 5: 293-314.
- Serata, S. and Fuenkajorn, K. (1993). Formulation of a constitutive equation for salt. In **Proceedings of the 7th International Symposium on Salt** (pp. 483 – 488). Amsterdam: Elsevier Science.
- Serata, S., Hiremath, M. and Oka K. (1991). **Long-term geomechanical stability analysis of salt dome for compressed air energy storage plant.** Report RP2615-2, prepared for Electric Power Research Institute, Serata Geomechanics, Inc.

- Shames, I.H. and Cozzarelli, F.A. (1997). **Elastic and inelastic stress analysis**. (Revised printing). Philadelphia: Taylor & Francis.
- Suwanich, P. and Ratanajaruraks, P. (1982). Potash and rock salt in Thailand: Appendix A core log of K-holes. **Nonmetallic minerals bulletin No. 2**. Bangkok: Economic Geology Division, DMR, Bangkok, Thailand.
- Suwanich, P. (1986). Potash and rock salt in Thailand. **Nonmetallic Minerals Bulletin No. 2**, Bangkok: Economic Geology Division, DMR, Bangkok, Thailand.
- Swanson, S.R. and Brown, W.S. (1971). An observation of loading path independence of fracture in rock. **International Journal of Rock Mechanics and Mining Sciences**. 8: 277-281.
- Therol, L. and Ghoreychi, M. (1996). Rock salt damage experimental results and interpretation. In **Proceedings of the 3rd Conference on the Mechanical Behavior of Salt** (pp. 175-189). Clausthal-Zellerfeld: Trans Tech Publications.
- Vogler, U.W. and Kovari, K. (1978). Suggested methods for determining the strength of rock materials in triaxial compression. **International Journal of Rock Mechanics and Mining Sciences and Geomechanics Abstracts**. 15: 47-54.
- Wallner, M. (1988). Frac-pressure for cavities in rock salt. In **Proceedings of the 2nd Conference on the Mechanical Behavior of Salt** (pp. 645-658). Clausthal-Zellerfeld: Trans Tech Publications.
- Wanten, P.H., Spiers, C.J. and Peach, C.J. (1996). Deformation of NaCl single crystals at $0.27T_m < T < 0.44T_m$. In **Proceedings 3rd Conference on the**

- Mechanical Behavior of Salt** (pp. 117-128). Clausthal-Zellerfeld: Trans Tech Publications.
- Warren, J. (1999). **Evaporites: Their evolution and economics**. Oxford: Blackwell Science.
- Wawersik, W.R. and Hannum, D.W. (1980). Mechanical behavior of New Mexico rock salt in triaxial compression up to 200°C. **Journal of Geophysical Research**. 85: 891-900.
- Wawersik, W.R. and Preece, D.S. (1981). Creep testing of salt-procedure, problems and suggestions. In **Proceedings of the 1st Conference on the Mechanical Behavior of Salt** (pp. 421-449). Clausthal-Zellerfeld: Trans Tech Publications.
- Wawersik, W.R., Callender, J.F., Weaver, B., and Dropek, R.K. (1976). Preliminary determination of mechanical properties of rock salt. In **Proceedings of the 17th U.S. Rock Mechanics Symposium** (pp. 506-1-7). Salt Lake City, Utah.
- Wetchasat, K. (2002). **Assessment of mechanical performance of rock salt formations for nuclear waste repository in northeastern Thailand**, M.S. thesis, Suranaree University of Technology, Thailand.
- Yahya, O.M.L., Aubertin, M., and Julien, M.R. (2000). A unified representation of the plasticity, creep and relaxation behavior of rock salt. **International Journal of Rock Mechanics and Mining Sciences**. 37: 787 – 800.
- Yin, F. (1998). **The creep of potash rock from New Brunswick**. M.S. thesis, University of Manitoba.

BIOGRAPHY

Mr. Mongkhol Jandakaew was born in Nakhon Sawan province. He earned his Bachelor's Degree in Geological Engineering from Suranaree University of Technology (SUT) in 2001. In 1999, he was awarded a scholarship from ESSO Thailand Company. For his post-graduate, he continued to study with a Master's Degree in Geological Engineering emphasizing on rock mechanics at SUT. In 2002, he also studied with a Bachelor's Degree in business administration emphasizing on construction management at Sokhothai Tammathirat Open University. During 1999 to 2003, he was a part time teaching assistant at SUT and research assistant at the Department of Alternative Energy Development and Efficiency (DEDE). Moreover, he worked for a civil engineering company as an assistant tunnel engineer. In 2003, he has published two technical papers related to rock salt mechanics at the conference of Engineering Geology and Geotechnical Engineering, University of Nevada, USA. For his work, he has a good knowledge in geomechanics theory and practice.